PERFORMANCE ANALYSIS AND NETWORK PATH CHARACTERIZATION FOR SCALABLE INTERNET STREAMING

A Dissertation

by

SEONG-RYONG KANG

Submitted to the Office of Graduate Studies of
Texas A&M University
in partial fulfillment of the requirements for the degree of

DOCTOR OF PHILOSOPHY

May 2008

Major Subject: Computer Science

PERFORMANCE ANALYSIS AND NETWORK PATH CHARACTERIZATION FOR SCALABLE INTERNET STREAMING

A Dissertation

by

SEONG-RYONG KANG

Submitted to the Office of Graduate Studies of
Texas A&M University
in partial fulfillment of the requirements for the degree of

DOCTOR OF PHILOSOPHY

Approved by:

Chair of Committee,	Dmitri Loguinov
Committee Members,	Riccardo Bettati
	Yoonsuck Choe
	Narasimha Reddy
Head of Department,	Valerie E. Taylor

May 2008

Major Subject: Computer Science

ABSTRACT

Performance Analysis and Network Path Characterization
for Scalable Internet Streaming. (May 2008)
Seong-Ryong Kang, B.S., Kyungpook National University;
M.S., Texas A&M University
Chair of Advisory Committee: Dmitri Loguinov

Delivering high-quality of video to end users over the best-effort Internet is a challenging task since quality of streaming video is highly subject to network conditions. A fundamental issue in this area is how real-time applications cope with network dynamics and adapt their operational behavior to offer a favorable streaming environment to end users.

As an effort towards providing such streaming environment, the first half of this work focuses on analyzing the performance of video streaming in best-effort networks and developing a new streaming framework that effectively utilizes unequal importance of video packets in rate control and achieves a near-optimal performance for a given network packet loss rate. In addition, we study error concealment methods such as FEC (Forward-Error Correction) that is often used to protect multimedia data over lossy network channels. We investigate the impact of FEC on the quality of video and develop models that can provide insights into understanding how inclusion of FEC affects streaming performance and its optimality and resilience characteristics under dynamically changing network conditions.

In the second part of this thesis, we focus on measuring bandwidth of network paths, which plays an important role in characterizing Internet paths and can benefit many applications including multimedia streaming. We conduct a stochastic anal-

ysis of an end-to-end path and develop novel bandwidth sampling techniques that can produce asymptotically accurate capacity and available bandwidth of the path under non-trivial cross-traffic conditions. In addition, we conduct comparative performance study of existing bandwidth estimation tools in non-simulated networks where various timing irregularities affect delay measurements. We find that when high-precision packet timing is not available due to hardware interrupt moderation, the majority of existing algorithms are not robust to measure end-to-end paths with high accuracy. We overcome this problem by using signal de-noising techniques in bandwidth measurement. We also develop a new measurement tool called PRC-MT based on theoretical models that simultaneously measures the capacity and available bandwidth of the tight link with asymptotic accuracy.

To my family

ACKNOWLEDGMENTS

I am sincerely grateful to my advisor Dr. Dmitri Loguinov for allowing me to conduct research with him. I am constantly amazed by his extraordinary ability in transforming seeming unsolvable problems into a tractable form, infinite knowledge on subject matters, and relentless attention to detail. His exceptional commitment to research and strong demand for excellence have guided me this far. I am truly grateful to his insightful advice, encouragement, and constant motivation throughout this work.

I would also like to thank professors Riccardo Bettati, Yoonsuck Choe, and Narasimha Reddy for their service on my advisory committee. Their insightful comments and constructive criticisms helped me improve my research. In addition, I am deeply grateful to Dr. Donald Friesen for giving me ample teaching opportunities during the course of this study. Having interactions with other students in laboratory or classroom environment have given me enjoyable experiences and have energized me throughout this endeavor.

Furthermore, I would like to thank my friends and fellow students at Texas A&M University for numerous discussions about various issues related to research, teaching, and lives. I sincerely thank current and former members of Internet Research Lab for being supportive of me during this work. I also thank to Inchoon Yeo for being a great friend and always being available whenever I need his assistance and help.

Last, but not least, I would like to thank my parents and my family members for their continuous support and encouragement. I am especially grateful to my wife for her endless support and love. Without her dedication and belief in me, this work would have been impossible.

TABLE OF CONTENTS

CHAPTER Page

CHAPTER Page

CHAPTER Page

LIST OF TABLES

TABLE Page

LIST OF FIGURES

FIGURE Page

FIGURE Page

FIGURE Page

CHAPTER I

INTRODUCTION

The Internet is a global information infrastructure, which facilitates users to access information using various networked (inter-connected) systems and applications. During the last decade, it has exhibited an explosive growth of the use of audio and video content that is provided by a variety of commercial, educational, and individual websites. As a result, real-time streaming that transports multimedia data has become an important part of the present Internet and attracted significant research effort from the industry and academic community. However, delivering high-quality of video to end users over the best-effort Internet is a challenging task since multimedia data is very sensitive to certain QoS (quality of service) characteristics (such as delay and packet loss) and quality of streaming video is highly subject to network conditions that often dynamically change over time. A fundamental issue in this area is how real-time applications cope with network dynamics (such as variation in delays due to network queuing and packet loss caused by congestion and/or other reasons) and adapt their operational behavior to offer a high-quality streaming environment to end users.

A. Objective and Approach

To address this issue, one dimension of work focuses on improving the best-effort model of the current Internet [9], [15], [19], [25], [29], [91] by supplementing it with

---

The journal model is *IEEE/ACM Transactions on Networking.*

some form of network QoS. These methods include DiffServ (Differentiated Services) [9], [15] and IntServ (Integrated Services) [12] proposals and various Active Queue Management (AQM) algorithms [19], [25], [29], [57], [91], offering prioritized services to different flows. The other dimension of related work is based on end-to-end methods that depend solely on end-system entities without network support and are associated with end-to-end rate and error control [7], [79], [103].

Although existing studies report certain success in improving the video streaming quality, none of them is sufficient to support a scalable, low-overhead, low-delay, and retransmission-free platform required by many current real-time streaming applications since they are not able to effectively utilize video-specific features such as *unequal* importance of multimedia packets, time limits in decoding of received packets, and an impact of packet loss on scalable video.

As an effort towards providing a high-quality scalable streaming environment that is free of retransmission, we investigate AQM-enabled schemes that can effectively utilize different importance of video packets and provide QoS services to flows with much less overhead than the mechanisms like DiffServ or IntServ. To understand and quantify how packet loss affects quality of scalable video, we analyze the performance of video streaming in best-effort networks. Based on this analysis, we propose a new streaming framework that allows applications to mark their own packets with different priorities and uses AQM inside routers to effectively drop less-important packets during buffer overflows. This framework achieves "optimal" transmission of video packets for a given packet loss rate without recovering packets lost during congestion.

Different from the above method, many real-time applications employ error concealment techniques to recover packets lost during transmission without retransmitting them. Forward-Error Correction (FEC) is widely used in streaming applications

to protect audio and video data in lossy network paths, which provides retransmission-free network services. However, it requires to send additional information with the data, which is in general not desirable for applications because of additional bandwidth requirements. FEC is seemingly beneficial for streaming services, but is not well understood how inclusion of redundant FEC packets affects the performance of scalable video and its resilience characteristics for a given packet loss rate. Thus, we examine FEC-protected transmission of video data and study the effect of packet loss within an FEC block and derive the asymptotic (i.e., assuming large sending rates) distribution of the number of lost packets per FEC block, which enables us to model the performance of video streaming with FEC protection. This result reveals a relationship between the FEC overhead rate and the end-to-end utility of received video and leads to optimal selection of FEC rate for a given packet loss rate and FEC block size.

In the second part of this thesis, we focus on measuring characteristics of network paths, which can be utilized by rate control algorithms for real-time traffic. Note that it is often believed that rate control is necessary for streaming applications to provide a high level of video quality to end users and avoid wasting network resources with packets that are eventually dropped in congested routers. With the development of scalable video such as MPEG-4 Fine Granular Scalability (FGS) [83], real-time video applications can implement rate control that re-scales the enhancement layer of the video stream to any desired bit rate. However, typical end-to-end congestion control mechanisms in the best-effort network rely on packet loss to probe for available bandwidth, which may cast a serious challenge to real-time flows because lost packets may need to be recovered before their decoding deadlines. This packet loss problem can be significantly improved by supplementing rate control mechanisms with bandwidth information discovered by other tools [64].

Given the importance of this topic and lack of stochastic analysis of this problem, we study packet-pair/train sampling techniques that have been used in the majority of existing bandwidth estimators and develop a generic queuing model of an Internet router. We then stochastically analyze bandwidth sampling process in the context of a single-congested node under non-negligible, non-stationary, and non-fluid cross-traffic conditions and derive an asymptotically accurate bandwidth estimator for both capacity and available bandwidth. This is one of the first methods that simultaneously estimates both types of bandwidth and is provably accurate. Following the single-hop analysis, we focus on developing an automated tool that measures both bandwidth metrics of a multi-hop path with asymptotic accuracy by utilizing recursive extension of the single-hop model. This automated tool relies on hop-by-hop measurement and adaptively selects probing parameters according to network conditions.

Finally, we note that all existing bandwidth estimation methods heavily rely on high-precision packet timing at measurement hosts. However, timing irregularities caused by OS (Operating System) scheduling jitter and hardware interrupt moderation are common in real networks, in which certain algorithms (e.g., [44]) reveal severe performance issues. On the other hand, theoretical models (e.g., [48], [61], [69], [75]) usually have probable convergence, but not have practical implementation to become a measurement tool. To address these issues related to realistic measurement environment, we develop a measurement tool *PRC Measurement Tool* (PRC-MT) based on asymptotically accurate bandwidth models of [61] and perform comparative study of existing tools in non-simulated networks.

B. Contributions

This work makes the following contributions:

- *A better understanding of how packet loss affects the performance of scalable video in best-effort networks.* We thoroughly study the effect of packet loss on quality of video under various network conditions. We define quality measure U, which is the percentage of received data in each frame that can be used for decoding the frame, and derive closed-form models of U under several general patterns of packet loss. These analytical results provide statistical insight into understanding the penalty inflicted on scalable code.

- *A new streaming framework that can provide QoS services to real-time flows.* This framework effectively utilizes unequal importance of video packets in rate control and achieves a near-optimal performance for a given network packet loss rate without recovering packets lost during transmission.

- *A new performance measure of the quality of scalable video with FEC protection and its resilience characteristics and a new method of optimally selecting FEC overhead rate for a given network packet loss rate.* As an alternative to retransmission-based error recovery, we investigate error concealment methods such as FEC, which is often used to protect multimedia data over lossy network channels. In FEC-protected video, the distribution of the number of lost packets and the location of the first loss in a block play an important role in understanding the effectiveness of FEC. Thus, we first study these two metrics and derive a model for each assuming large sending rates. Based on these results, we then develop models that enable us to understand optimality and resilience characteristics of scalable video under dynamically changing network conditions.

- *New bandwidth sampling techniques and measurement tools.* We study the problem of estimating bandwidth of network paths. First, we build a generic stochas-

tic queuing model of an end-to-end path and develop a new bandwidth sampling method in the context of a single-congested node, which can produce asymptotically accurate capacity and available bandwidth estimates of network paths under non-negligible and arbitrary cross-traffic. We next apply recursive extension of this single-hop model to a multi-hop path and develop an automated measurement tool that measures tight-link of the path by hop-by-hop probing. In addition, we develop a new measurement tool called PRC-MT based on theoretical models of [61] and conduct a comparative study of existing measurement tools in non-simulated networks where delay measurement is not accurate due to various timing irregularities. This study shows that PRC-MT significantly outperforms existing tools and reveals performance issues of certain algorithms such as Pathload when end-hosts delay generation of interrupts for network hardware. We overcome this timing problem by incorporating signal de-noising techniques into bandwidth measurement and develop a measurement tool called *Interrupt Moderation Resilient Pathload* (IMRP) that significantly improves Pathload's estimation reliability under a wide range of interrupt delays.

C. Dissertation Organization

The rest of the dissertation is organized as follows. In Chapter II, we describe background and related work of this thesis. Chapter III analyzes performance of scalable video streaming in best-effort networks and introduces a new streaming framework based on AQM. In Chapter IV, we examine performance of streaming video under FEC protection and discuss its optimality and resilience characteristics. Chapter V presents a stochastic analysis of bandwidth estimation in the context of a single-congested node and its extension to multi-hop paths, while in Chapter VI, we in-

vestigate practical issues of bandwidth measurement in real networks where delay measurements are not perfect due to hardware-related timing irregularity. Finally, we conclude this work and discuss future directions in Chapter VII.

CHAPTER II

BACKGROUND AND RELATED WORK

In this chapter, we review prior work in the areas of Internet QoS, error control, and bandwidth estimation.

A. Internet QoS Studies

Studies in this area supplement the best-effort model of the current Internet to provide a "better than best-effort" performance to end flows. Some of them focus on AQM (Active Queue Management) [19], [25], [29], [91] that provides unequal treatment to flows while controlling congestion and achieving fairness among the flows. Other work ranges from offering hard guarantees in the form of *Integrated Services* (IntServ) [12], [88], [106] to more scalable models such as *Differentiated Services* (DiffServ) [9], [15]. We overview some of these approaches that are related to the following two categories.

1. Priority QoS Methods

Several studies investigate the performance of video streaming over the DiffServ architecture. Gurses *et al.* [33] study streaming of temporally-scalable H.263+ video over a DiffServ network and propose three-color markers (TCM), which allow ingress routers to promote packets (i.e., increase their priority) or demote them based on their conformity to agreement between peering ISPs. Although this work provides flow differentiation at routers, it does not allow the end flows to effectively benefit from unequal priority of the packets since DiffServ can arbitrarily remark them according to ingress/egress policies of peering ISPs.

Shin *et al.* [89], [90] study the problem of "optimal" assignment of relative priority indexes to video packets depending on their impact on the quality of received video. Besides using a fairly complex packet prioritization scheme, the work does not discuss how the network should treat marked packets. Zhao *et al.* [108] employ MPEG-4 FGS for video streaming and use several computationally intensive packet prioritization schemes, but also without studying network support of the proposed architecture.

Among non-DiffServ methods, Tang *et al.* [98] present a rate control scheme called RCS for real-time traffic, which uses low-priority dummy packets to probe for new bandwidth at the beginning of a new connection and upon detection of data packet loss. When a new connection is started, the RCS source sends dummy packets with a predefined rate that can support for the highest quality of encoded video for the duration of one round-trip time (RTT). If the source detects loss of data packets at a current sending rate R of data packets, it sends dummy packets with the current sending rate R for one RTT. This method assumes priority queuing policies at intermediate routers on an end-to-end path to drop the dummy packets first during congestion.

Hurley *et al.* [38] propose ABE (Alternative Best Effort), which allows applications to choose between two types of service by marking their own packets as either green for low delay or blue for low packet loss based on the nature of their traffic. All green packets are served at each router within a certain predefined delay or otherwise dropped, while blue packets do not get special treatment from the routers. A similar approach is used in BEDS (Best Effort Differentiated Service) [26], which distinguishes two service classes similar to ABE using two RED (Random Early Detection) queues. BEDS employs small queue and aggressive RED drop probability and thresholds for low-latency service. On the other hand, it uses large queue and

less aggressive drop probability and thresholds for low-loss service.

Internet-2's QBSS (QBone Scavenger Service) [82] also provides service differentiation by allowing end flows to mark their own packets with the low-priority bit. However, the current QBSS does not support more than two priorities or directly benefit video traffic. Similarly, Li *et al.* [59] also suggests flow differentiation based on priorities assigned by applications, but without offering how real-time applications use different priorities in conjunction with rate control to improve their streaming quality.

2. Active Queue Management

Active Queue Management (AQM) schemes perform special operations in the router to achieve better performance for end flows. These operations include dropping random packets (e.g., RED), re-arranging the order in which packets are served (e.g., WFQ (Waited Fair Queuing)), and randomly marking packets from more aggressive flows (e.g., ECN (Explicit Congestion Notification)). While WFQ focuses on providing fairness to competing flows [19], [91], RED/ECN attempt to avoid congestion by randomly dropping or marking packets with a certain probability that increases with the level of congestion [25], [27], [29]. As such, these methods are not specifically tailored to multimedia applications and thus cannot significantly improve video quality of Internet streaming.

Additional studies combine congestion control with AQM to provide robust and smooth controllers since routers can detect network conditions more accurately than end systems. Lapsley *et al.* [57] study optimization-based congestion control and propose REM (random early marking) that carries congestion information using exponential marking based on user's utility. Katabi *et al.* [50] present XCP (eXplicit Congestion notification Protocol) that conveys information about the degree of con-

gestion in network paths to application sources using separate AQM controllers for utilization and fairness. Several other studies include Kelly-style optimization framework [46], [51], [53], [71] and Low's work [65], [66], [67], [68]. Note that none of those methods are coupled with multimedia streaming.

B. Forward Error Correction

FEC methods can recover lost data segments using extra information transmitted together with the data. We discuss some of the studies that report somewhat conflicting results on the benefits of FEC.

Altman *et al.* [3] study simple media-specific FEC for audio transmission and show that it provides little improvement to the quality of audio under any amount of FEC. This work uses media-specific FEC that is sometimes less effective in recovering lost packets than media-independent FEC [79]. Biersack *et al.* [7] evaluate the effect of FEC for different traffic scenarios in an ATM network. This study measures the reduction of loss rate for each source and reports that the performance gain of FEC quickly diminishes when all traffic sources employ FEC and the number of sources increases.

Alternative approaches aim to maximize the effect of FEC by choosing the proper amount of overhead and avoiding unlimited rate increase by keeping the combined rate $R + F$ (where R is the streaming rate of the application and F is the FEC overhead rate) equal to some constant S. Bolot *et al.* [11] present a media-specific method for adjusting FEC overhead under certain constraints on the total sending rate S. That work achieves close to optimal audio-specific subjective quality. Frossard *et al.* [31] propose a method that selects rates R and F using the distortion perceived by end-users. The method is fairly complex since it involves solving recurrence equations,

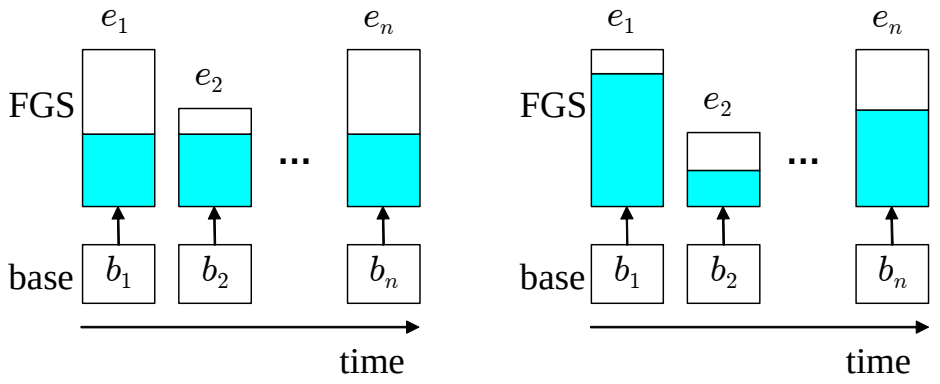

(a) Fixed size (b) Variable size

Fig. 1. Scaling of MPEG-4 FGS using fixed-size and variable-size frames.

which does not scale to large FEC block sizes.

Note that none of the above studies offers an explanation of how FEC overhead affects the performance of video applications for a given packet loss rate.

C. Structure of MPEG-4 FGS

Radha *et al.* [83] present a scalable video-coding method, which provides Fine-Grained Scalability (FGS) that is the streaming profile of the ISO/IEC MPEG-4 standard. It is a method of compressing residual video signals into a single enhancement layer that provides a flexible and low-overhead foundation for scaling the enhancement layer to match variable network capacity during streaming. The FGS layer is typically coded at some fixed (very large) bitrate and can be re-scaled to any desired bitrate by discarding a certain fraction of each FGS frame.

Fig. 1 illustrates the operation of MPEG-4 FGS. The figure shows individual frames from the base layer and the corresponding FGS layer. The shaded parts of the enhancement layer are the fractions of each frame taken by the server as part of its rate-scaling mechanism during streaming. Depending on the optimization goals

of the server, it can transmit a fixed fraction of each frame or use rate-distortion (R-D) models to dynamically determine the desired amount of data in each frame (interested readers are referred to [17] for more details).

D. Bandwidth Estimation

There are two types of bandwidth metrics: bottleneck bandwidth and available bandwidth. The former is the capacity of the slowest link (often called the *narrow* link) of an end-to-end path, while the latter represents the smallest unused bandwidth of links in the path. The link with the smallest unused bandwidth is referred to as the *tight* link. We discuss some of bandwidth estimation techniques that have been proposed in the literature separately below, starting with bottleneck-capacity estimators.

1. Capacity Measurement

Transmission delay of a packet over a link is solely determined by the capacity of the link and the size of the packet. Hence, capacity measurement techniques based on active probing focus on identifying transmission delay of probe packets that are sent over a link under investigation.

One of the earliest such tools is Pathchar [41], which is developed by Van Jacobson in 1997 and infers characteristics (such as capacity, latencies, and queuing delays) of individual links along an Internet path by exploiting the TTL field of IP packets. To probe each router, Pathchar sends multiple packets per packet size arranged in a linearly increasing order and drops them in a select router by TTL-limiting. Each of the ICMP error messages returned by a router due to TTL-expiration provides an estimate of round-trip time to that particular router. Recognizing the effect of cross-traffic on the measured RTT, Jacobson employs minimum filtering to keep the

minimum RTT sample per packet size. Capacity of each link can be estimated using the linearly increasing slope of the minimum RTTs as a function of probe-packet size.

More recent work exploits inter-packet dispersions (delays) sampled at the receiver to estimate the narrow-link capacity of a path rather than individual link capacities. The main idea is based upon an observation by Jacobson [42] in 1988 that the inter-arrival dispersion of two back-to-back packets (a packet-pair) injected into an idling network represents transmission delay of the second packet in the packet-pair over the narrow link. However, in real networks, inter-packet dispersions exiting from the narrow-link router will be distorted by cross-traffic at routers on the path. Specifically, if cross-traffic delays the first packet in the probing pair, the dispersion is compressed, while it is expanded when cross-traffic queues between the two probing packets. This variation (noise) in output dispersion due to random queueing of probe packets at intermediate routers is the primary source of error in bandwidth measurement. Thus, the majority of work in this area centers around how to filter out random queuing effects embedded in the measured output dispersions.

In order to facilitate removal of random noise in the output dispersion samples, several studies investigate different filtering techniques. Carter *et al.* [14] propose `bprobe` that sends a sequence of ICMP echo packets and measures inter-arrival times of returning successive packets. In this approach, the source sends a series of $n = 10$ packets of size q_i for each phase ϕ_i (where $i = 1, 2, \ldots, 7$ and $q_i < q_j$ if $i < j$). In each phase ϕ_i, the source computes a capacity range $[C_{k,i}, C_{k,i} + \epsilon]$ for each estimate $C_{k,i} = q_i/y_k$ between two consecutively returning packets k and $k + 1$, where y_k is the inter-arrival delay between returning packets k and $k + 1$ and ϵ is a certain small constant. Then, `bprobe` selects the most overlapping capacity range by iteratively intersecting the capacity ranges obtained in prior phases (starting from the last phase that uses the largest packet size) and produces a capacity estimate as the middle

point of the most overlapping capacity range. Other similar methods that use the most common output dispersion to estimate the capacity includes Nettimer [54] and PBM [78].

Recently, Dovrolis *et al.* [21] study characteristics of bandwidth estimation techniques that use packet-trains (packet-pairs are a special case of packet trains with train length $N = 2$) and model intermediate routers assuming a continuous fluid approximation for cross-traffic. This work shows that packet-pair histograms usually have many different modes (also observed in [78]) and that packet-train histograms become unimodal as the length N of packet-trains increases. This work also reports that the unique mode is centered at ADR (Asymptotic Dispersion Rate) that is lower than the capacity of the path. Based on this observation, the paper proposes a capacity estimator called Pathrate that uses two-phase probing and relies on histogram-based heuristics for actual bandwidth estimation. The two-phase probing methodology attempts to discover all local modes in the first phase by sending a large number of packet-pairs and continues the second phase unless the histogram of packet-pair samples is unimodal (which can happen in very lightly loaded paths).

In the second phase, Pathrate sends packet trains with length $N > 2$. If the resulting dispersions of packet train samples are not unimodal, then the probing source increases the train length N by a factor of 2 and repeats the process. When the resulting dispersions become unimodal, Pathrate's internal algorithm heuristically determines a range $[\zeta^-, \zeta^+]$ of the unique mode centered at ADR and selects, as the capacity estimate $\hat{C}$, the minimum local mode m_k that is higher than ζ^+ from a sequence of local modes $M = \{m_1, m_2, \ldots, m_M\}$ obtained in the first phase:

$$\hat{C} = m_k = \min(m_i \in M : m_i > \zeta^+). \tag{1}$$

This heuristic rule in (1) is based on the assumption that $\zeta^+ < C$ and the range of

the unique mode $[\zeta^-, \zeta^+]$ covers all the local modes between ADR and C.

In addition to histogram-based proposals, other methods include *packet tailgating* [55], where larger packets are followed by smaller packets to ensure a particular queuing pattern at the narrow link, and *packet cartouche* [35], where certain packets in a probe-train are dropped at select routers (using the TTL field) so as to ensure that the surviving packets can measure the capacity of individual routers and/or subpaths.

Besides the methods discussed above, a recent approach called CapProbe [49] is based on the assumption that if packets in a probe pair have arrived at the receiver with the smallest combined one-way delay, then the packets have not been queued at any intermediate routers in the path and thus the inter-packet delay of the probe pair reflects the transmission delay of the bottleneck link. Based on this assumption, CapProbe sends up to 100 packet-pairs and finds a minimum-delayed pair that satisfies the following condition:

$$\min_i(d_{1,i} + d_{2,i}) = \min_i(d_{1,i}) + \min_i(d_{2,i}), \tag{2}$$

where i represents packet-pair sequence number and $d_{1,i}$ and $d_{2,i}$ are the respective one-way delays of the first and second packets in i-th packet-pair. If such a minimum delay pair satisfying the above condition is not found from 100 probe samples, then CapProbe adjusts the size of probe-packets and repeat this process. Using minimum filtering, CapProbe is frequently able to obtain C with better accuracy and much quicker than the previous methods.

2. Available Bandwidth Measurement

Unlike link capacity, available bandwidth is an elastic metric that varies over time depending on the amount of cross-traffic on a network path. Research in this area

focuses on statistical nature of output inter-packet dispersions that reflect dynamics of cross-traffic through the path. Based on the analysis of dispersion information, various techniques have been proposed. One of the earliest approaches, called `cprobe` [14], directly relates the average of inter-arrival packet dispersions to the available bandwidth estimate $\tilde{A}$ by dividing the probe packet size by the average dispersion. Subsequent more sophisticated approaches (such as [37], [44], [72], [85], [96]) center around discovering a relationship between the input and output dispersions and how to utilize this relationship in actual measurement of the path.

Melander *et al.* [72] study the dependency between input rate R_I and output rate R_O of probe packets and derive the following expression for a single-link path under a fluid assumption on cross-traffic:

$$R_O = \begin{cases} R_I & R_I < A \\ \dfrac{R_I}{R_I + \lambda} C & R_I \geq A \end{cases}, \tag{3}$$

where C and A are the capacity and available bandwidth of the path, respectively. Based on this single-link model, this work proposes a new bandwidth probing technique called TOPP (Trains of Packet Pairs), which sends a sequence of packet-pair trains with increasing rates in subsequent trains. The input rates of probe-pair trains are selected in a predefined range and average output rates of each train are collected for further analysis. Re-writing (3), the paper obtains a linear relationship between two metrics R_I/R_O and R_I:

$$\frac{R_I}{R_O} = \begin{cases} 1 & R_I < A \\ \dfrac{R_I}{C} + \dfrac{\lambda}{C} & R_I \geq A \end{cases}. \tag{4}$$

Then, TOPP extracts from (4) both C and λ by exploiting the linear relationship between R_I/R_O and R_I using the collected average output rates and thus obtains

$A = C - \lambda$. In the multi-hop case, the paper reports that (4) can extract A assuming that available bandwidth of the second tight-link following the tight-link is obtained using empirical methods.

Different from TOPP, Pathload proposed by Jain *et al.* [44] adjusts input rates of packet-trains to infer available bandwidth of the path. This work is based on an observation that if the input probe rate is higher than the available bandwidth of the path, then one-way delays of packets in a probing-train exhibit an increasing trend. Pathload sends a fleet of n packet-trains, each of which consists of N back-to-back packets with inter-packet spacing x. After all packets in a train are received, the receiver performs a trend test on one-way delays of packets in the train. For the trend test, Pathload uses simple methods called *Pairwise Comparison Test* (PCT) and *Pairwise Difference Test* (PDT). The PCT metric represents how often consecutive one-way delays in a probe-train increase, while PDT metric quantifies how strong the difference between the first and last one-way delays in the data set is. After receiving all packets in n trains, the receiver determines the trend of the fleet based on the fraction of n trains that is of increasing or no-trend. When the trend information for a fleet is fed back to the source by the receiver, Pathload searches for an available bandwidth region by increasing or decreasing the input probing rate at the sender in a binary search fashion based on the trend information.

Another recent approach that is based on the one-way delay variation is Pathchirp [85], which focuses on reducing the measurement overhead of Pathload. In [85], Pathchirp uses packet-trains (called chirps) with exponentially decreasing inter-packet spacings and infers available bandwidth using the queuing delay signature of arriving chirps. The basic idea behind this method is that when a transmission rate $r_k = q/x_k$ of a packet k in the train reaches the available bandwidth of the path, then subsequent packets $j > k$ in the chirp will exhibit increasing queueing delay. Hence, the available

bandwidth of the path is the rate r_k of the packet at which the queueing delay starts increasing.

Considering bursty cross-traffic and non-monotonic increase of queueing delays, Pathchirp employs an empirical method to detect and interpret different patterns of queueing delay variations of probe packets in a packet-train. In reality, Pathchirp uses one-way delays in place of queuing delays since the latter is not easily measurable. It then classifies these delays into three groups based on variations of successive one-way delays and infers per-packet available bandwidth using heuristics, which leads to per-train available bandwidth after averaging the per-packet available bandwidth over the duration of that train.

Hu *et al.* [37] investigate a probing technique called IGI (Initial Gap Increasing) and PTR (Packet Transmission Rate) that iteratively probes for the so called *turning point* at which the input rate of probe-trains at the sender becomes equal to the output rate at the receiver. The method sends packet-trains with increasing inter-packet delay in each successive packet-train and finds an inter-packet spacing $\hat{x}$ of a certain packet-train, which equals the average output dispersion of that train. At the turning point $\hat{x}$, the IGI algorithm calculates cross-traffic intensity λ:

$$\lambda = \frac{\sum_{y_i > \max(\Delta, \hat{x})} C\,(y_i - \Delta)}{(N-1)\hat{x}}, \tag{5}$$

where C is an a-priori-known capacity of the tight-link, $\Delta = q/C$ (where q is the probe packet size), y_i is the output dispersion of the i-th pair in the train, and N is the train length. Then, available bandwidth of the path is $A = C - \lambda$. Different from IGI, PTR simply reports the average output rate at the turning point as the available bandwidth estimate of the path:

$$A = \frac{qN}{(N-1)\hat{x}}, \tag{6}$$

which is similar to TOPP [72].

Like IGI/PTR, Spruce [96] also requires an a-priori-known tight-link capacity C. Spruce sends packet-pairs with inter-packet spacing $\Delta = q/C$ and collects individual bandwidth samples A_i:

$$A_i = C\Big(1 - \frac{y_i - \Delta}{\Delta}\Big), \tag{7}$$

where y_i is the i-th measured packet spacing at the receiver. The algorithm averages samples A_i to obtain a running estimate of the available bandwidth. Note that Spruce emulates Poisson sampling by spacing different packet-pairs with exponential random delays.

CHAPTER III

MULTI-LAYER ACTIVE QUEUE MANAGEMENT FOR SCALABLE VIDEO STREAMING

In this chapter, we study video streaming over best-effort networks and analyze performance characteristics of scalable video under uniformly-random packet loss using MPEG-4 FGS as the example scalable video. Quantifying drastic quality degradation of streaming video in best-effort networks, we propose a new streaming framework that allows applications to mark their own packets with different priority and use multi-queue congestion control inside routers to effectively drop the less-important packets during buffer overflows. We describe priority AQM algorithms that provide "optimal" performance to video applications under arbitrary network loss and study a variation of Kelly's congestion control in combination with our framework.

A. Introduction

Typical video applications transport multimedia data that is highly sensitive to quality-of-service (QoS) characteristics (e.g., delay or packet loss) of their end-to-end path and often require better than simply best-effort services from the network before they can offer a high-quality streaming environment to end users. In response to this demand, significant research effort went into improving the best-effort model of the current Internet [9], [15], [19] , [25], [29], [91].

One dimension of this related work supplements the best-effort model with network QoS that guarantees a "better than best-effort" performance to end flows (these methods loosely fall under the umbrella of DiffServ [9], [15]). The other, more recent

dimension includes various Active Queue Management (AQM) algorithms [19], [25], [27], [29], [57], [91] that are able to provide QoS services to the flows with much less overhead than the more traditional mechanisms like DiffServ or IntServ [12].

However, none of the existing QoS methods provide a scalable, low-overhead, low-delay, and retransmission-free platform required by many current real-time streaming applications. To fill this void, we investigate novel AQM algorithms that not only can provide a provably "optimal" performance under random loss, but also possess very low implementation complexity.

One of the characteristics of video packets that does not match the best-effort service is that they often carry information of *different* importance. Thus, video applications can clearly differentiate between the more-important and the less-important packets. In all layered video coding schemes, the base layer is more important than the enhancement layer. Furthermore, the lower sections of the enhancement layer are more important than the higher sections because their loss renders all dependent data virtually useless. Thus, treating all video packets equally (as in the current best-effort Internet) usually leads to significant quality degradation during packet loss and low useful throughput during congestion, both of which cause video streaming to become unappealing in practical settings.

With the presence of unequal importance among video packets, the first goal of this work is to achieve "high end-user utility," which means that the majority of packets that are transmitted across the bottleneck link must carry *useful* information that can be decoded by the receiver. In video applications that use motion compensation and variable-length coding (VLC), a single lost packet in the base layer may affect several frames and render them all useless even though some of them arrive to the receiver without any loss. Furthermore, the enhancement layer is not immune to packet loss either since strong dependence between the coded data allows packet loss

to affect consecutive chunks of data that are significantly larger than those actually lost in the network. Hence, even under moderate packet loss, the bottleneck link may be used to transmit a large number of packets that eventually get dropped by the decoder.

In addition to high utility, many interactive applications (such as video telephony) further require low end-to-end delays to deliver high application-layer performance to the user. Additional problems with delays arise during retransmission of lost packets since all video frames have strict decoding deadlines. During heavy congestion (especially along paths with large buffers), the RTT is often so high that even the *retransmitted* packets are dropped in the same congested queues [64]. As a result, the receiver in such scenarios must ask for multiple retransmissions of each lost packet, which often causes the retransmitted packets to miss their decoding deadlines. Thus, our second goal is to provide a *retransmission-free* network service to video flows. This direction generally aligns well with FEC-based approaches, except our goal is to avoid all bandwidth overhead associated with error-correcting codes and occupy network channels only with the actual video data.

To improve the quality of video delivered over the Internet, we investigate a new streaming framework in which each application marks its own packets with different priorities and uses AQM inside routers to effectively drop the less-important packets during congestion. Such preferential (instead of random) dropping of packets allows the application to maintain a much higher quality of video for the end user compared to similar scenarios in a best-effort network. We also find that the use of multi-queue AQM allows scalable video applications to maintain high useful link utilization *without retransmitting any of the lost packets* or sending any error-correcting codes. Thus, we achieve both goals of high utility and low end-to-end delay.

While our implementation relies on Kelly's utility-based controllers [51], it is

important to realize that the proposed framework can be used with any congestion control (including end-to-end methods such as AIMD, TFRC, or even TCP) and can be deployed in the current Internet with minimum modifications to the existing infrastructure.

B. Analysis of Video Streaming

In the first part of this section, we investigate probabilistic characteristics of video streaming performance under random packet loss. We study a best-effort network, in which routers drop video packets uniformly and randomly during congestion. Recall that many studies of Internet QoS attempt to improve TCP performance by changing drop behavior of the network from bursty to uniformly random [27], [29]. Thus, it can be argued that future networks will deploy such packet drop mechanisms more often than the current Internet. Therefore, we assume an independent loss model with exponential tails of burst-length distributions (rather than a heavy-tailed model, which is commonly observed in FIFO queues) and use it throughout this chapter.

In the second part of this section, we overcome the drastic reduction of video quality in best-effort streaming and show that *preferential* packet drops can in fact provide "optimal" performance to the end-user. Thus, following the best-effort analysis, we study priority-based AQM that supports preferential streaming and compare it with the best-effort scheme.

Finally, we should note that although quality degradation of multimedia streaming in best-effort networks is well documented, the novelty of this section lies in the derivation of the exact closed-form expressions for the penalty inflicted on scalable flows under uniform packet loss and the novel associated discussion that is also useful for understanding "optimality" of AQM in later sections.

1. Best-Effort Streaming

We investigate the effect of random packet drops on video quality using the example of MPEG-4 FGS (similar results apply to non-FGS layered coding)[1]. We start by examining the probabilistic characteristics of packet drops in an FGS frame, derive the expected amount of *useful* data recovered from each frame, and define the effectiveness of FGS transmission over a lossy channel.

Assume that long-term network packet loss p can be modeled by a sequence of independent Bernoulli random variables X_i. Each X_i is an indicator function that determines whether packet i is lost or not: $X_i = 1$ *iff* packet i is dropped in the network. Then $P(X_i = 1) = 1 - P(X_i = 0) = E[X_i] = p$ is the average packet loss. Even though this model is a great simplification of real networks and results in the probability of obtaining a burst of length k proportional to e^{-k} (i.e., the tail of burst sizes is exponential), it suffices for our purposes (see the discussion on RED/ECN ([27], [29]) earlier in this section).

Next assume that FGS frame sizes H_j are measured in packets and are given by *i.i.d.* random variables with a probability mass function (PMF) $q_j = P(H_j = k), k = 1, 2, \ldots$. The exact distribution of $\{H_j\}$ depends on the frame rate, variation in scene complexity, and the bitrate of the sequence. The question we address next is what is the expected amount of useful packets that the receiver can decode from each frame under p–percent random loss? Thus, our goal is to determine the expectation of Y_j, which is the number of consecutively received packets in a frame j.

Lemma 1. *Assuming independent Bernoulli packet loss with probability p, the ex-*

[1]Further note that motion-compensated enhancement layers suffer even more degradations under best-effort loss and are not modeled in this work. However, the expected amount of improvement from QoS in such schemes is even higher than that in FGS.

pected number of useful packets in an FGS frame is:

$$E[Y_j] = \frac{1-p}{p} \sum_{k=1}^{\infty} \left(1 - (1-p)^k\right) q_k. \tag{8}$$

Proof. Assume that G_j is the random distance from the beginning of frame j to the next packet-loss event. Then, all G_j are geometric random variables with respect to each frame j and can assume any integer value in the range $[1, \infty)$. Note that when the first packet-loss location G_j is no more than H_j, the decoder recovers exactly $G_j - 1$ packets from the frame. Otherwise, all H_j packets are recovered.

Next, taking a conditional expectation of Z_j, we can write:

$$E[Y_j|H_j = k] = \sum_{i=1}^{k} (i-1)p_i + \sum_{i=k+1}^{\infty} k p_i, \tag{9}$$

where $p_i = P(G_j = i) = q^{i-1}p$ is the geometric PMF of G_j and $q = 1 - p$. Then, (9) becomes:

$$\begin{aligned} E[Y_j|H_j = k] &= p \sum_{i=1}^{k} (i-1)q^{i-1} + k \sum_{i=k+1}^{\infty} q^{i-1}p \\ &= p \sum_{i=1}^{k} (i-1)q^{i-1} + k\Big(1 - p \sum_{i=1}^{k} q^{i-1}\Big). \end{aligned} \tag{10}$$

Substituting $l = i - 1$ into (10), we get:

$$\begin{aligned} E[Y_j|H_j = k] &= p \sum_{i=1}^{k} l q^l + k\Big(1 - p \sum_{l=0}^{k-1} q^l\Big) \\ &= pq \sum_{l=0}^{k-1} \frac{d}{dq} q^l + k\Big(1 - p\frac{1-q^k}{1-q}\Big) = \frac{1-p}{p}\Big(1 - (1-p)^k\Big). \end{aligned} \tag{11}$$

Expanding the conditional expectation in (11) to arbitrary frame sizes H_j, we obtain (8). □

Throughout the rest of the chapter, we examine one particular distribution of

Table I. Expected Number of Useful Packets

H	Packet loss p	Simulations	Model (12)
100	0.0001	99.49	99.49
100	0.01	62.78	62.76
100	0.1	8.99	8.99

$\{H_j\}$, in which all FGS frames have the same fixed size H. Under these conditions, (8) becomes:

$$E[Y_j] = \frac{1-p}{p}\left(1-(1-p)^H\right). \tag{12}$$

This model is compared to actual simulation results in Table I for $H = 100$. As the table shows, even under a reasonably low packet loss of 1%, the expected number of useful packets in each frame is only 62; however, the decoder successfully receives (on average) a total of 99 packets per frame. Furthermore, under moderate loss of 10%, only 9 useful packets are recovered from each frame, while a total of 90 packets per frame are transmitted over the bottleneck link.

Furthermore, as streaming rates become higher (and H becomes larger), $E[Y_j]$ tends to $(1-p)/p$ and the recovered (useful) percentage of each frame tends to zero. This is shown in Fig. 2 (left) for $p = 0.1$, in which the number of useful packets in the best-effort case quickly saturates at $(1-p)/p = 9$ as H becomes large. The same side of the figure also plots the number of packets that could have been recovered in the "optimal" case, where all $H(1-p)$ packets are useful in decoding (which is clearly the best possible scenario under p–percent packet loss).

To quantify the effect of FGS packet transmission on video quality, we define *utility* U of received FGS video as the ratio of the average number of FGS packets used in decoding a video frame (i.e., $E[Y_j]$) to the total number of received FGS

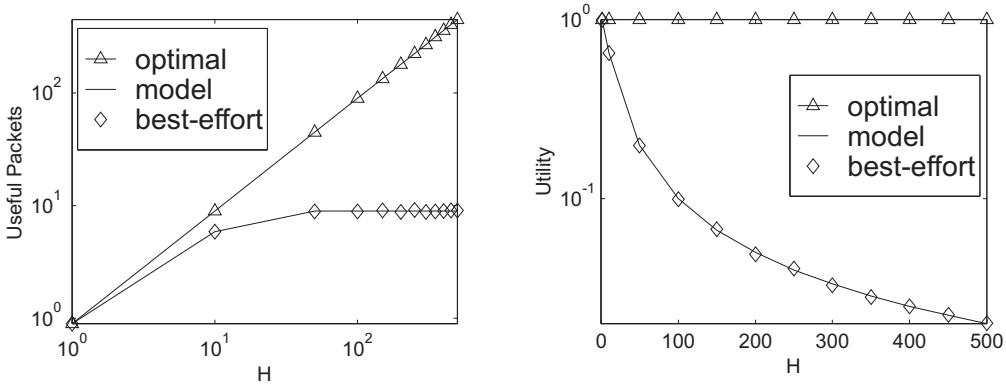

Fig. 2. The number of useful FGS packets in each frame (left). Utility of received video (right).

packets (i.e., $H - pH$):

$$U = \frac{E[Y_j]}{H(1-p)} = \frac{1-(1-p)^H}{Hp}, \tag{13}$$

where the last expansion holds for the constant frame size model in (12). For instance, we get $U = 0.1$ with $p = 0.1$ and $H = 100$, which means that only 10% of the received FGS packets are useful in enhancing the base layer. This result is further illustrated in Fig. 2 (right), which plots the utility of best-effort streaming and the "optimal" utility for different values of H and $p = 0.1$. As the figure shows, the utility of best-effort video drops to zero inverse proportionally to the value of H, which means that as $H \to \infty$ (i.e., sending rates become higher), the decoder receives "junk" data with probability 1.

2. Optimal Preferential Streaming

In this section, we discuss the "optimal" streaming method that can provide high end-user utility and significant quality improvement along AQM-enabled network paths. In order to achieve the maximum end-user utility (i.e., $U = 1$), routers must drop the upper parts of the FGS layer during congestion and transmit only the lower parts since

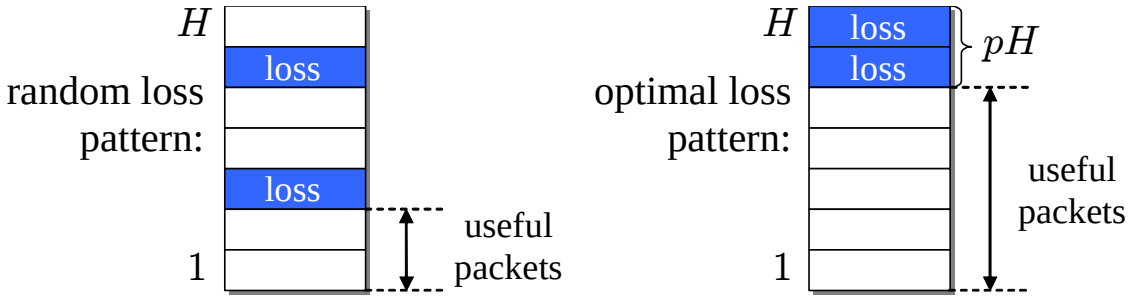

(a) Random loss (b) Ideal loss

Fig. 3. Useful data in each frame under random and ideal loss patterns.

consecutive lower portions of the FGS layer can enhance the base layer, while any gaps in the delivered data typically render the remainder of the layer useless. Fig. 3 depicts the difference between the ideal and random drop patterns in an enhancement frame and shows that all dropped packets must occupy the upper portion of the FGS layer to achieve optimality.

Since for a given drop rate p, the "optimal" AQM scheme drops pH packets from the upper part of the FGS frame and protects the remaining $H(1-p)$ packets, all received FGS packets are consecutive and thus can be used to enhance the base layer. Hence, the utility of this framework is always one regardless of the values of p or H. For example, assuming the same scenario as in the best-effort case ($p = 0.1$, $H = 100$), preferential streaming delivers *ten times more useful packets* than best-effort streaming. The main question now is whether optimal streaming is possible in practice and how to achieve it using scalable AQM methods. We address this issue next.

C. Preferential Video Streaming Framework

In this section, we introduce a new video streaming framework called *Partitioned Enhancement Layer Streaming* (PELS) that operates in conjunction with priority-queuing AQM routers in network paths. In the PELS framework, applications partition the enhancement layer into two layers and voluntarily mark their packets using different priority classes, allowing the network routers to discriminate between the packets based on their priority (no per-flow management is required).

Recall that coded video frames carry information that has different importance to the end user – the lower layers are more sensitive to packet loss than the higher layers. The base layer (being most sensitive) is *required* for displaying video appropriately at the receiver and thus is transmitted using the highest priority class. This ensures that the base layer is dropped only when the entire FGS layer is discarded by the routers.

The reason for splitting the FGS layer into two priorities is also simple to understand. Bytes in the lower part of the FGS layer are more important than those in the higher part because the former includes the information needed to properly decode the latter. Due to this nature of FGS streams, dropping packets randomly (as in the best-effort network) does not properly protect the lower parts of FGS even under moderate congestion. Hence, to protect the lower portions of FGS frames and drop the upper parts, preferential treatment of not only the base layer, but also the enhancement layer is highly desirable.

1. Router Queue Management

We discuss queuing disciplines necessary to support PELS and how applications should assign priority to their packets. To separate video traffic from the rest of

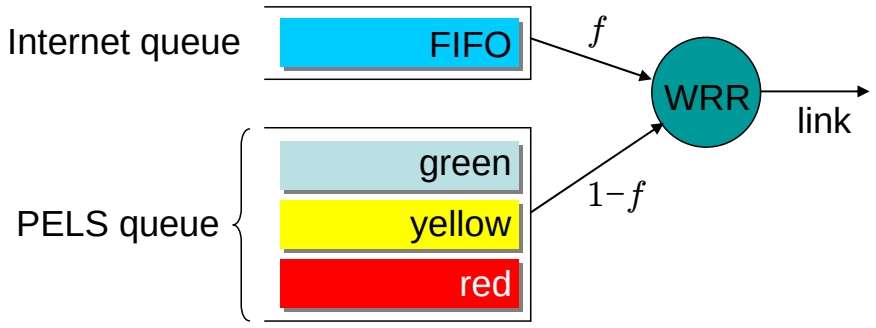

Fig. 4. Router queues for PELS framework.

the flows, the proposed PELS architecture must maintain in each network router two types of queues – the PELS queue and the Internet queue. The PELS queue is further subdivided into green, yellow, and red priority queues to service marked multimedia packets, while the Internet queue serves all other (non-multimedia) Internet traffic in a regular FIFO fashion. To ensure that network bandwidth is shared "fairly" between PELS applications and other Internet traffic, we employ weighted round-robin (WRR) scheduling between the PELS and Internet queues. Recall that WRR can provide a desired level of fairness between several types of traffic by allocating a certain fraction of the outgoing link to each queue as shown in Fig. 4. This allows de-centralized administrative flexibility in selecting the weights and assigning proper "importance" to different classes of traffic.

It is easy to see that the PELS queue must employ a *strict* priority queuing discipline to maximize the resulting video quality for a given total throughput budget. Since the higher parts of the FGS frame cannot be decoded without the presence of the lower parts, each router has no reason to transmit the higher parts before sending the lower ones. This implies that network routers must use queuing mechanisms that do not allow low-priority packets to pass until *all* high-priority packets are fully transmitted. Note that, in general, strict priority queueing is frowned upon since

it leads to starvation in low-priority queues and denial-of-service effects for certain flows; however, this situation does not arise in PELS since each flow sends a certain amount of high-priority (i.e., green) packets and always receives non-negligible service from the network. In fact, starvation in low-priority (i.e., red) queues is equivalent to 100% loss in these queues and has very little effect on the resulting quality since it affects only the upper parts of each enhancement frame (more on this below).

Since PELS application sources can arbitrarily mark their packets, we must next ensure that no end-user gains anything by marking *all* of its FGS packets with high priority (i.e., green). Such "misbehaving" sources will increase congestion in the green queues, which will result in (uniform) random losses in their base layers and will quickly degrade the resulting quality of their own video. Similarly, end-flows have little incentive in sending too many yellow packets or being congestion-indifferent. Thus, if each application is a selfish, independent entity that attempts to maximize the utility of its video at the receiver, it will send red packets to probe for congestion and back-off (i.e., reduce the total sending rate) during the loss of any red packets to protect the yellow/green queues from upcoming congestion.

We should make several other interesting observations. First, notice that PELS assumes certain stationarity of the end-to-end path (all packets take the same route) and the presence of PELS-enabled AQM at the *bottleneck* router. The former assumption is common to all flows using congestion control (i.e., multi-path routing and/or route changes make the control loop produce unpredictable results). The latter assumption is very relaxed since it does not require *all* routers to deploy PELS at the same time. Our second observation is that priority queuing in PELS is low-overhead, flexible, does not require support from DiffServ or use of per-flow management, and can be implemented using priority queues available in many existing router hardware/software solutions. Finally, PELS does not require communication between

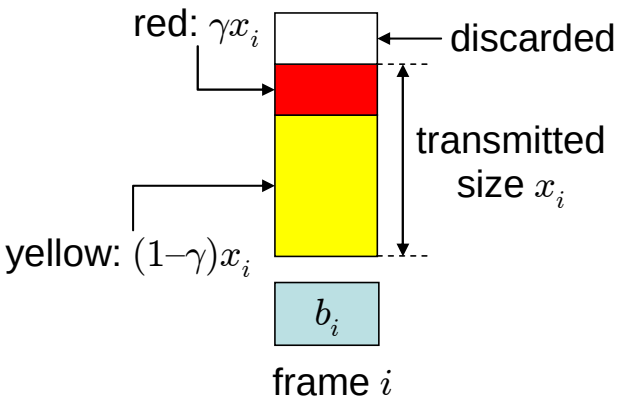

Fig. 5. Partitioning of the FGS layer into two layers and PELS coloring of FGS packets.

routers and leaves the decisions of how to mark packets to the end-user (i.e., pushes complexity outside the network).

2. FGS Partitioning and Packet Coloring

In a practical network environment (such as the Internet), packet loss and available bandwidth are not constant and change dynamically depending on cross traffic, link quality, routing updates, etc. Hence, streaming servers must often probe for newly available bandwidth as part of congestion control and continuously send low-priority packets under the assumption that these probes (and only they) will get lost during congestion.

Fig. 5 illustrates one possible partitioning of FGS bytes into two priority classes (i.e., yellow and red) that can achieve "optimal" utility discussed in section 2.. The figure shows that the server sends x_i bytes from each enhancement frame i (where x_i is given by congestion control and is derived from R_{max} using rate scaling algorithms [17]). The transmitted section of each FGS frame is divided into two segments – the lower segment of size $(1-\gamma)x_i$ is all yellow and the upper segment of size γx_i is all red. The division into red and yellow packets depends on how conservative (many

red packets and large γ) or optimistic (few red packets and small γ) the server wants to be.

In an ideal network with stationary packet loss p in the enhancement layer, the server can select γ such that γx_i is equal to px_i. This will ensure that *all* red packets are lost and that exactly $(1-p)x_i$ yellow packets are recovered for decoding (this is the best scenario under any circumstances). In practice, however, keeping red packet loss p_R at 100% is not feasible since any slight increase in p (caused by a new flow joining the network or change in network conditions) will "spill" the loss into the yellow queue, effectively creating a best-effort FIFO situation in the yellow queue. Thus, proper and dynamic selection of γ is important (see the next section).

The other issue to address is congestion control. Even though red queues can be used to isolate increasing packet loss p without reducing the sending rate of the flow (i.e., by proportionally increasing γ), the resulting situation will lead to "trashing" the network with numerous red packets that eventually get dropped at the bottleneck link. To prevent waste of bandwidth on the path to the bottleneck, the server must implement elastic congestion control and reduce its rate whenever it loses either yellow or red packets (the loss of green packets means that there is not enough bandwidth to support the base layer and no meaningful streaming can continue). Since all flows in our model use PELS and the same congestion control, they all back-off during the loss of red packets and keep the amount of "waste" to a minimum.

3. Selection of γ

Recall that partitioning of the FGS layer into yellow/red packets attempts to ensure that only the upper sections of each frame are dropped during congestion; however, the performance of PELS depends on the selection of γ and the level of congestion at the bottleneck link. In order for PELS to be effective, we must ensure that when

flows probe for new bandwidth, they do not incur such high levels of congestion as to force packet loss in the yellow priority queue. Hence, given any control interval k with packet loss $p(k)$ in the FGS layer, how can the server make sure that there will be no loss among *yellow* packets during interval $k+1$?

Intuitively, γ should be adjusted according to packet loss measured during interval k to keep the resulting red loss $p_R = px_i/\gamma x_i = p/\gamma$ at a certain threshold p_{thr}. The most optimistic approach suggests $p_{thr} \approx 1$ (which leads to the largest utility $U \approx 1$) and the most pessimistic approach keeps $p_{thr} \approx p$ (which leads to the best-effort utility in the enhancement layer).

Based upon these observations, we seek a middle ground in which p_{thr} can be stabilized between 70 and 90% using simple closed-loop control methods that adjust γ based on the following rules:

- Increase γ when p increases
- Decrease γ when p decreases.

Considering this general intuition, we next investigate a single proportional controller that adjusts γ based on the measured packet loss $p(k)$ and target red packet loss p_{thr}:

$$\gamma_i(k) = \gamma_i(k-1) + \sigma(p_i(k-1)/p_{thr} - \gamma_i(k-1)), \tag{14}$$

where index i represents flow number, $p_i(k)$ is the measured *average* packet loss in the entire FGS layer for flow i during interval k, and σ is controller's gain parameter. Note that $(1-p_{thr})\gamma x_i$ is the amount of cushion left by the server for the yellow packets. For example, $p_{thr} = 0.75$ means that 25% of the red queue works to protect the yellow queue against sudden (unexpected) increase in packet loss.

Note that, in general, the measurement of $p_i(k)$ is coupled with congestion control and should be provided by its feedback loop (we discuss this in section D.). Next

notice that the controller in (14) is stable if the following is satisfied.

Lemma 2. *The controller (14) is stable* iff $0 < \sigma < 2$.

Proof. Taking the z-transform of (14) we obtain the following:

$$\Gamma_i(z) = z^{-1}\Gamma_i(z) + \sigma\Big(z^{-1}P_i(z)/p_{thr} - z^{-1}\Gamma_i(z)\Big) = \frac{\sigma z^{-1}P_i(z)/p_{thr}}{1-(1-\sigma)z^{-1}}. \tag{15}$$

The poles of system (14) are the roots of its characteristic equation $1-(1-\sigma)z^{-1} = 0$ (notice that $P_i(z)$ does not depend on $\Gamma_i(z)$). Thus, the system has single pole $z = 1-\sigma$. For the control system to be stable, the absolute value of z must be less than 1 (i.e., $|z| < 1$). This leads to $0 < \sigma < 2$ and concludes the proof. □

Note that in a real network environment, feedback delays are often involved. Assuming arbitrary round-trip delay D_i for flow i, (14) becomes:

$$\gamma_i(k) = \gamma_i(k-D_i) + \sigma(p_i(k-D_i)/p_{thr} - \gamma_i(k-D_i)). \tag{16}$$

Then we have a stronger version of the previous lemma that shows stability of the resulting controller under arbitrary delays.

Lemma 3. *The controller (16) is stable* iff $0 < \sigma < 2$.

Proof. The z-transform of (16) is:

$$\Gamma_i(z) = z^{-D_i}\Gamma_i(z) + \sigma\Big(z^{-D_i}P_i(z)/p_{thr} - z^{-D_i}\Gamma_i(z)\Big) = \frac{\sigma z^{-D_i}P_i(z)/p_{thr}}{1-(1-\sigma)z^{-D_i}}. \tag{17}$$

The new pole is given by $z = (1-\sigma)^{1/D_i}$, which also leads to stability condition $0 < \sigma < 2$. □

Next, we derive the effect that (14)-(16) have on the packet loss in the red queues.

Lemma 4. *Assuming stationary packet loss p, both controllers (14)-(16) converge red packet loss p_R to p_{thr}.*

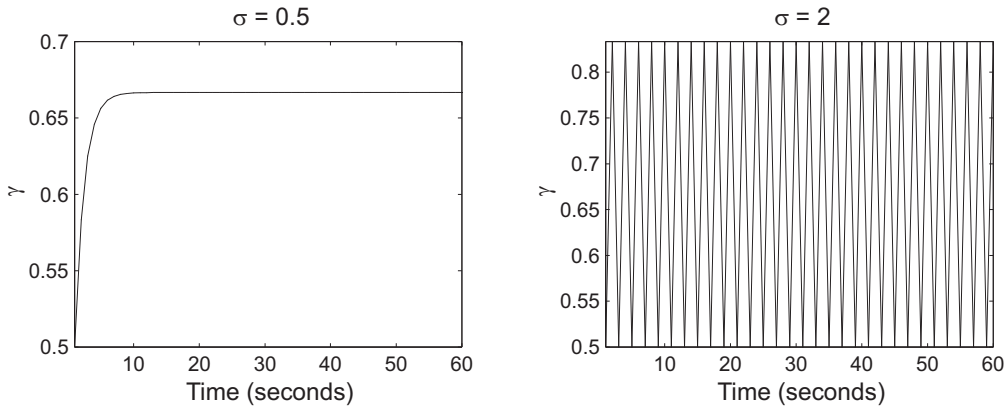

Fig. 6. Stability of γ with different σ.

Proof. Since $\gamma(k)$ does not change with time in the steady state, $\gamma(k) = \gamma(k-1) = \gamma^*$. From (14), we get:

$$\gamma^* = \frac{p^*}{p_{thr}}, \tag{18}$$

where p^* is the stationary packet loss of the network. Since the red packet-loss can be expressed as $p_R(k) = p(k)/\gamma(k)$, the stationary red packet-loss is given by:

$$p_R^* = \frac{p^*}{\gamma^*}. \tag{19}$$

Substituting γ^* from (18) into (19), we get $p_R^* = p_{thr}$. □

To illustrate that selection of σ is important, but not drastically difficult, Fig. 6 depicts the behavior of $\gamma(k)$ with different σ (we use a heavy-loss case with $p = 0.5$ and $p_{thr} = 0.75$ in this example). As the figure shows, $\gamma(k)$ is stabilized at the stationary point $\gamma^* = p/p_{thr} \approx 0.67$ when $\sigma = 0.5$, while it is unstable when $\sigma = 2$.

The resulting utility of received video in PELS under dynamically changing γ is lower-bounded by the following (assuming that only yellow packets are recovered from the FGS layer):

$$U \geq \frac{H(1-\gamma)}{H(1-p)} = \frac{1-p/p_{thr}}{1-p}. \tag{20}$$

Thus, the utility of PELS is at least 0.96 for $p = 0.1$ and $p_{thr} = 0.75$ and at least 0.996 for $p = 0.01$ and the same threshold. Although PELS does not achieve "optimality" for $p_{thr} < 1$, it comes very close to it and at the same time avoids the pitfalls of the optimal method.

D. Congestion Control for Video

Congestion control is necessary for streaming applications to provide a high level of video quality to end users and avoid wasting network resources with packets that are eventually dropped in congested queues. Many control methods dynamically adjust the sending rate of end-flows based on network feedback and aim to achieve a stable tradeoff between under-utilization of resources and network congestion (i.e., packet loss).

Recent studies have focused on developing smooth congestion control schemes for multimedia streaming (e.g., TFRC [28] and binomial algorithms [6]) after AIMD (Additive Increase, Multiplicative Decrease) was unofficially found to be "unacceptable" for video streaming due to its large rate fluctuations. Nonetheless, these new control schemes often do not have stationary points in the operating range of typical applications and continuously oscillate [107].

Among many recent game-theoretic and optimization methods [46], [51], [53], [65], [67], [68], [66], [71], we selected Kelly's congestion control framework (called *proportional fairness* [51]), since it is stable, efficient, and fair under various network conditions. In this section, we study Kelly's controls, apply them to PELS streaming, and investigate whether their performance provides the necessary foundation for

achieving our goals of smooth, high-quality video streaming.

In general, it is important to remember that PELS is *independent* of congestion control and can be utilized with any end-to-end or AQM scheme. Thus, the complexity of implementing Kelly controls inside routers should be de-coupled from that of PELS since the latter does not require the presence of the former. Kelly controls are studied here as an example of one possible scheme that supplements PELS with smoothly changing rates. We leave the study of additional methods for future work.

1. Continuous-Feedback Control

Although Kelly's controls have attracted significant attention, their application to video streaming is limited to [17] in which Dai *et al.* use an application-friendly form of the controller given by:

$$\frac{dr(t)}{dt} = \alpha - \beta p(t) r(t), \tag{21}$$

where $r(t)$ is the rate of the flow, $p(t)$ is packet loss (feedback from the network), α and β are gain parameters. Since in real applications, rate adjustment is not continuous, we use a discrete form of (21). However, notice that the classical discrete Kelly control studied by [46] and others shows stability problems when the feedback delay becomes large [107]. Hence, we employ a slightly modified discrete version of this framework called *Max-min Kelly Control* (MKC) [107]:

$$r_i(k) = r_i(k - D_i) + \alpha - \beta r_i(k - D_i) p_l(k - D_i^{\leftarrow}), \tag{22}$$

where $r_i(k)$ is the rate of source i during interval k, $D_i^{\leftarrow}$ is the backward delay from the router to source i, D_i is the round trip delay of flow i, and packet loss p_l is fed back from the *most-congested* resource l (this provides max-min resource allocation instead of proportionally fair). The packet loss is computed inside router l at discrete

intervals and inserted into all passing packets:

$$p_l(k) = \frac{\sum_{j \in S_l} r_j(k - D_j^{\rightarrow}) - C_l}{\sum_{j \in S_l} r_j(k - D_j^{\rightarrow})}, \tag{23}$$

where S_l is the set of sources sending packets through router l, $D_j^{\rightarrow}$ is the forward delay from source j to the router, and C_l is link capacity of router l. The stability of system (22)-(23) is formalized as follows.

Lemma 5. *System (22)-(23) is stable under heterogeneous delays* iff $0 < \beta < 2$.

Proof. See [107]. □

We apply (22) for rate control in PELS streaming and investigate its control characteristics including:

- Convergence to a single stationary point
- Fairness between flows.

From (22) and (23), we next derive stationary rates r_i^* of end flows in the equilibrium point and show that (22) has no oscillations in the steady state.

Lemma 6. *Regardless of the feedback delay, the stationary rate r_i^* of each flow is:*

$$r_i^* = \frac{C_l}{N} + \frac{\alpha}{\beta}. \tag{24}$$

Proof. Since the rate of each flow does not change with time in the steady state, $r_i(k) = r_i(k - D_i) = r_i^*$. Using this observation in (22) we get

$$r_i^* = \frac{\alpha}{\beta p^*}, \tag{25}$$

where p^* is the stationary packet loss. Since in the steady state, all flows share the bandwidth equally (i.e., $r_i^* = r_j^* = r^*$), we have $p^* = \frac{Nr^* - C}{Nr^*}$ from (23). Substituting $p^* = \frac{Nr_i^* - C}{Nr_i^*}$ in (25) and rearranging it we get (24). □

Thus, unlike AIMD or TCP, MKC does not penalize flows with higher RTT and further converges to a single stationary point with no oscillation.

Next notice that priority queueing in PELS imposes increased delays on red packets and that the utilization of each priority class directly affects delay characteristics of *all* queues with lower priority. Since green packets have much smaller queuing delays than yellow or red packets, it is tempting to provide feedback only in green packets. However, since the base layer is sent at significantly lower rates than the enhancement layer, this method introduces unnecessary feedback delays due to large inter-packet spacing of the base layer. Thus, it is easy to conclude that network feedback must be inserted by the router into *all* passing packets (regardless of their color) for timely delivery to the end flows. Below, we discuss methods to discard out-of-sequence (i.e., outdated) feedback that may arrive in red/yellow packets.

2. PELS Implementation

We implemented new agents and a priority-based AQM mechanism for PELS streaming in the `ns2` network simulator [73]. PELS application sources mark their packets with three priority levels (i.e., green, yellow, and red) and employ MKC for rate control. Computation of packet loss $p(k)$ is performed by the router on a discrete time scale of T time units and then injected into the header of each packet passing through the router (note that feedback information is a queue-specific metric). Each new computation of $p(k)$ increases router's local epoch number z to prevent sources from reacting to the same feedback more than once as well as to suppress outdated values of $p(k)$ created by re-ordering inside PELS queues. Label (*router ID*, z, $p(k)$) is provided to end flows through the header of the packets queued at the bottleneck link.

Once received by the end-user, feedback $p(k)$ is sent in ACKs to the source, which

applies rate adjustments according to (22) as long as it has not seen this feedback before. The use of epoch numbers allows the source to keep the frequency of its control loop in sync with that of the router and ensures stability of the resulting system.

We next describe the above two algorithms in more detail. Upon arrival and queuing of a packet j, the router increments its local counter S by the size s_j of the packet: $S = S + s_j$. Then once every T time units, the router computes new total rate R, new packet loss p, increments its epoch number z, and resets the byte counter:

$$R = \frac{S}{T}, \quad p = \frac{R - C}{R}, \quad z = z + 1, \quad S = 0. \tag{26}$$

To verify the "freshness" of feedback, each PELS source i checks feedback sequence number z in the acknowledgment and ignores feedback with z less than or equal to its current epoch number z_i; otherwise, z_i is set to z and a new sending rate is computed using (22). When there are multiple routers along an end-to-end path, each router compares its p_l with that inside arriving packets and overrides the existing value only if its packet loss is larger than the current loss recorded in the header. End flows use the *router ID* field to keep track of feedback freshness and react to possible shifts of the bottlenecks.

Selection of interval T depends on the desired responsiveness of the PELS framework to network conditions, but does not affect stability of the system as a whole. To analytically reflect the implementation of the PELS framework where the router purposely delays its feedback by T units, we need to modify the model of packet loss in (23) to become:

$$p_l(k) = \frac{\sum_{j \in S_j} r_j(k - T - D_j^{\rightarrow}) - C_l}{\sum_{j \in S_j} r_j(k - T - D_j^{\rightarrow})}. \tag{27}$$

Stability of system (22)-(27) is proved using the same arguments as in Lemma 5 [107]

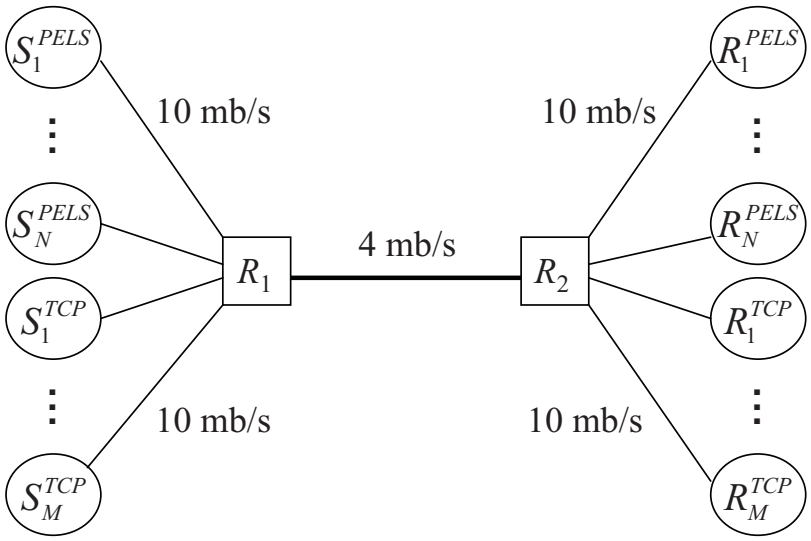

Fig. 7. Simulation topology.

and is omitted from this work.

E. Simulation Results

In this section, we present simulation results of PELS including the properties of $\gamma(k)$, MKC congestion control, PELS queuing delay, and PELS video quality. We start by describing the simulation setup.

1. Simulation Setup

For `ns2` simulations, we use a simple bar-bell topology with multiple PELS and TCP sources connecting to a single bottleneck link. As shown in Fig. 7, the capacity of the bottleneck is 4 mb/s, while the rest of the links are 10 mb/s. In all simulations, one video frame (63,000 bytes including the base layer) consists of 126 packets, 500 bytes each (these numbers are derived from MPEG-4 coded CIF Foreman). We mark 21 packets in each frame as green to protect the base layer of the sequence.

Recall that router queues in our framework completely separate the PELS flows

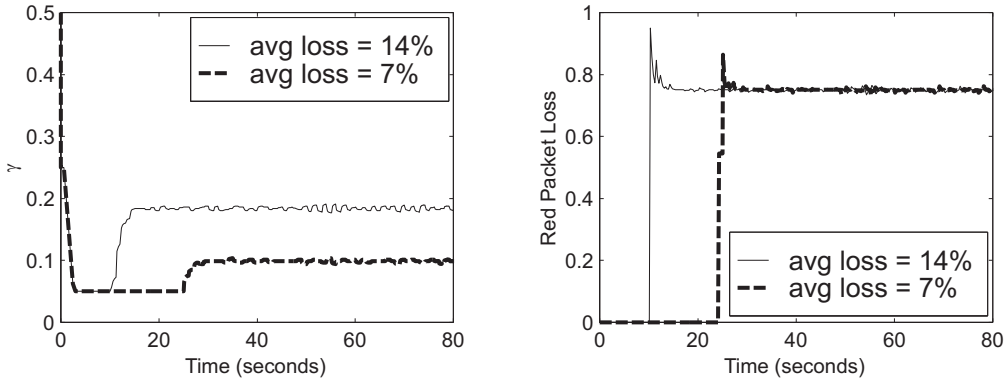

Fig. 8. The evolution of γ (left). The corresponding red loss rates (right).

from the traffic in the Internet queue. In our simulations, we allocate 50% of the bottleneck link to TCP cross-traffic; however, since the PELS and Internet queues do not affects each other in any way, we only focus on PELS flows and omit discussion of what happens to TCP traffic.

2. Stability Properties of γ

In this section, we show simulation results regarding stability of $\gamma(k)$ computed by end-flows using dynamically varying packet loss $p(k)$. Fig. 8 (left) shows the evolution of $\gamma(k)$ obtained by running PELS streaming simulations in `ns2` with two different average packet losses and $\sigma = 0.5$. In the beginning, γ drops from the initial value of 0.5 to the lowest possible threshold $\gamma_{low} = 0.05$ since there is no packet loss (i.e., the flows slowly probe for new bandwidth). When packets start being dropped during congestion, γ increases until it is stabilized at $\gamma^* = p^*/p_{thr}$. Small oscillations of $\gamma(k)$ after it reaches the stationary point is caused by small variation in feedback $p(k)$.

Fig. 8 (right) illustrates red packet drop rates p_R corresponding to the values of γ on the left side the figure. As shown in the figure, red packet loss is stabilized at the target threshold rate $p_{thr} = 75\%$ regardless of the value of p (i.e., 7% or 14%). Since

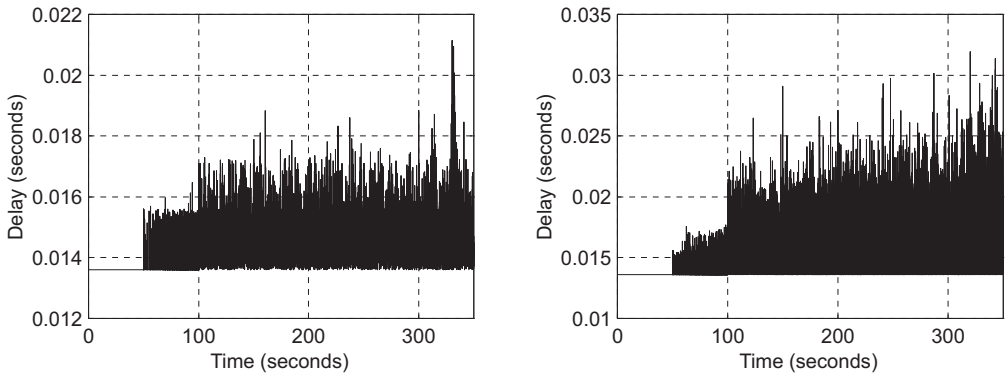

Fig. 9. Green (left) and yellow (right) delays.

the red loss never reaches 100%, all of yellow packets are protected and experience (ideal) zero-loss conditions.

Recall that AQM routers in the PELS framework employ three priority queues for preferential treatment of green, yellow, and red packets. Fig. 9 illustrates delays of green (left) and yellow (right) packets and Fig. 10 (left) depicts delays of red packets. Theses delays are obtained by running `ns2` simulations in which at every 50 seconds, two new flows entered the system with the initial rate of 128 kb/s (i.e., the rate of the base layer).

3. Delay Characteristics of PELS

First notice that green and yellow packets have very small delays compared to those of red packets. The average delays of green and yellow packets are only 16 and 25 ms, respectively, while the average delays of red packets reach as high as 400 ms. Further notice that after 100 seconds, red packet delays increase every 50 seconds since each new flow further reduces the available bandwidth and increases congestion in the red queue. These results are expected from the use of priority queuing in the routers and have no harmful effect on PELS flows as loss or delays in the red queue have

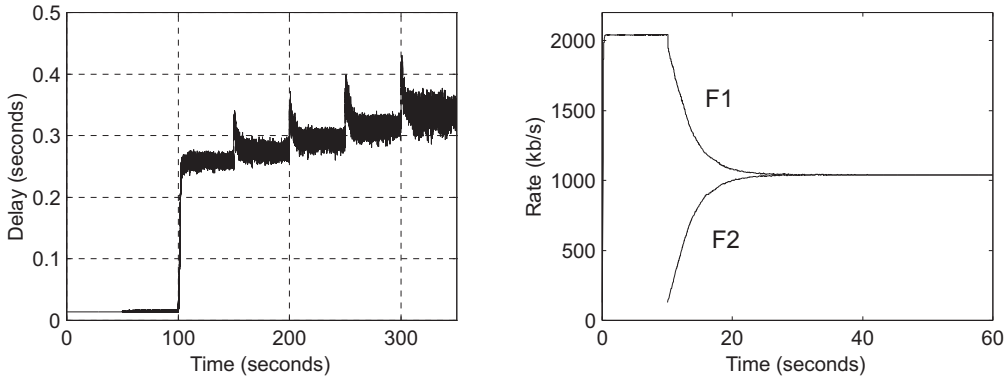

Fig. 10. Red packet delays in PELS (left). Convergence and fairness of MKC congestion control (right).

minimum impact on the video quality (in fact, the purpose of red packets *is* to be lost in the network and protect the yellow queue).

4. Properties of PELS Congestion Control

We next study characteristics of MKC congestion control coupled with the PELS queuing framework. Fig. 10 (right) illustrates convergence of two PELS flows to 50% of the available PELS capacity (i.e., 1 mb/s each) for $\alpha = 20$ kb/s and $\beta = 0.5$. In the figure, flow F1 starts at time zero with the initial rate $r_0 = 128$ kb/s and then converges to the full link capacity at around 0.1 seconds exponentially claiming the available bandwidth. It maintains the equilibrium rate until the second flow F2 starts at $t = 10$ seconds ($r_0 = 128$ kb/s). After another 13 seconds, both flows converge to a fair allocation of link's bandwidth. For additional simulations of MKC with non-equal feedback delays, see [17], [107].

5. PSNR Quality Evaluation

In this section, we compare the proposed preferential streaming scheme with the best-effort method using PSNR quality curves. Through simulation, we obtained packet

loss statistics of each FGS frame and then applied them to the video sequence offline. We enhanced each base-layer frame using consecutively received FGS packets and plotted PSNR quality curves accordingly. Aggregate packet loss was calculated in the routers at $T = 30$ ms time intervals.

Our main puzzle in this section was to properly select a "generic" brand of best-effort streaming that adequately represents existing (non-QoS) approaches. Although there are numerous methods of streaming video over the Internet (including TCP, FEC-protected transmission, and various non-AIMD methods), we aim to compare PELS with an alternative framework that: 1) does not retransmit any lost packets; and 2) does not send any error-correcting codes. Since no such framework exists to our knowledge, we use AQM-enabled MKC under the assumption that the base layer is "magically" protected at all times. If packet loss is allowed in the base layer and retransmission is suppressed, best-effort streaming simply becomes impossible due to propagation of losses throughout each GOP (Group of Pictures). Thus, we protected the entire base layer in the best-effort case and allowed random loss only in the FGS layer to keep this approach even remotely competitive with PELS.

We first examine PSNR of the Foreman sequence reconstructed with 10% network packet loss (Fig. 11(a)). As shown in the figure, best-effort streaming improves the base-layer PSNR by approximately 24% on average, while PELS enhances it by 60%.

Next, we examine the case with higher packet loss. Fig. 11(b) illustrates the PSNR curve of the same Foreman sequence reconstructed with 19% packet loss. In this case, while the best-effort method improves the base-layer PSNR only by 16%, PELS improves it by 55%.

From the curves in Fig. 11, we also observe that the PSNR of best-effort streaming varies by as much as 15 dB (even though the sending rates of MKC are perfectly smooth) and provides a highly-fluctuating quality that is similar to that achievable

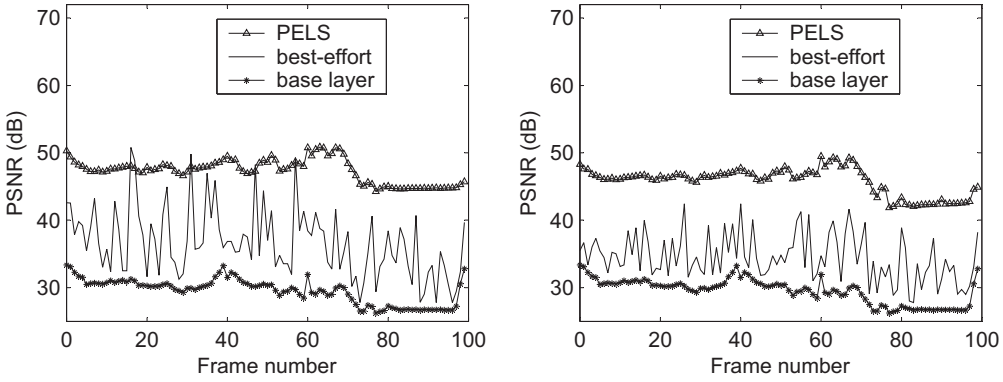

(a) $p = 10\%$ (b) $p = 19\%$

Fig. 11. PSNR of CIF Foreman reconstructed with two different packet loss p.

with AIMD [17]. On the contrary, PELS maintains a much higher PSNR throughout the entire sequence and keeps quality fluctuation to a minimum, which can be further reduced using sophisticated R-D scaling methods [17] (not used in this work). Thus, we can conclude that PELS streaming provides an effective and low-overhead QoS foundation for scalable multimedia streaming in the future Internet.

CHAPTER IV

MODELING BEST-EFFORT AND FEC STREAMING

We study Forward-Error Correction (FEC) for video streaming over best-effort networks. FEC is often used in streaming applications to protect video and audio data in lossy network paths; however, studies (such as [3], [7], [11], [31]) in the literature report conflicting results on the benefits of FEC over best-effort streaming. To address this uncertainty, we start with a baseline case that examines the impact of packet loss on scalable (FGS-like) video in best-effort networks and derive a closed-form expression for the loss penalty imposed on embedded coding schemes under several loss models. Through this analysis, we find that the utility (i.e., usefulness to the user) of unprotected video *converges to zero* as streaming rates become high. We then study FEC-protected video streaming, re-derive the same utility metric, and show that for all values of loss rate inclusion of FEC overhead substantially improves the utility of video compared to the best-effort case. We finish this chapter by constructing a dynamic controller on the amount of FEC that maximizes the utility of scalable video and show that the resulting system achieves a significantly better PSNR quality than alternative fixed-overhead methods.

A. Introduction

Forward-error correction (FEC) is widely used in the Internet for its ability to recover data segments lost in the network [7], [79], [103]. With a proper amount of redundancy included in transmitted packets, FEC can reduce the impact of packet loss on the quality of video, thus improving the performance of streaming over best-effort

networks. However, selection of FEC overhead becomes a fairly complicated task when network path dynamics change over time, which in certain cases may lead to reduced or negligible performance gain compared to similar best-effort scenarios [3], [7], [58].

Although FEC appears intuitively beneficial, studies in the literature report conflicting results on its performance in practice. Some of them (e.g., [3], [58]) show that FEC provides little benefit to applications due to the extra overhead, while others (e.g., [11], [31]) find FEC to be promising in the context of particular multimedia applications. To understand the benefits of FEC in Internet streaming, we first analyze the performance of video streaming in best-effort networks and derive a closed-form model for the penalty inflicted on scalable[1] video coding under Markov and renewal patterns of packet loss. For this analysis, we consider *end-user utility* U as the main metric, which we define as the percentage of received data in each frame that can be used for decoding the frame, i.e.,

$$U = \frac{M}{T}, \tag{28}$$

where M is the average number of bytes/packets used in decoding a frame and T is the average amount of data per frame successfully delivered to the receiver. Deriving (28) in closed-form, we show that best-effort streaming imposes a significant penalty on video applications when packet loss randomly corrupts the video stream and demonstrate that for any fixed packet loss $p > 0$, the utility $U \to 0$ as the streaming rate goes to infinity.

Given poor performance of best-effort streaming, we next examine FEC-protected

[1]In scalable video (e.g., MPEG-4 FGS [83]), the enhancement layer is compressed using embedded coding and can be easily re-scaled to match variable network bandwidth during streaming. In such methods, the lower sections of the enhancement layer are more important than the higher sections because their loss renders all dependent data in the source frame virtually useless.

transmission of video data. Previous studies in the literature (e.g., [31], [32], [105]) have examined the dynamics of the loss process under a two-state Markov chain and provided numerical models for obtaining the distribution of the number of loss events in a block of fixed size n; however, these models usually rely on complex recursive expressions or tedious summations, neither of which sheds light in *qualitative* or *closed-form* terms on the behavior of FEC in practice. To overcome this limitation and ultimately compute (28), we study the effect of Markov-based packet loss within an FEC block and derive the asymptotic (i.e., assuming large sending rates) distribution of the number of lost packets per FEC block. This model offers a low-complexity version of the same result obtained by the earlier methods and allows computation of other metrics of interest related to FEC streaming.

Armed with this result, we next focus on investigating the performance of video streaming with FEC protection under two-state Markov-chain loss. Assuming that R is the streaming rate of the application and F is the rate of FEC packets, we employ (28) to understand how the FEC overhead rate $\psi = F/(R+F), (0 < \psi < 1)$, affects the utility of received video. Using the models derived in the second part of the chapter, we show that U exhibits percolation and converges to 0, 0.5, or $(1-\psi)/(1-p)$ depending on the value of ψ as the streaming rate R approaches infinity. However, for finite R, we find that U achieves a unique global maximum in some point ψ^* that depends on network packet loss and FEC block size, which indicates *that sending more or less FEC than the optimal amount results in a reduction in* U.

Driven by the goal of maximizing the usefulness of network bandwidth and achieving the highest visual quality under given network conditions, we subsequently explore a simple control mechanism that dynamically adjusts the amount of overhead $\psi(t)$ based on the packet-loss information fed back to application servers by their receivers. We find that such adaptive control allows the application to maintain op-

timally high utility regardless of the variation in packet loss rates and deliver better PSNR quality to the user compared to schemes with a static or sub-optimal allocation of FEC.

B. Impact of Packet Loss in Best-Effort Networks

In this section, we examine the performance of video streaming in the best-effort Internet assuming random packet loss. We consider two loss models and study the expected amount of recovered data in each video frame. Unlike previous studies (e.g., [5]), we model the dependency between data in each video frame and derive the expected percentage of useful information transmitted over the bottleneck link.

Many studies (e.g., [104]) show that the pattern of Internet packet loss can be captured by Markov models. Thus, we first examine the dynamics of utility (28) assuming that the loss process is a two-state Markov chain. Following the Markov analysis, we study a more general distribution of packet loss and model the network as an alternating ON/OFF process with heavy-tailed ON (loss) and OFF (no loss) periods. While the two modeling approaches are different, they both demonstrate that the best-effort Internet imposes a significant performance penalty on scalable streaming services and its handling of video traffic is far from optimal.

1. Markov Packet Loss

We investigate the effect of packet drops on video quality using the example of MPEG-4 FGS (Fine Granular Scalability[2]) [83]. In what follows next, we apply the Markov

[2]Similar results apply to motion-compensated enhancement layers, which suffer even more degradation under best-effort loss and are not modeled in this work. However, the expected amount of improvement from FEC in such schemes is even higher than that in FGS.

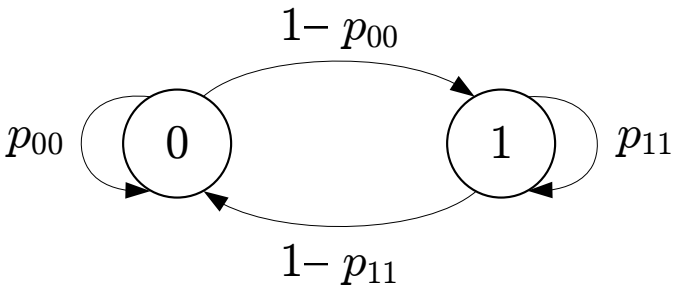

Fig. 12. Two-state Markov chain.

packet-loss model to FGS sequences, derive the expected amount of useful data recovered from each frame, and define the effectiveness of FGS packet transmission over a lossy channel. Note that in our analysis, we only examine the enhancement layer (which is often responsible for a large fraction of the total rate) and assume that the base layer is fully protected. Even under such conditions, best-effort networks deliver very low performance to scalable flows, which progressively degrades as the streaming rate becomes higher.

Assume that the long-term network packet loss is given by p and the loss process can be modeled by a two-state discrete Markov chain shown in Fig. 12, where states 1 and 0 represent a packet being either lost in the network or delivered to the receiver, respectively. In the figure, $1 - p_{00} > 0$ is the probability that the next packet is lost given that the previous one has arrived and $1 - p_{11} > 0$ is the probability that the next packet is received given that the previous one has been lost. In the stationary state, probability π_0 and π_1 to find the process in each of its two states are given by:

$$\pi_0 = \frac{1 - p_{11}}{2 - p_{00} - p_{11}}, \quad \pi_1 = p = \frac{1 - p_{00}}{2 - p_{00} - p_{11}}. \tag{29}$$

Assume that FGS frame sizes H_j are measured in packets and are given by *i.i.d.* random variables. The exact distribution of $\{H_j\}$ is not essential and typically depends on the coding scheme, frame rate, variation in scene complexity, and the

bitrate of the sequence. The question we address next is *what is the expected amount of useful packets that the receiver can decode from each frame under p-percent random loss?* To answer this question, we denote by Z_j the number of consecutively received packets in a frame j and next compute its expectation $E[Z_j]$, which plays an important role in determining the utility of received video.

Assume that the chain is stationary at the beginning of a frame and let $E[Z_j^H]$ be the expected number of useful packets per frame if all frames are of size H. Then, we have the following result.

Theorem 1. *Assuming a two-state Markov packet loss in (29) and fixed-size frames with $H_j = H$, the expected number of useful packets in each frame is:*

$$E[Z_j^H] = \frac{1-p}{1-p_{00}}(1-p_{00}^H). \tag{30}$$

Proof. Assume that D_j is the random distance in packets from the beginning of frame j before the first packet-loss event. Let X_1 be the state of the Markov chain when the first packet in frame j passes through the network. Note that if $X_1 = 1$, then the amount of recovered data in the frame is $Z_j = 0$; however, if the loss process is in state $X_1 = 0$, then the recovered amount depends on the value of D_j, i.e., the decoder recovers $Z_j = D_j$ packets when $D_j \leq H$ and all $Z_j = H$ packets otherwise. Then, we can write:

$$\begin{aligned} E[Z_j^H] &= \pi_0 E[Z_j^H | X_1 = 0] + \pi_1 E[Z_j^H | X_1 = 1] \\ &= \pi_0 \Big(\sum_{i=1}^{H} i P(D_j = i | X_1 = 0) + H \sum_{i=H+1}^{\infty} P(D_j = i | X_1 = 0) \Big) \end{aligned} \tag{31}$$

Conditioning on $X_1 = 0$, it immediately follows that D_j are geometric random variables with a conditional PMF $P(D_j = i | X_1 = 0) = p_{00}^{i-1}(1-p_{00}), i \geq 1$. Substituting $\pi_0 = 1 - \pi_1 = 1 - p$ in (31) and expanding the PMF of D_j, we get (30). □

Table II. Expected Number of Useful Packets (Markov Model)

Packet loss	$H = 100$		$H = 1,000$	
p	Simulations	Model (30)	Simulations	Model (30)
0.0001	99.595	99.595	960.988	960.986
0.01	68.329	68.324	123.715	123.709
0.1	11.248	11.247	11.255	11.250
0.2	4.998	5.000	4.999	5.000
0.9	0.138	0.138	0.139	0.138

To verify (30), we simulate a Markov loss process in Matlab with several values of packet loss p and keep probability p_{00} equal to $1 - 0.8p$ and p_{11} equal to $(2p - 1 + p_{00}(1 - p))/p$ so that the average loss rate is p. For this example, we generate a sequence of 10 million frames of size H each and randomly corrupt them using a long Markov-chain loss sequence. Then, we examine each frame j to obtain Z_j and compare $E[Z_j^H]$ to the model in Table II for $H = 100$ and $H = 1,000$. As the table shows, (30) matches simulations very well. Also observe in the table that for $H = 100$ and a reasonably low packet loss of 1%, the expected number of useful packets in each frame is only 68 even though the decoder successfully receives (on average) 99 packets per frame. When we use larger frames with $H = 1,000$, the decoder can use only 123 packets on average out of each 990 packets it receives over the network. Moreover, the table shows that under $p = 10\%$, only 11 useful packets are recovered from each frame *regardless of the actual size of the frame*. This means that the bottleneck link under these conditions transmits 8 ($H = 100$) to 90 ($H = 1,000$) times more packets than the receiver is able to utilize in decoding its video.

It is easy to notice in (30) that $E[Z_j^H]$ saturates at $(1 - p)/(1 - p_{00})$ as $H \to \infty$ (i.e., streaming rates become high). This is shown in Fig. 13(a) for $p = 0.1$ ($p_{00} = 0.92$ and $p_{11} = (2p - 1 + p_{00}(1 - p))/p = 0.28$), in which the number of useful packets

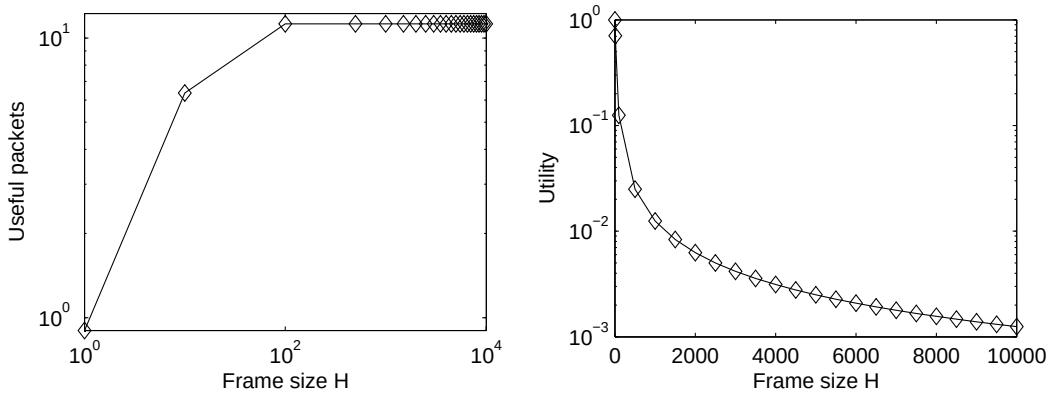

(a) $E[Z_j^H]$ (b) U^H

Fig. 13. Simulation results of $E[Z_j^H]$ and U^H for $p = 0.1$.

recovered per frame indeed converges to $(1-p)/(1-p_{00}) = 11$ as H becomes large.

Re-writing (28) using (30), we have for constant frame sizes:

$$U^H = \frac{E[Z_j^H]}{H(1-p)} = \frac{1-p_{00}^H}{(1-p_{00})H}. \tag{32}$$

For instance, we get $U^H = 0.12$ for $p = 0.1$ (using the same value of p_{00}, p_{11} as before) and $H = 100$, which means that only 12% of the received FGS packets are useful in enhancing the base layer. The trend of (32) is illustrated in Fig. 13(b), which plots the utility of best-effort streaming for different values of H and $p = 0.1$. As the figure shows, U^H drops to zero inverse proportionally to the value of H, which means that as $H \to \infty$, the decoder receives "junk" data with probability $1 - o(1)$.

Next, we briefly study the result of Theorem 1 for arbitrary frame-size distributions. For this purpose, we expand (30) to variable frame sizes H_j.

Corollary 2. *Assuming a two-state Markov packet loss in* (29)*, the expected number*

of useful packets in each frame is:

$$E[Z_j] = \frac{1-p}{1-p_{00}}\Big(1 - E[p_{00}^{H_j}]\Big). \tag{33}$$

In the next theorem, we show that $E[Z_j]$ in *any* video sequence with the average frame size H is upper-bounded by (30).

Theorem 3. *For a given average frame size $E[H_j] = H$ and Markov-chain loss, the expected number of useful packets per frame is always upper-bounded by that in sequences with $H_j = H$:*

$$E[Z_j] \leq E[Z_j^H]. \tag{34}$$

Proof. Set $u(x) = p_{00}^x$ and notice that $u(x)$ is a strictly convex function of x. Then, using Jensen's inequality, it follows that $E[u(H_j)]$ is no less than $u(E[H_j])$ and therefore $1 - E[p_{00}^{H_j}] \leq 1 - p_{00}^H$. Applying this observation to (30) and (33), we immediately obtain (34). □

We illustrate the result of Theorem 3 assuming a lognormal[3] frame-size distribution, whose PDF is given by:

$$f(x) = \frac{1}{\sqrt{2\pi}\sigma x} e^{-(\log x - \mu)^2/2\sigma^2}, \tag{35}$$

where μ and σ^2 are respectively the mean and variance of $\log(H_j)$. For the sake of this example, we use $p = 0.1$, $p_{00} = 1 - p$, $\sigma = 1.5$ and compute μ such that the mean of the lognormal distribution $E[H_j] = e^{\mu + \sigma^2/2}$ matches the desired values. Table III shows the expected number of useful packets in each frame of this sequence and the same metric in the case of constant frame sizes $H_j = H$. As the table shows, $E[Z_j]$ matches simulations well and is in fact upper-bounded by $E[Z_j^H]$.

[3]Several studies have shown that MPEG frame sizes can be modeled by a lognormal distribution [87], which explains our interest in it.

Table III. Expected Number of Useful Packets (Variable Frame Size)

$E[H_j]$	Simulations	Model (33)	Upper bound (30)
10	3.427	3.450	5.861
100	7.446	7.406	8.999
200	8.143	8.148	9.000
500	8.651	8.696	9.000

Similar observations apply to utility U, which we define as:

$$U = \frac{E[Z_j]}{(1-p)E[H_j]} = \frac{1 - E[p_{00}^{H_j}]}{(1-p_{00})E[H_j]}. \tag{36}$$

From Theorem 3, it immediately follows that U is upper-bounded by U^H:

$$U \leq U^H = \frac{1 - p_{00}^H}{(1-p_{00})H}. \tag{37}$$

This result indicates that regardless of the frame-size distribution, Markov loss implies that $U \to 0$ as $H \to \infty$ and the convergence rate is no worse than linear.

The next question we address is *how many useful packets can be recovered in each frame if the pattern of network packet loss deviates from the Markov model?* We penetrate this problem by obtaining $E[Z_j^H]$ under a more general packet-loss pattern. Note that since the exact distribution of H_j is application-specific (i.e., unknown) and to conserve space, the rest of the chapter only deals with constant frame sizes and no longer considers variable H_j.

2. Renewal Packet Loss

Several studies have analyzed the characteristics of Internet packet loss and reached a number of conclusions on the distribution of loss-burst lengths including that loss-burst lengths could be modeled as exponential (e.g., [104]) as well as heavy-tailed (e.g., [64]). We overcome this uncertainty by deriving closed-form models for both

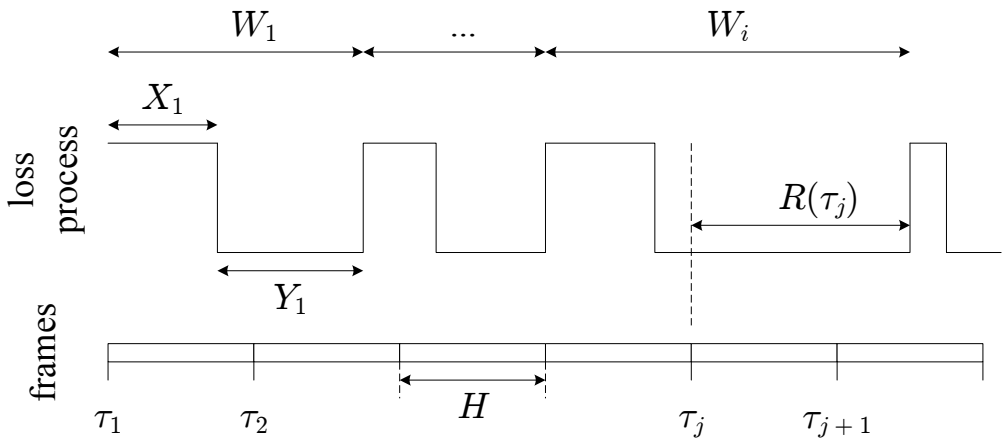

Fig. 14. ON/OFF process $V(t)$ (top) and the transmission pattern of video frames (bottom).

cases, as well as the more generic case when loss-burst lengths have an arbitrary distribution.

We explore the recurrent behavior of packet loss using a simple stochastic model from renewal theory. Assume that the packet loss process $V(t)$ goes through ON/OFF periods, where all packets are lost during each ON period and all packets are delivered during each OFF period. Then, we can write:

$$V(t) = \begin{cases} 1 & \text{loss at time } t \\ 0 & \text{no loss at time } t \end{cases} . \tag{38}$$

Suppose that the duration of the i-th ON period is given by a random variable X_i and the duration of the i-th OFF period is given by Y_i (X_i and Y_i may be drawn from different distributions). Fig. 14 illustrates the evolution of alternating process $V(t)$. The figure also shows that if $V(t)$ is sampled at a random instant τ_j where frame j starts and the process happens to be in the OFF state, the distance to the next packet loss is given by some residual process $R(\tau_j)$, whose distribution determines Z_j. We elaborate on this observation next.

Assume that X_i and Y_i are independent of each other and sets $\{X_i\}$ and $\{Y_i\}$ consist of *i.i.d.* random variables. Then, $V(t)$ is an alternating renewal process, whose j-th renewal cycle has duration $W_j = X_j + Y_j$ and whose n-th renewal occurs at time epoch $T_n = \sum_{j=1}^{n} W_j$. Next, we derive long-term network packet loss p, which is the fraction of time that the process is in the ON state.

Lemma 7. *Under the ON/OFF process model, the long-term network packet loss p is:*

$$p = \lim_{t\to\infty} P(V(t) = 1) = \frac{E[X_i]}{E[X_i] + E[Y_i]}. \tag{39}$$

Proof. Notice that network packet loss is the ratio of the total number of lost packets to the total number of transmitted packets, averaged over a sufficiently long period of time. This can be written as:

$$p = \lim_{t\to\infty} \frac{1}{t} \int_0^t V(u)du. \tag{40}$$

We can view each ON duration of $V(t)$ as the amount of *reward* $P_j = X_j$ for each renewal cycle W_j. Then, the cumulative reward $C(t)$ of this process over each interval $[0, t)$ is $C(t) = \int_0^t V(u)du$. Applying the renewal-reward theorem to $C(t)$, we have [102]:

$$p = \lim_{t\to\infty} \frac{C(t)}{t} = \frac{E[P_j]}{E[W_j]}. \tag{41}$$

Substituting $E[P_j]$ and $E[W_j]$ in (41), we get (39). □

Given network packet loss p, we are primarily interested in the location of the first ON event after each frame starts, which determines the number of consecutively received packets in that frame. Suppose that τ_j represents the time instants when the j-th frame starts its transmission over the network. Then, we can safely assume that points τ_j are *uncorrelated* with the cycles of packet loss $V(t)$ since the former

is an application-specific parameter, while the latter depends on many factors (such as network congestion and cross-traffic) that are not related to the *contents* of the streaming traffic. Thus, we can view τ_j as being uniformly distributed within each renewal cycle of $V(t)$ and $R(\tau_j)$ as the *residual* life of Y_i before the next renewal.

Notice that at τ_j, there are two possible scenarios:

- $V(t)$ is in the ON state;
- $V(t)$ is in the OFF state.

In the former case, the amount of useful data recovered in the frame is $Z_j^H = 0$. However, in the latter case, this amount will depend on the residual life $R(\tau_j)$ of the current OFF cycle (see Fig. 14). Denote by $F_Y(x)$ the distribution of Y_i and assume that $E[Y_i] < \infty$. Next, define $F(x) = P(R(t) \leq x)$ to be the distribution of the residual lifetime of the current OFF cycle. Then, recall that $F(x)$ can be expressed as [102]:

$$F(x) = \frac{1}{E[Y_i]} \int_0^x (1 - F_Y(u))\, du. \tag{42}$$

Noticing that the distribution of X_i does not affect $E[Z_j^H]$, we have the following result.

Theorem 4. *Assuming a fixed frame size H, the expected number of useful packets in a frame is determined solely by the distribution of inter-loss durations Y_i and equals:*

$$E[Z_j^H] = (1 - p) \int_0^H \bar{F}(x) dx, \tag{43}$$

where $\bar{F}(x) = 1 - F(x)$ is the tail distribution of $R(t)$.

Proof. Consider a frame j that starts at time instant τ_j. Conditioning on $V(t)$ being in the OFF state at τ_j, the number of recovered bits/bytes is the random variable

$Z_j^H = \min(R(\tau_j), H)$, which leads to the following:

$$E[Z_j^H] = (1-p)\left(\int_0^H xf(x)dx + H\int_H^\infty f(x)dx\right), \tag{44}$$

where term $1-p$ is simply $P(V(t)=0)$ and $f(x)$ is the PDF of $R(t)$. Using integration by parts, the first integral in (44) becomes:

$$\int_0^H xf(x)dx = HF(H) - \int_0^H F(x)dx. \tag{45}$$

The second integral in (44) is:

$$H\int_H^\infty f(x)dx = H - HF(H). \tag{46}$$

Adding (45) and (46) and rearranging the terms, we establish (43). □

Note that (42) is based upon the limiting distributions of conventional renewal theory, which provides an *asymptotic* result on $R(t)$ as $t \to \infty$. In order to examine the accuracy of the model for finite $t \ll \infty$, we obtain closed-form expressions of (43) for exponential and Pareto distributions of Y_i in the next two lemmas and compare these results to simulations.

Lemma 8. *For exponential Y_i with rate λ, the expected number of useful packets in a frame is:*

$$E[Z_j^H] = \frac{1-p}{\lambda}\left(1 - e^{-\lambda H}\right). \tag{47}$$

Proof. Since $F_Y(x)$ is an exponential distribution, from (42) or the memoryless property of exponential distributions, $F(x) = 1 - e^{-\lambda x}$. Substituting $\bar{F}(x) = 1 - F(x) = e^{-\lambda x}$ in (43), we get (47). □

We illustrate the usage of (47) using exponential Y_i with several values of packet

Table IV. Expected Number of Useful Packets (Exponential Model)

Packet loss	$H = 100$		$H = 1,000$	
p	Simulations	Model (47)	Simulations	Model (47)
0.0001	99.491	99.491	951.599	951.530
0.01	62.582	62.579	98.970	98.995
0.1	8.998	8.999	8.978	9.000
0.2	3.987	4.000	3.979	4.000
0.9	0.111	0.111	0.110	0.111

loss p. We set $E[X_i] = 1/(1-p)$, $E[Y_i] = 1/p$ (which leads to $\lambda = p$), and generate over 20 million random values X_i, Y_i to simulate the evolution of ON/OFF process $V(t)$ and obtain metric $E[Z_j^H]$ for a video stream of fixed-size frames. Model (47) is compared to simulation results for $H = 100$ and $H = 1,000$ in Table IV. As shown in the table, (47) follows simulation results very well and also saturates at fixed values as $H \to \infty$. This result clearly implies that U^H converges toward zero for large H.

The next result shows that heavy-tailed inter-burst gaps Y_i actually improve $E[Z_j^H]$. In this case, we consider a shifted Pareto distribution $F_Y(x) = 1-(x/\beta+1)^{-\alpha}$, where $x \geq 0$, $\alpha > 1$, and $\beta > 0$. Notice that the domain of this distribution is $(0, \infty)$, which allows us to construct a well-formed renewal process and model arbitrarily small durations Y_i.

Lemma 9. *For Pareto Y_i with finite mean $E[Y_i] < \infty$, the expected number of useful packets is:*

$$E[Z_j^H] = \begin{cases} \dfrac{(1-p)\beta}{2-\alpha}\left[\left(\dfrac{H}{\beta}+1\right)^{2-\alpha} - 1\right] & \alpha \neq 2 \\ (1-p)\beta \log\left(\dfrac{H}{\beta}+1\right) & \alpha = 2 \end{cases}. \tag{48}$$

Proof. Using $E[Y_i] = \beta/(\alpha - 1)$, we have the following distribution of $R(t)$:

$$F(x) = \frac{1}{E[Y_i]} \int_0^x \left(\frac{u}{\beta} + 1\right)^{-\alpha} du = 1 - \left(\frac{x}{\beta} + 1\right)^{1-\alpha}. \tag{49}$$

Notice that this is a more heavy-tailed distribution than the original one, which implies that residuals $R(\tau_j)$ are expected to be *larger* than the original OFF periods Y_i[4]. Substituting $\bar{F}(x) = (x/\beta + 1)^{1-\alpha}$ into (43), we have:

$$E[Z_j^H] = (1-p) \int_0^H \left(\frac{x}{\beta} + 1\right)^{1-\alpha} dx. \tag{50}$$

Separately expanding the integral in (50) for $\alpha = 2$ and $\alpha \neq 2$, we get both cases in (48). □

We also verify (48) using simulations with Pareto-distributed Y_i and keep $E[X_i] = 1/(1-p)$, which leads to β being equal to $(\alpha - 1)/p$. We compare simulation results with (48) in Table V for $H = 100$ and $H = 1,000$. First, notice in the table that simulations match the model very well. Second, observe that the Pareto case delivers more useful packets on average than the exponential case previously shown in Table IV. This can be explained by the properties of Pareto $F_Y(x)$, which tends to create large inter-loss gaps followed by many small ones all hitting the same frame. This is schematically shown in Fig. 15 where the Pareto loss events are more bursty and each frame has a higher probability to start within a very large OFF burst.

Also notice that for $\alpha > 2$, $E[Z_j^H]$ in (48) converges to a constant equal to $(1-p)\beta/(\alpha-2)$ as $H \to \infty$ and utility U^H asymptotically tends to zero as $1/H$. For $\alpha = 2$, the expected number of recovered packets is approximately $(1-p)\beta \log H$, which grows (albeit slowly) to infinity as $H \to \infty$. Nevertheless, even in this case,

[4]This is the so-called "inspection paradox" [102].

Table V. Expected Number of Useful Packets (Pareto Model)

Packet loss	$\alpha = 2$, $H = 100$		$\alpha = 3$, $H = 100$	
p	Simulations	Model (48)	Simulations	Model (48)
0.0001	99.492	99.493	99.491	99.492
0.01	68.613	68.621	66.017	66.000
0.1	21.557	21.581	15.012	15.000
0.2	12.062	12.178	7.263	7.272
0.9	0.494	0.501	0.218	0.217
Packet loss	$\alpha = 2$, $H = 1,000$		$\alpha = 3$, $H = 1,000$	
p	Simulations	Model (48)	Simulations	Model (48)
0.0001	952.713	953.006	952.256	952.285
0.01	237.278	237.391	164.950	165.000
0.1	41.652	41.536	17.630	17.647
0.2	21.296	21.213	7.894	7.920
0.9	0.754	0.755	0.225	0.221

$U^H \sim \log(H)/H \to 0$ for sufficiently large frame sizes. Finally, for very heavy-tailed cases of $1 < \alpha < 2$, $E[Z_j^H]$ is proportional to $H^{2-\alpha}$ and utility $U^H \sim H^{1-\alpha}$ still becomes asymptotically negligible as $H \to \infty$.

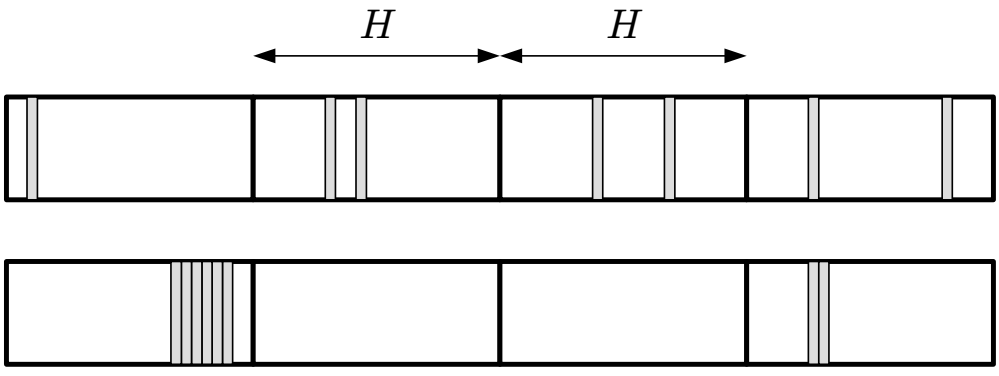

Fig. 15. Packet loss patterns for exponential (top) and Pareto (bottom) Y_i.

3. Discussion

Note that for many Internet applications and protocols (such as TCP), it is typically understood that uniform packet loss has benefits over bursty loss. Interestingly, however, our results imply that for streaming of embedded video signals, bursty packet drops are more desirable than uniformly random. It is further important to note that video-coding methods that use error concealment may exhibit lower performance under bursty loss, in which case the above conclusions would not necessarily hold. In all other cases, subsequent losses within a given frame have no effect on the already-useless frame data and thus lead to better performance of the application as they allow a larger portion of the *remaining* frames to be loss-free.

We next investigate FEC-based streaming as an alternative to retransmission. We study the characteristics of packet drops in an FEC-block in the following section and discuss the impact of loss on FEC-protected video in Section D.

C. Impact of Packet Loss on FEC

The distribution of the number of lost packets and the location of the first loss in a block play an important role in understanding the effectiveness of FEC. This section studies these two metrics and offers a model for each assuming large sending rates.

We start by briefly discussing previous work on Markov loss models and pointing out their shortcomings.

1. Background

The original work by Gilbert [32] examines loss events in communication channels under a two-state Markov chain and provides an error model based on recursive formulas that compute the probability of losing a certain number of packets in a

block of a given size. Assume a Markov-chain loss model in Fig. 12 and define $P(u, x)$ to be the probability of losing x packets out of u transmitted ones. Next, notice that by conditioning on the last state of the Markov loss process, probability $P(u, x)$ can be written as following:

$$P(u, x) = P(u, x|0) + P(u, x|1), \tag{51}$$

where $P(u, x|j)$, $j = 0$ or 1, represents the probability of losing x packets out of u transmitted packets given that the loss process is in state j at the end of the block.

Further note that $P(u, x|0)$ and $P(u, x|1)$ can be written as recursive equations [105]:

$$\begin{aligned} P(u, x|0) &= P(u-1, x|0)p_{00} + P(u-1, x|1)(1-p_{11}) \\ P(u, x|1) &= P(u-1, x-1|1)p_{11} + P(u-1, x-1|0)(1-p_{00}), \end{aligned}$$

where p_{00} and p_{11} represent transition probabilities of the Markov chain shown in Fig.12.

As two-state Markov loss models have become fairly standard, additional studies (e.g., [31]) examine methods of deriving the above probabilities in closed-form. These approaches and the resulting models are generally very complex both numerically and symbolically. In one example, Yousefizadeh *et al.* [105] recently presented a closed-form solution to the recursive equations above. They derive the probability of receiving $v = u - x$ packets from a u-packet FEC block:

$$P(u, x|j) = p_{00}^{u-2x+j}(1-p_{00})(1-p_{11})^{1-j}W_1P_0 + p_{00}^{u-2x-1+j}(1-p_{00})^j(1-p_{11})W_2P_1,$$

where

$$W_1 = \sum_{i=0}^{x-1} \binom{x-1}{i} \binom{v}{i+1-j} (p_{00}p_{11})^{x-1-i} \Big((1-p_{00})(1-p_{11})\Big)^i,$$

$$W_2 = \sum_{i=0}^{x-j} \binom{x}{i+j} \binom{v-1}{i} (p_{00}p_{11})^{x-i-j} \Big((1-p_{00})(1-p_{11})\Big)^i.$$

Note that this model holds only for particular conditions (such as $u \geq 2x+1$) and is computationally intensive for non-trivial u even though it does not require solving recursive equations. Also note that none of the previous models provides explicit information about the distribution of the number of lost packets per block or the location of the first loss event.

In the following subsections, we examine a new (asymptotic) methodology that computes the probability $P(u,x)$ and related metrics of interest in simple closed-form terms.

2. Basic Model

To investigate how the Markov loss process affects each block of FEC, we define $L(n)$ to be the random number of packets lost in a given block of size $n \geq 1$. Notice that $P(u,x)$ discussed in the previous subsection is simply $P(L(u) = x)$. Next, define Bernoulli random variables:

$$X_i = \begin{cases} 1 & \text{packet } i \text{ is lost} \\ 0 & \text{otherwise} \end{cases}, \quad 1 \leq i \leq n. \tag{52}$$

where i is the sequence number of the packet within a given block of size n.

Then, the number of lost packets in the block is $L(n) = \sum_{i=1}^{n} X_i$. Note, however, that since loss events X_i in the block are correlated under Markov loss, the distribution of $L(n)$ as $n \to \infty$ does not follow the de Moivre-Laplace theorem for

independent random variables. Instead, $L(n)$ converges to a Gaussian distribution $N(nE[X_i], Var[\sum X_i])$ as long as $\{X_i\}$ are bounded and exhibit exponentially decaying dependence[5] [94]. In such cases, the approximation error is available explicitly and is of the order of $(\log n)^2/\sqrt{n}$. With this result in mind, normality of $L(n)$ is easy to establish and the only remaining pieces of the model are $\mu = E[L(n)]$ and $\sigma^2 = Var[L(n)]$, which we derive next.

3. Model Parameters

Assuming that the Markov chain is in the stationary state at the beginning of the current block, we easily get:

$$\mu = E[L(n)] = E\Big[\sum_{i=1}^{n} X_i\Big] = np, \tag{53}$$

which is the same result as in the de Moivre-Laplace theorem for sums of independent variables [74]. Notice, however, that the variance of $L(n)$ does not necessarily equal the usual npq, where $q = 1 - p$. To understand the next result, define B to be the transition matrix of the two-state Markov chain in (29):

$$B = \begin{bmatrix} p_{00} & 1 - p_{00} \\ 1 - p_{11} & p_{11} \end{bmatrix}. \tag{54}$$

Furthermore, denote by λ_1 and λ_2 the eigenvalues of the transition matrix B and define a row vector $\mathbf{v} = (0, 1)$. Note that since for all stochastic matrices $\lambda_1 = 1$, it is easy to obtain that $\lambda_2 = p_{00} + p_{11} - 1$. Then, we have the following lemma.

---

[5] In the context of Markov chains, this means that the chain changes its state with non-zero probability (i.e., $p_{00} \geq \varepsilon$, $p_{11} \geq \varepsilon$ for some $\varepsilon > 0$) (see Theorem 8.9 in [8]).

Lemma 10. *Assume that each loss event in a block of size n follows the two-state Markov chain in* (29) *and the chain is in the stationary state at time* 0*. Then, the variance of* $L(n)$ *is:*

$$\sigma^2 = np(1-p) + \frac{2p(1-p)\lambda_2}{1-\lambda_2}\left(n - \frac{1-\lambda_2^n}{1-\lambda_2}\right). \tag{55}$$

Proof. Writing $\sigma^2 = E[L^2(n)] - \mu^2$, we obtain:

$$\begin{aligned} E[L^2(n)] &= E\Big[\Big(\sum_{i=1}^{n} X_i\Big)^2\Big] = nE[X_i^2] + E\Big[\sum_{i=1}^{n}\sum_{j\neq i} X_i X_j\Big] \\ &= np + 2\sum_{i=1}^{n-1}\sum_{j=i+1}^{n} E[X_i X_j]. \end{aligned} \tag{56}$$

Computing $E[X_i X_j]$ in (56), we get:

$$E[X_i X_j] = P(X_j = 1 | X_i = 1) P(X_i = 1) = \pi_1 \mathbf{v} B^{j-i} \mathbf{v}^T. \tag{57}$$

Note that the above expression $\mathbf{v}B^{j-i}\mathbf{v}^T$ is simply cell $(1,1)$ of matrix B^{j-i}. Combining (56) and (57), we get:

$$E[L^2(n)] = np + 2p\mathbf{v}\Big[\sum_{i=1}^{n-1}\sum_{d=1}^{n-i} B^d\Big]\mathbf{v}^T. \tag{58}$$

Next we compute B^d, which can be represented as a function of B's eigenvalues by Sylvester's theorem [86]. For 2×2 matrices, this leads to a simple closed-form result:

$$B^d = \lambda_1^d \frac{\lambda_2 I - B}{\lambda_2 - \lambda_1} + \lambda_2^d \frac{\lambda_1 I - B}{\lambda_1 - \lambda_2}, \tag{59}$$

where I represents the 2×2 identity matrix.

Finally, substituting (59) into (58) and recalling that we only need cell $(1,1)$ in

B^d, we get:

$$E[L^2(n)] = np + 2p\sum_{i=1}^{n-1}\sum_{d=1}^{n-i}[p + (1-p)\lambda_2^d] = np + 2p\Big[p\frac{n(n-1)}{2} + R(n)\Big], \qquad (60)$$

where

$$R(n) = \frac{(1-p)\lambda_2}{1-\lambda_2}\left(n - \frac{1-\lambda_2^n}{1-\lambda_2}\right). \qquad (61)$$

Combining (53), (60), and (61), we get (55). □

Simulations confirm that (55) is exact (for examples, see the table on page 75).

4. Asymptotic Approximation

In this subsection, we examine asymptotic (i.e., for large[6] n) characteristics of the distribution of $L(n)$. Note that unless $2 - p_{00} - p_{11} = 1 - \lambda_2$ is on the order of $1/n$, the term λ_2^n in (55) is virtually zero for non-trivial $n \gg 1$. Since p is fixed and B cannot depend on n, we can drop λ_2^n in (61) to obtain:

$$R(n) \approx \frac{(1-p)\lambda_2}{1-\lambda_2}\left(n - \frac{1}{1-\lambda_2}\right). \qquad (62)$$

This leads to the following approximation on $\sigma^2 = np(1-p) + 2pR(n)$ for large n:

$$\sigma^2 \approx np(1-p) + \frac{2p(1-p)\lambda_2}{1-\lambda_2}\left(n - \frac{1}{1-\lambda_2}\right). \qquad (63)$$

Notice that when $R(n)/n \approx 0$, the model above simplifies to the case of Bernoulli loss and σ^2 reduces to $npq(1 + o(1))$. Thus, term $R(n)$ determines the amount of "dependency" in the sequence and the amount of deviation of σ^2 from its uncorrelated version. For convenience, re-write (63) as:

$$\sigma^2 = np(1-p)\left(1 + \frac{2\lambda_2}{1-\lambda_2}\Big[1 - \frac{1}{(1-\lambda_2)n}\Big]\right). \qquad (64)$$

[6]Throughout the chapter, "asymptotically large n" means that $np \gg 0$.

As a result of this transformation, it is easy to observe as a self-check that $\sigma^2 \approx npq$ when $\lambda_2 \approx 0$ (or $p_{00} + p_{11} \approx 1$), or in other words, when there is no dependency between X_i and X_j. This indeed reduces the Markov-chain to the Bernoulli case and allows the de Moivre-Laplace theorem to hold.

For large np, we can state that for $2 - p_{00} - p_{11} \geq \varepsilon > 0$:

$$\lim_{n\to\infty} \frac{\sigma^2}{n} = p(1-p)\left(1 + \frac{2\lambda_2}{1-\lambda_2}\right). \tag{65}$$

Combining the above discussion into a single approximation, we obtain the following distribution of $L(n)$.

Corollary 5. *Assume that each loss event in a block of size n follows the two-state Markov chain in* (29)*, the chain is in the stationary state at time* 0*, and* $2-p_{00}-p_{11} \geq \varepsilon > 0$*. Then, the distribution of* $L(n)$ *for large n is:*

$$L(n) \sim N\left(np, np(1-p)\frac{p_{00}+p_{11}}{2-p_{00}-p_{11}}\right). \tag{66}$$

Next, we verify model (66) using Matlab simulations. We create a Markov process using two different values of p with two sets of transition probabilities (p_{00}, p_{11}). We use $p_{00} = 0.4$, $p_{11} = 0.1$ to obtain large packet loss $p = 0.4$ and $p_{00} = 0.92$, $p_{11} = 0.28$ for smaller packet loss $p = 0.1$. Simulation results are compared to the model in Fig. 16, where the curve "Gaussian model" is the standard distribution $N(np, npq)$ for independent loss events and curve "our model" represents the distribution predicted by (66). As the figure shows, model (66) matches the simulation very well, while the classical Gaussian model exhibits variance inconsistent with that of the actual distribution. Also notice in the figure that the true distribution of $L(n)$ may have σ^2 both smaller and larger than the corresponding value npq. The first example has $p_{00} + p_{11} = 0.5$, which results in $\sigma^2 \approx npq/3$. The second example has $p_{00} + p_{11} = 1.2$,

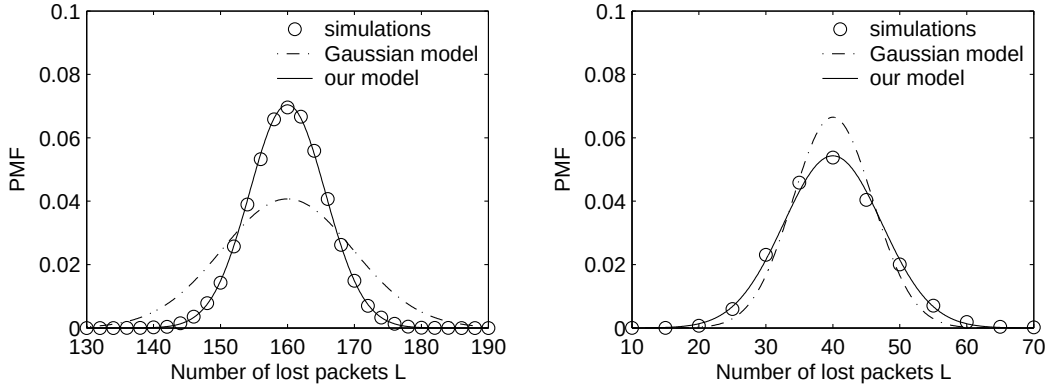

(a) $p = 0.4$ (b) $p = 0.1$

Fig. 16. Distribution of $L(n)$ for $n = 400$ and two different p.

which leads to $\sigma^2 = 1.5npq$. Further note that (66) holds for relatively small n as well. Fig. 17 shows two examples for $n = 50$ and $n = 20$, respectively, where the match is just as good as in Fig. 16.

Numerical assessment of the model is shown in Table VI, which illustrates several examples from the CDF tail of both distributions in Fig. 17. As the table shows, for both values of n, (66) matches simulations very well.

5. Non-Stationary Initial State

We now tackle the issue of non-stationary initial distribution of X_0, which is the state of the packet preceding the first packet in the FEC block. This analysis will be required later for the derivation of streaming utility U^H. Define $L_c(n)$ to be the random number of packets lost in a given block of size n conditioned on the initial state X_0 being 1 and μ_c to be its mean:

$$\mu_c = E[L_c(n)] = E[L(n)|X_0 = 1]. \tag{67}$$

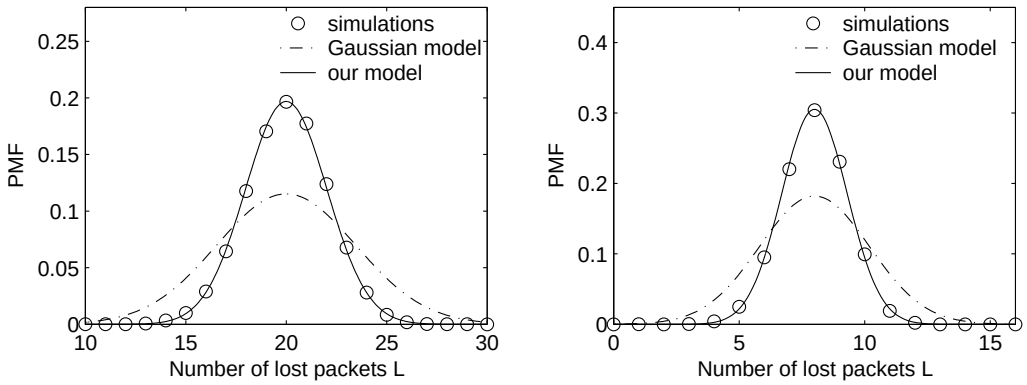

(a) $n = 50$ (b) $n = 20$

Fig. 17. Distribution of $L(n)$ for $p = 0.4$ ($p_{00} = 0.4$, $p_{11} = 0.1$).

Lemma 11. *Assume that each loss event in a block of length n follows the two-state Markov chain in* (29)*. Then, the mean of* $L_c(n)$ *for large n is:*

$$\mu_c = np + (1-p)\lambda_2 \frac{1-\lambda_2^n}{1-\lambda_2}. \tag{68}$$

Proof. Note that the mean of $L(n)$ conditioned on the value of initial state $X_0 = x$ is:

$$E[L(n)|X_0 = x] = \sum_{i=1}^{n} P(X_i = 1|X_0 = x). \tag{69}$$

To obtain $P(X_i = 1|X_0 = x)$, we need cell $(x, 1)$ from the matrix B^i. From (59), we easily establish that:

$$P(X_i = 1|X_0 = x) = \begin{cases} \pi_1(1-\lambda_2^i) & x = 0 \\ \pi_1 + (1-\pi_1)\lambda_2^i & x = 1 \end{cases}. \tag{70}$$

Setting $x = 1$ and expanding (69) using (70), we get (68). □

Simulations confirm that (68) is exact. For large n, the term λ_2^n becomes negli-

Table VI. Comparison of (66) to Simulations ($p = 0.4$)

n	Metric	Simulations	Model (66)	Gaussian model
50	μ	20.000	20.000	20.000
	σ^2	4.106	4.106	12.000
	$P(L(n) \leq 16)$	0.043	0.042	0.156
	$P(L(n) \leq 24)$	0.989	0.986	0.903
20	μ	8.000	8.000	8.000
	σ^2	1.706	1.706	4.800
	$P(L(n) \leq 6)$	0.121	0.125	0.246
	$P(L(n) \leq 10)$	0.979	0.972	0.873

gible and thus (68) can be simplified to:

$$\mu_c \approx np + \frac{\lambda_2(1-p)}{1-\lambda_2}. \tag{71}$$

Next, define σ_c^2 to be the variance of $L_c(n)$:

$$\sigma_c^2 = Var[L_c(n)] = Var[L(n)|X_0 = 1]. \tag{72}$$

Then, we have the following result.

Lemma 12. *Assume that each loss event in a block of length n follows the two-state Markov chain in* (29)*. Then, the variance of $L_c(n)$ for large n is:*

$$\sigma_c^2 \approx (p-1)\Big[np + p + \frac{1-2np-6p}{\gamma} + \frac{5p-1}{\gamma^2}\Big], \tag{73}$$

where $\gamma = 2 - p_{00} - p_{11} \geq \varepsilon > 0$.

Proof. Write the conditional variance σ_c^2 as:

$$\sigma_c^2 = E[L^2(n)|X_0 = 1] - \mu_c^2. \tag{74}$$

Then, we can express the first term of (74) as:

$$E[L^2(n)|X_0 = 1] = E[L(n)|X_0 = 1] + 2\sum_{i=1}^{n-1}\sum_{j=i+1}^{n} E[X_i X_j|X_0 = 1]. \tag{75}$$

Notice that by conditioning on $X_0 = x$, $E[X_i X_j]$ depends on the value of i in addition to the distance $d = j - i$:

$$E[X_i X_j|X_0 = x] = \mathbf{v}B^d\mathbf{v}^T P(X_i = 1|X_0 = x). \tag{76}$$

Using (76) and (70), we obtain:

$$E[X_i X_j|X_0 = 1] = (p + (1-p)\lambda_2^{j-i})(p + (1-p)\lambda_2^i). \tag{77}$$

Denoting by G the double summation term in (75) and expanding it using (77), we have:

$$\begin{aligned} G &= \sum_{i=1}^{n-1}\sum_{j=i+1}^{n} E[X_i X_j|X_0 = 1] \qquad (78)\\ &= \sum_{j=1}^{n-1}\left(p^2 j - p + p^2 + p(1-p)\frac{1-\lambda_2^{j+1}}{1-\lambda_2}\right)\\ &+ \sum_{j=1}^{n-1}\left((p^2-p)j\lambda_2^j - \frac{(1-p)^2}{1-\lambda_2}\lambda_2^{n+1}\right)\\ &+ \sum_{j=1}^{n-1}\left(np(1-p) - (1-p)^2 + \frac{(1-p)^2}{1-\lambda_2}\right)\lambda_2^j. \end{aligned}$$

Let G_1, G_2, and G_3 be the first, second, and third summations in (78), respectively. Expanding each term separately, we get:

$$\begin{aligned} G_1 &= (n-1)\left(\frac{p^2 n}{2} - p + p^2 + \frac{p(1-p)}{1-\lambda_2}\right) - \frac{p(1-p)\lambda_2^2(1-\lambda_2^{n-1})}{(1-\lambda_2)^2},\\ G_2 &= (p^2-p)\lambda_2\frac{(1-n\lambda_2^{n-1})(1-\lambda_2) + \lambda_2(1-\lambda_2^{n-1})}{(1-\lambda_2)^2} - \frac{(1-p)^2}{1-\lambda_2}(n-1)\lambda_2^{n+1},\\ G_3 &= \left((1-p)(np-1+p) + \frac{(1-p)^2}{1-\lambda_2}\right)\frac{\lambda_2(1-\lambda_2^{n-1})}{1-\lambda_2}. \end{aligned}$$

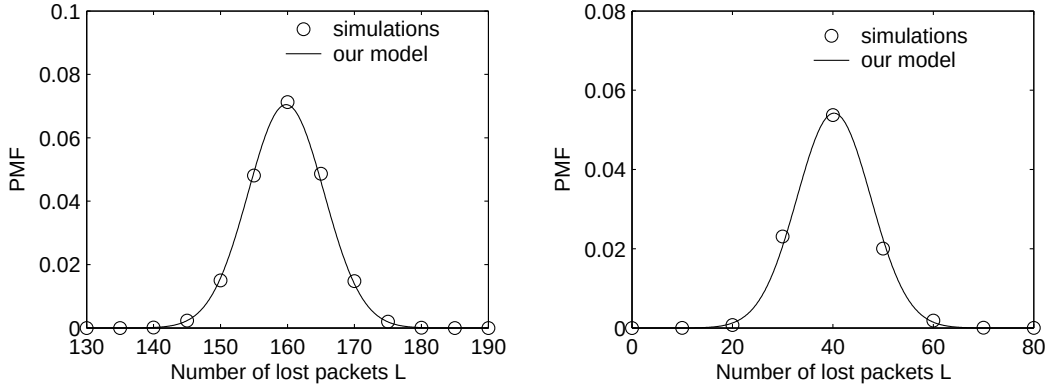

(a) $p = 0.4$ (b) $p = 0.1$

Fig. 18. Distribution of $L_c(n)$ for $n = 400$ and two different p.

Using the same argument for large n as in the previous subsection and dropping terms λ_2^{n-1} and λ_2^{n+1}, we can simplify G_1, G_2, and G_3 to:

$$\begin{aligned} G_1 &= (n-1)\left(\frac{p^2 n}{2} - p + p^2 + \frac{p(1-p)}{1-\lambda_2}\right) - \frac{p(1-p)\lambda_2^2}{(1-\lambda_2)^2}, \\ G_2 &= \frac{(p^2-p)\lambda_2}{1-\lambda_2}\left(1 + \frac{\lambda_2}{1-\lambda_2}\right), \\ G_3 &= \left((1-p)(np-1+p) + \frac{(1-p)^2}{1-\lambda_2}\right)\frac{\lambda_2}{1-\lambda_2}. \end{aligned} \tag{79}$$

Substituting $\lambda_2 = p_{00} + p_{11} - 1$ and using (71) and (79), we obtain (73). □

Combining (68) and (73), the next asymptotic result follows immediately.

Corollary 6. *Assume that each loss event in a block of length n follows the two-state Markov chain in* (29)*. Then, the distribution of $L_c(n)$ for large n is:*

$$L_c(n) \sim N(\mu_c, \sigma_c^2). \tag{80}$$

We next present simulations that show the accuracy of (80). For this example, we use $n = 400$ and two different values of p and plot the distribution of $L_c(n)$ in Fig.

Table VII. Comparison of (80) to Simulations ($p = 0.4$)

n	Metric	Simulations	Model (80)
400	μ_c	159.800	159.800
	σ_c^2	32.053	32.053
	$P(L_c(n) \leq 142)$	0.001	0.001
	$P(L_c(n) \leq 150)$	0.051	0.050
	$P(L_c(n) \leq 170)$	0.971	0.970

18. To demonstrate the numerical match, we compute several metrics of interest for $p = 0.4$ and compare them with (80) in Table VII. As the figure and table show, (80) agrees with simulations very well.

D. Performance of FEC in Scalable Streaming

Our next step is to study the performance of FEC-based video streaming considering two loss patterns and analyze the convergence point of U^H as $H \to \infty$.

Since our main interest in FEC is how its overhead affects the utility of received video, we examine a generic media-independent FEC scheme based on (n, k) block codes (such as parity or Reed-Solomon codes), where n is the total number of packets in an FEC block and k is the number of redundant FEC packets in the block. Thus, the actual number of video data packets in each block is $H = n - k$ and the FEC overhead rate (i.e., fraction of FEC packets) ψ is k/n. Recall that under (n, k) block coding, all H data packets are recovered if the number of lost packets in a block is no more than the number of FEC packets k. However, if the channel loses more than k packets, then only those packets in the enhancement layer located *before the first loss in the block* can be used in decoding.

1. Markov Packet Loss

In this subsection, we first investigate the expected amount of data recovered in each block and in the next subsection analyze the corresponding utility of received video.

To derive $E[Z_j^H]$, we again assume that $L(n)$ is the number of packets lost in a block of size n and define $\bar{Q} = E[Z_j^H \mid L(n) > k]$ to be the expected number of useful video packets recovered from an FEC block when $L(n)$ is greater than the number of FEC packets in the block. The following result states the value of $\bar{Q}$.

Lemma 13. *Assuming a two-state Markov packet loss in* (29) *and* $L(n) > k$*, the expected number of useful video packets recovered per frame is:*

$$\bar{Q} = E[Z_j^H \mid L(n) > k] = \frac{p_{00}p_{11} - \lambda_2}{1 - \lambda_2} \sum_{i=1}^{n-k-1} i p_{00}^{i-1} \frac{P(L_c(n-i-1) > k-1)}{P(L(n) > k)}. \quad (81)$$

Proof. Assume that D_j is the random distance in packets to the first loss in a block j as before. Then, we can obtain $P(D_j = i)$ using the basic properties of Markov chains:

$$P(D_j = i) = \begin{cases} \pi_1 & i = 0 \\ \pi_0 p_{00}^{i-1}(1 - p_{00}) & i \geq 1 \end{cases}. \quad (82)$$

Next, write $\bar{Q}$ as:

$$\bar{Q} = E[Z_j^H | L(n) > k] = \sum_{i=1}^{n-k-1} i P(D_j = i | L(n) > k).$$

Using Bayes' formula, we can get:

$$P(D_j = i | L(n) > k) = \frac{P(L(n) > k | D_j = i) P(D_j = i)}{P(L(n) > k)}. \quad (83)$$

Next note that we can compute:

$$P(L(n) > k | D_j = i) = P(L_c(n-i-1) > k-1), \quad (84)$$

Table VIII. Comparison of (81) to Simulations

$p = 0.4$, $n = 400$, $\sigma^2 = 32.106$			
k	$P(L(n) > k)$	$\bar{Q}$ in simulations	$\bar{Q}$ in (81)
170	0.0307	0.802	0.807
165	0.1656	0.863	0.865
160	0.4674	0.919	0.920
155	0.7874	0.964	0.963
140	0.9996	0.999	0.999
0	1.0000	1.000	1.000
$p = 0.1$, $n = 400$, $\sigma^2 = 54.943$			
k	$P(L(n) > k)$	$\bar{Q}$ in simulations	$\bar{Q}$ in (81)
50	0.0809	8.245	8.002
45	0.2224	8.905	8.800
40	0.4593	9.604	9.601
30	0.9068	10.813	10.840
20	0.9983	11.231	11.224
0	1.0000	11.250	11.250

which represents the probability of losing more than $k-1$ packets from $n-i-1$ transmitted ones conditioned on the $(i+1)$-st packet being lost.

Finally, recalling that $\pi_0 = (1-p_{11})/(2-p_{00}-p_{11}) = (1-p_{11})/(1-\lambda_2)$ and with the help of (83), (84), and (82), we get (81). □

Notice that by utilizing the models derived in section C., we can compute for asymptotically large n each of the terms in (81) individually, which in turn allows us to calculate $\bar{Q}$. To verify (81), we compute $\bar{Q}$ in simulations and show the result in Table VIII. For the first case, we use large packet loss $p = 0.4$ ($p_{00} = 0.4$, $p_{11} = 0.1$), $n = 400$, and over 1 billion iterations. As the table shows, (81) matches simulation results very well. For the second case, we use smaller packet loss $p = 0.1$ ($p_{00} = 0.92$, $p_{11} = 0.28$) and observe in the table that (81) is reasonably accurate as well. It is worth noting that the model is more accurate when np is large or $\sigma^2 < np$. Thus,

due to the small np and $\sigma^2 > np$, the match in the second case in Table VIII is not as good as that in the first case.

Using the result in (81), we easily get $E[Z_j^H]$.

Corollary 7. *Assuming two-state Markov packet loss with average loss probability p, the expected number of useful packets recovered per FEC block of size n is:*

$$E[Z_j^H] = P(L(n) \leq k)H + P(L(n) > k)\bar{Q}. \tag{85}$$

2. Utility

Defining a new metric $C(n) = \bar{Q}P(L(n) > k)$ and re-writing (28) using (85), we get:

$$U^H = \frac{P(L(n) \leq k)H + C(n)}{n(1-p)}. \tag{86}$$

For convenience of presentation, define the overhead rate ψ as a linear function of packet loss: $\psi = \eta p$ (where η is a constant). Then, we have in the next theorem the asymptotic behavior of U^H as the video rate becomes large.

Theorem 8. *Assuming a two-state Markov packet loss in an FEC block of size n, average loss probability p, and FEC overhead rate $\psi = \eta p$, $(0 < \psi < 1)$, the utility of received video for each FEC block converges to the following:*

$$\lim_{H\to\infty} U^H = \begin{cases} 0 & 0 < \eta < 1 \\ 0.5 & \eta = 1 \\ \dfrac{1-\psi}{1-p} & 1 < \eta < 1/p \end{cases}. \tag{87}$$

Proof. Recalling that the distribution of $L(n)$ is asymptotically normal with param-

eters μ and σ^2 as discussed in Section C.4, we can write:

$$P(L(n) \leq k) = \int_{-\infty}^{k} f(x)dx, \tag{88}$$

where $f(x)$ is the PDF of $L(n)$.

Define $\phi(x)$ to be the PDF of the standard normal distribution and let $z = (k-\mu)/\sigma$. Then, re-write (88) as:

$$P(L(n) \leq k) = \int_{-\infty}^{z} \phi(x)dx. \tag{89}$$

Using $\psi = \eta p$ and $k = \psi n$, re-write z as:

$$z = \frac{(\eta - 1)\sqrt{(H+k)p}}{\sqrt{(1-p)\dfrac{p_{00}+p_{11}}{2-p_{00}-p_{11}}}}. \tag{90}$$

Notice that $(p_{00}+p_{11})/(2-p_{00}-p_{11}) > 0$ and observe from (90) that as $H \to \infty$, $z \to -\infty$ if $\eta < 1$, $z \to \infty$ if $\eta > 1$, and $z = 0$ if $\eta = 1$. Thus, the probability $P(L(n) \leq k)$ in (89) converges to the following as $H \to \infty$:

$$\lim_{H\to\infty} P(L(n) \leq k) = \begin{cases} 0 & 0 < \eta < 1 \\ 0.5 & \eta = 1 \\ 1 & 1 < \eta < 1/p \end{cases}. \tag{91}$$

Next, observe in (81) that since $P(L_c(n-i-1) > k-1)$ is less than or equal to 1, $C(n)$ is upper-bounded by:

$$C(n) \leq \frac{p_{00}p_{11} - \lambda_2}{1-\lambda_2} \sum_{i=1}^{n-k-1} i p_{00}^{i-1} = \frac{p_{00}p_{11} - \lambda_2}{1-\lambda_2} \bar{C}, \tag{92}$$

where

$$\bar{C} = \sum_{i=1}^{n-k-1} i p_{00}^{i-1}. \tag{93}$$

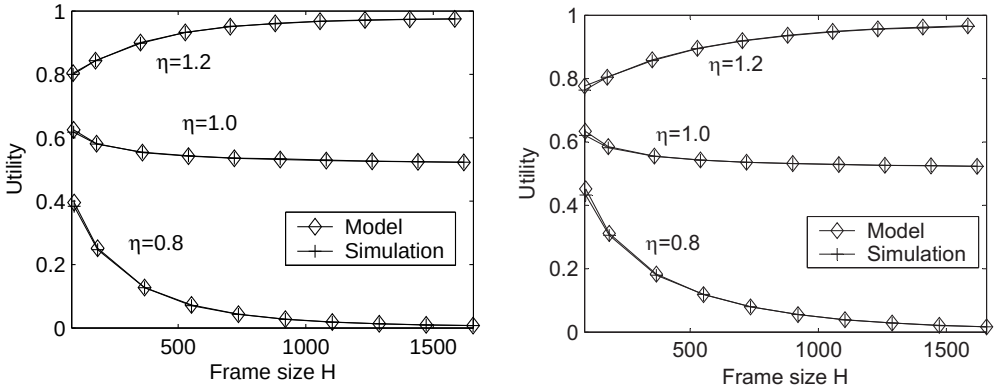

(a) Bernoulli loss (b) Markov loss

Fig. 19. Simulation results of U^H and their comparison to model (87) for Bernoulli loss and Markov loss ($p_{00} = 0.92, p_{11} = 0.28$). In both figures, $p = 0.1$.

Recalling that $p_{00} > 0$ and expanding (93), we get:

$$\bar{C} = \frac{1 + (n-k-1)p_{00}^{n-k} - (n-k)p_{00}^{n-k-1}}{(1-p_{00})^2}. \tag{94}$$

Since $\bar{C}/n \to 0$ as $n \to \infty$, so does $C(n)/n$. Thus, using (91) in (86), and utilizing the fact that $H = n(1-\psi)$, we immediately get (87). □

We next verify the asymptotic characteristics of the achieved utility in (87). Before considering a general Markov loss model, we first examine a special case with $p_{00} = 1-p$ (i.e., Bernoulli loss). Fig. 19(a) plots simulation results of U^H for different η and compare them with (87). As the figure shows, (87) matches simulations very well and U^H indeed converges to 0, 0.5 or $(1-\psi)/(1-p) = 0.9778$ as the streaming rate becomes high. For the general Markov loss case, we plot simulation results U^H and compare them with the values predicted by (87) for three different values of η in Fig. 19(b). As the figure shows, U^H follows a trend similar to that in the Bernoulli case with the exception of a slightly slower convergence rate (Markov chains with

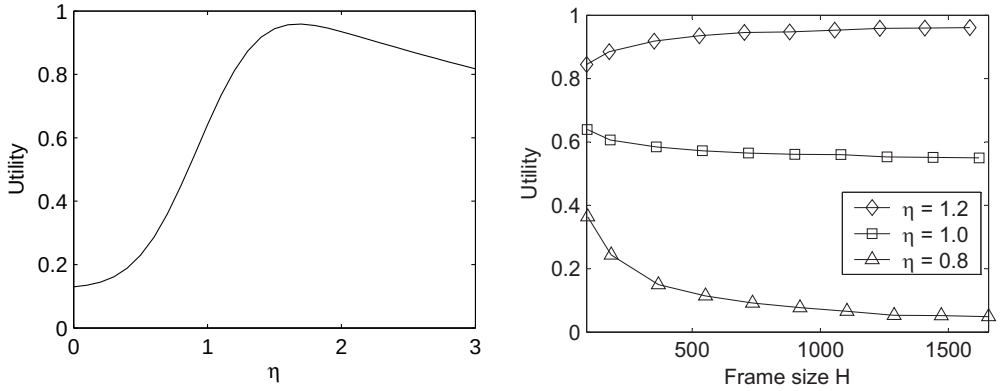

(a) U^H for finite n (b) Renewal loss

Fig. 20. (a) U^H computed from (86) for $n = 100$ and different values of η. (b) Simulation results of U^H for renewal loss. In both figures, $p = 0.1$.

dependency between the states are more slowly mixing than the Bernoulli case). For instance, under the Markov-chain loss, $U^{1800} = 0.016$ for $\eta = 0.8$, while the Bernoulli case has $U^{1800} = 0.007$ for the same value of η (see Fig. 19).

In summary, the above result on U^H implies that 1) the amount of overhead used in FEC has a significant impact on the quality of received video; 2) U^H asymptotically achieves its maximum when the amount of overhead $\psi = \eta p$ is just slightly larger than the average network loss p. Note, however, that when the streaming rate is finite (i.e., $n < \infty$), U^H depends on n as well as η and the optimal amount of overhead can be determined by maximizing (86). To demonstrate this, we show one such example with finite $n = 100$ and $p = 0.1$ in Fig. 20(a). As the figure shows, U^H reaches its maximum at $\eta = 1.7$, which is much larger than that predicted by (87). We leverage this result later in the chapter and next focus on more generic patterns of packet loss.

3. Renewal Packet Loss

In this section, we study U^H under ON/OFF renewal packet loss. Similarly to the result in (85) discussed in Section D.1, we model the amount of useful data recovered from an FEC block as:

$$E[Z_j^H] = E[Z_j^H|L(t) \leq k]P(L(t) \leq k) + E[Z_j^H|L(t) > k]P(L(t) > k), \tag{95}$$

where $L(t) = \int_t^{t+n} V(u)du$ is the number of lost packets in a block of size n starting at time instant t and $V(u)$ is the ON/OFF process described in Section B.2. Unfortunately, computing distribution $P(L(t) \leq k)$ under an ON/OFF renewal process appears to be impossible in closed form even though many studies (e.g., [97]) have attempted this task in the last 50 years. Hence, we do not pursue this direction further and show instead convergence of U^H using simulations without offering a closed-form model.

For this case, we generate 20 million random values for ON and OFF durations, where each of X_i and Y_i are *i.i.d.* Pareto. We use $E[Y_i] = 10$ and $E[X_i] = E[Y_i]p/(1-p)$ so as to keep the average loss equal to p and plot the simulation results of U^H for different values of η and $p = 0.1$ in Fig. 20(b). As the figure shows, U^H again exhibits a percolation point around $\eta = 1$ (i.e., $\psi = p$) and converges to three different values depending on η.

The final question we address is whether U^H converges to the same values as in the Markov case. We conduct simulations using very large n and several values of p. For each value of p, we identify a convergence point, at which increasing H virtually does not change the value of U^H (change in U^H after doubling the value of H is less than 0.001) and illustrate in Table IX convergence values of U^H for $\eta = 1.2$. As the table shows, U^H approaches to $(1-\psi)/(1-p)$ regardless of the value of p. This is the

Table IX. Utilities in Simulation (Renewal Loss)

Packet loss p	Convergence point	$(1-\psi)/(1-p)$
0.01	0.9974	0.9979
0.1	0.9775	0.9777
0.2	0.9496	0.9500
0.4	0.8665	0.8666

same asymptotic result observed in the Markov loss case discussed in the previous subsection. We also found that U^H converges to 0.5 for $\eta = 1$ and 0 for $\eta < 1$, but omit these results for brevity. This demonstrates that as long as the application can measure p, the behavior of U^H for large n is almost the same under many fairly general conditions of network loss.

The next question we address is how to select the proper amount of overhead such that U^H is maximized for a given streaming rate H and network packet loss p.

E. Adaptive FEC Control

1. Framework

In a practical network environment (such as the Internet), packet loss is not constant and changes dynamically depending on cross traffic, link quality, routing updates, etc. Hence, streaming servers must often adjust the amount of FEC overhead according to changing packet loss to maintain high end-user utility.

To remain friendly to other applications in the Internet and avoid filling network paths with unnecessary FEC packets, a streaming server must comply with the sending rate S suggested by its congestion control algorithm. Given S, the streaming server then determines FEC rate F and video source rate R such that $S = R + F$. Recall that to achieve high end-user utility, overhead rate ψ must be slightly higher

than packet loss p as discussed in Section D; however, the exact value of optimal ψ^* depends on the streaming rate and current packet loss p (the latter of which is generally coupled with congestion control and should be provided by its feedback loop).

Next, we discuss a simple approach that can select the proper amount of FEC overhead using our previous analysis. The main problem is how to select optimal η^* for a given packet loss p and FEC block size n to achieve maximum utility. One simple solution is to construct an optimization problem around (86):

$$\eta^* = \arg\max_{\eta} U^H(\eta, p, n), \tag{96}$$

which can be easily solved using binary search and applying models developed in the previous section as long as packet loss p, block size n, and Markov properties of the loss process are known. In practice, this can be implemented by fitting a Markov model to the measured loss events and maximizing utility in (96) regardless of whether the actual network loss exhibits Markovian properties or not. Simulations below suggest that the actual distribution of loss-burst lengths does not have a significant effect on the result.

2. Evaluation Setup

In this section, we present simulation results of our adaptive FEC-based scheme including the properties of U^H and video quality. We first simulate a Markov loss process, obtain packet loss statistics for each video frame, and examine the resulting utility and PSNR video quality of our method in comparison to two approaches that use fixed amounts of FEC overhead. We then conduct `ns2` [73] simulations to briefly investigate whether the results obtained from the Markov model are valid in more realistic network environments. In all simulations, one video frame ($40,000$

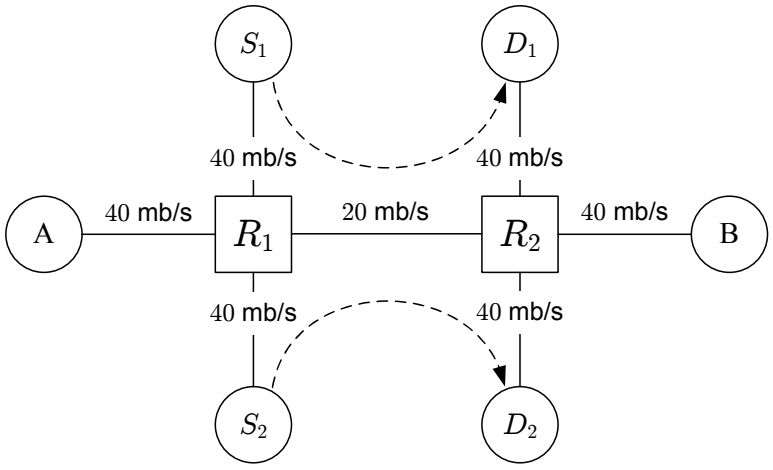

Fig. 21. `ns2` simulation topology.

bytes without including the base layer) consists of 200 packets, 200 bytes each (these numbers are derived from MPEG-4 coded CIF Foreman with a 128-kb/s base layer coded at 10 frames per second). For convenience of PSNR computation and to keep overhead reasonable, we use FEC block size $n = 200$ packets.

For `ns2` simulations, we use a simple topology shown in Fig. 21, in which video source A sends packets at 3.2 mb/s to receiver B over a single bottleneck link of capacity 20 mb/s. To congest the bottleneck link, we use N FTP connections between nodes S_1 and D_1 and 400 HTTP sessions between nodes S_2 and D_2. All access links are 40 mb/s. Each cross-traffic flow starts randomly and N varies over time to produce different values of network packet loss $p(t)$.

We start our investigation with the behavior of utility U^H.

3. Properties of U^H

To illustrate the adaptivity of (96), we first present results based on Markov loss simulations in Matlab. In this example, we simulate a streaming session with a hypothetical packet loss pattern shown in Fig. 22(a). The evolution of $p(t)$ in Fig.

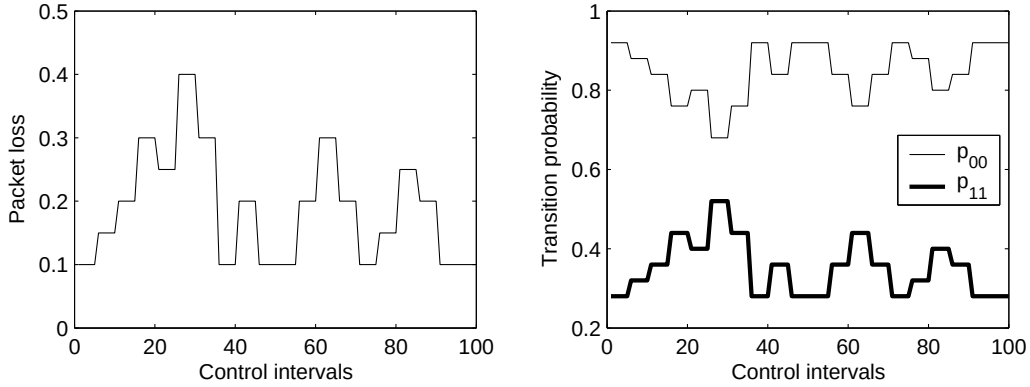

(a) Packet loss pattern (b) p_{00}, p_{11}

Fig. 22. Packet loss pattern obtained through Markov-chain simulation using transition probabilities p_{00} and p_{11}.

22(a) is obtained using the Markov chain in (29) with transition probabilities p_{00} and p_{11} plotted in Fig. 22(b). We consider two different fixed-overhead schemes (we call them M_1 and M_2 hereafter) to compare with our adaptive method. To determine the fixed amount of overhead, M_1 and M_2 use the lower ($p_L = 0.1$) and upper ($p_U = 0.4$) bounds on packet loss in Fig. 22(a), respectively.

We plot the achieved utility of FEC-protected video in Fig. 23. As the figure shows, (96) maintains its utility very high (in fact approaching the optimal value of U^H) along the entire streaming session with small deviations only at points when $p(t)$ transitions to its new value. Also observe in the figure that fixed-overhead schemes M_1 and M_2 perform much worse even though M_2 sends *more* FEC than our scheme.

Next, we examine how (96) behaves under changing $p(t)$ obtained from `ns2` simulations. In this case, we vary the number of FTP connections N every 5 control intervals and measure long-term average packet loss at the receiver. The relationship between N and the long-term average loss is illustrated in Fig. 24(a) where

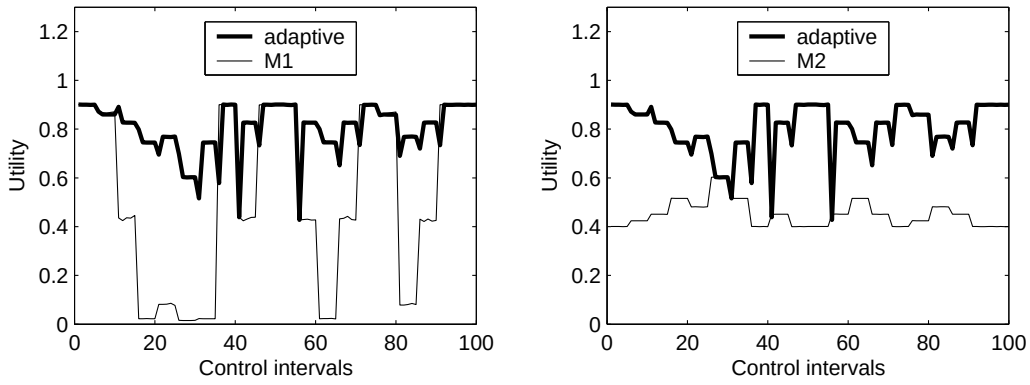

(a) $p_L = 0.1$ (b) $p_U = 0.4$

Fig. 23. Metric U^H achieved by the adaptive FEC overhead controller (96) and its comparison to utilities obtained in two different scenarios that use fixed amounts of overhead.

the increase in packet loss is caused by the well-known TCP scalability properties [20]. Changing the value of N randomly over time, the network exhibits fluctuating packet loss shown in Fig. 24(b). Using this information, the sender estimates transition probabilities p_{00} and p_{11} for each interval and uses them in FEC control. Figs. 25(a) and 25(b) plot the evolution of U^H achieved by different FEC-control schemes and show that our adaptive controller exhibits behavior similar to that observed in Markov-loss simulations.

Analysis in previous sections suggests that both correlated and uncorrelated loss patterns, as well as exponential and heavy-tailed loss-burst lengths, lead to an almost identical behavior of U^H. Additional simulations with `ns2` confirm that results based on simple Markov-loss models can indeed be used as first-step approximations to the real behavior of U^H in generic networks. Future work will examine this issue in more detail and attempt to understand how more complex loss patterns influence optimal selection of FEC overhead.

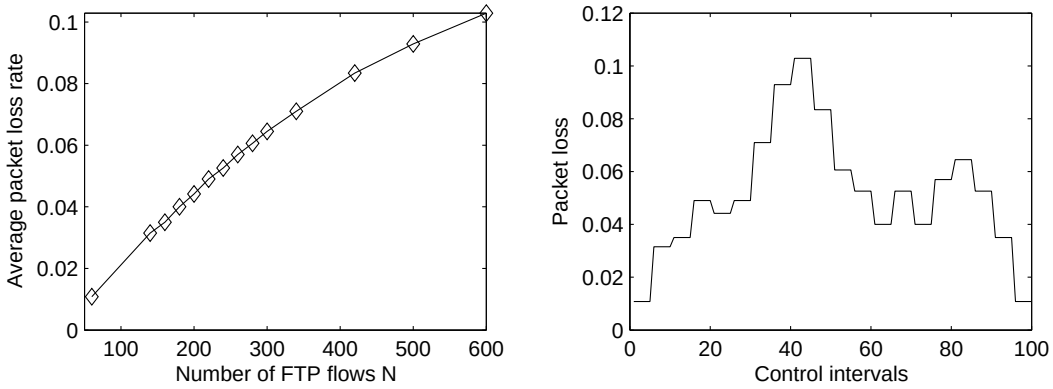

(a) Average loss rate (b) Packet loss pattern

Fig. 24. (a) Average packet loss rate for different number of FTP flows N in `ns2` simulation. (b) Packet loss pattern obtained through ns2 simulation.

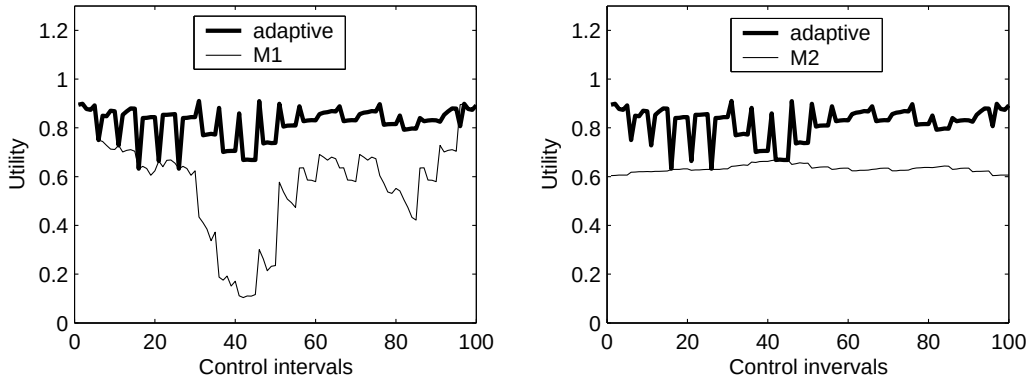

(a) $p_L = 0.01$ (b) $p_U = 0.1$

Fig. 25. Evolution of U^H achieved by the adaptive FEC overhead controller (96) and its comparison to that of utilities obtained in two different scenarios that use fixed amounts of overhead.

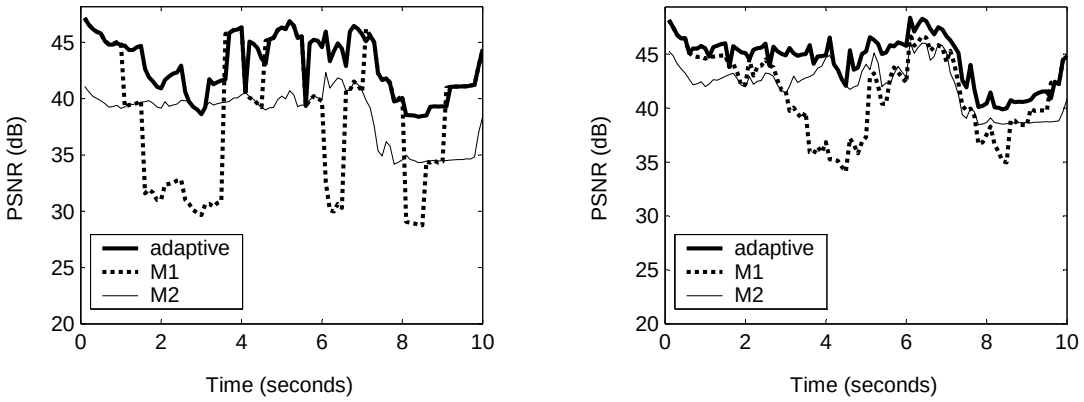

(a) Markov loss simulation (b) `ns2` simulation

Fig. 26. PSNR of CIF Foreman reconstructed with different FEC overhead control.

4. PSNR Quality

We finish the chapter by comparing the adaptive method with fixed-FEC schemes using PSNR quality curves. We apply packet-loss information obtained through `ns2` and Markov chain simulations to each MPEG-4 FGS frame of the Foreman video sequence. We enhance each base-layer frame using consecutively received FGS packets and plot PSNR quality curves accordingly. Note that for this comparison, we protected the entire base layer in all cases and allow random loss only in the FGS layer.

Fig. 26 plots PSNR curves for both simulation cases. Observe in Fig. 26(a) that M_1 suffers significant quality degradation when U^H drops around $t = 2$ seconds (see Fig. 23(a)). Similarly, M_2 exhibits suboptimal video quality during the entire streaming session due to its ψ being too large. Compared to the two cases M_1 and M_2, our adaptive method offers almost 6 dB higher PSNR than M_2 throughout the session and out-performs M_1 by almost 10 dB for half the duration of the streaming

session.[7] Fig. 26(b) shows that the improvement in `ns2` simulations is not as dramatic as that in the Markov example due to the lower packet loss rates, but nevertheless amounts to a 3 to 9 dB improvement.

[7]Note that a 1-dB gain in PSNR is usually considered significant [100].

CHAPTER V

BANDWIDTH ESTIMATION: STOCHASTIC ANALYSIS

This chapter examines the problem of estimating the capacity and available bandwidth of end-to-end paths under non-negligible cross-traffic conditions. In the first half of this chapter, we present a stochastic analysis of the problem in the context of a single congested node and derive several results that allow the construction of asymptotically-accurate bandwidth estimators. We develop a generic queuing model of an Internet router and propose a filtering solution that asymptotically converges to the desired values of the bottleneck capacity and available bandwidth under arbitrary (including non-stationary) cross-traffic. This is one of the first methods that simultaneously estimates both types of bandwidth and is provably accurate. In the second half, we focus on measuring both bandwidth metrics of the tight-link over a multi-hop path using recursive extension of the single-hop model developed in the first half. Using a new probing technique called Envelope based on the recursive model, we develop an asymptotically accurate bandwidth estimator that optimally selects probing parameters according to various network conditions and significantly outperforms existing methods in terms of estimation accuracy.

A. Introduction

Bandwidth estimation has recently become an important and mature area of Internet research [1], [2], [14], [22], [23], [35], [41], [43], [44], [52], [54], [55], [70], [72], [76], [77], [78], [84], [85], [93], [96], [101]. A typical goal of these studies is to understand the characteristics of Internet paths and those of cross-traffic through a variety of

end-to-end and/or router-assisted measurements. The proposed techniques usually fall into two categories – those that estimate the bottleneck bandwidth [14], [22], [23], [49] and those that deal with the available bandwidth [43], [72], [85], [96]. Recall that the former bandwidth metric refers to the capacity of the slowest link of the path, while the latter is generally defined as the smallest average unused bandwidth among the routers of an end-to-end path.

The majority of existing bottleneck-bandwidth estimation methods are justified assuming no cross-traffic along the path and are usually examined in simulations/experiments to show that they can work under realistic network conditions [14], [22], [23], [35]. With available bandwidth estimation, cross-traffic is essential and is usually taken into account in the analysis; however, such analysis predominantly assumes a fluid model for all flows and implicitly requires that such models be accurate in non-fluid cases. Simulations/experiments are again used to verify that the proposed methods are capable of dealing with bursty conditions of real Internet cross-traffic [44], [72], [85], [96].

To understand some of the reasons for the lack of stochastic modeling in this field, this work studies a *single-node* bandwidth measurement problem and derives a closed-form estimator for both capacity C and available bandwidth $A = C - \bar{r}$, where $\bar{r}$ is the average rate of cross-traffic at the link. For an arbitrary cross-traffic arrival process $r(t)$, we define $\bar{r}$ as the asymptotic time-average of $r(t)$ and assume that it exists and is finite:

$$\bar{r} = \lim_{t \to \infty} \frac{1}{t} \int_0^t r(u)du < \infty. \tag{97}$$

Notice that the existence of (97) does not require stationarity of cross-traffic, nor does it impose any restrictions on the arrival of individual packets to the router. While other definitions of available bandwidth A and the average cross-traffic rate

$\bar{r}$ are possible, we find that (97) serves our purpose well as it provides a clean and mathematically tractable metric.

In this chapter, we first deals with bandwidth estimation under *i.i.d.* renewal cross-traffic and the analysis of packet-pair/train methods. We first show that under certain conditions and even the simplest *i.i.d.* cross-traffic, histogram-based methods commonly used in prior work (e.g., [22]) can be misled into producing inaccurate estimates of C. We overcome this limitation by developing an asymptotically accurate model for C; however, since this approach eventually requires ergodicity of cross-traffic, we later build another model that imposes more restriction on the sampling process (using PASTA principles suggested in [96]), but allows cross-traffic to exhibit arbitrary characteristics.

Unlike previous studies [96], we prove that the corresponding PASTA-based estimators converge to the correct values and show that they can be used to simultaneously measure capacity C and available bandwidth A. To our knowledge, this is the first estimator that measures both C and A without congesting the link, assumes non-negligible, non-fluid cross-traffic in the derivations, and applies to non-stationary $r(t)$.

B. Stochastic Queuing Model

In this section, we build a simple model of a router that introduces random delay noise into the measurements of the receiver and use it to study the performance of packet-pair bandwidth-sampling techniques. Note that we depart from the common assumption of negligible and/or fluid cross-traffic and specifically aim to understand the effects of random queuing delays on the bandwidth sampling process. First consider an unloaded router with no cross-traffic. The packet-pair mechanism is based

on an observation that if two packets arrive at the bottleneck link with spacing x smaller than the transmission delay Δ of the second packet over the link, their spacing after the link will be exactly Δ. In practice, however, packets from other flows often queue between the two probe packets and increase their spacing on the exit from the bottleneck link to be larger than Δ.

Assume that packets of the probe traffic arrive to the bottleneck router at times a_1, $a_2, \ldots$ and that inter-arrival times $a_n - a_{n-1}$ are given by a random process x_n determined by the server's initial spacing. Further assume that the bottleneck node delays arriving packets by adding a random processing time ω_n to each received packet n. For the remainder of the chapter, we use constant[1] packet size q for the probing flow and arbitrarily-varying packet sizes for cross-traffic. Furthermore, there is no strict requirement on the initial spacing x_n as long as the modeling assumptions below are satisfied. This means that both isolated packet pairs or bursty packet trains can be used to probe the path. Let the transmission delay of each application packet through the bottleneck link be $q/C = \Delta$, where C is the transmission capacity of the link. Under these assumptions, packet departure times d_n are expressed by the following recurrence[2]:

$$d_n = \begin{cases} a_1 + \omega_1 + \Delta & n = 1 \\ \max(a_n, d_{n-1}) + \omega_n + \Delta & n \geq 2 \end{cases}. \tag{98}$$

In this formula, the dependence of d_n on departure time d_{n-1} is a consequence of FIFO queuing (i.e., packet n cannot depart before packet $n-1$ is fully transmitted). Furthermore, packet n cannot start transmission until it has fully arrived (i.e., time

[1]Methods that vary the probing packet size also exist (e.g., [23], [41]).

[2]Times d_n specify when the *last* bit of the packet leaves the router. Similarly, times a_n specify when the last bit of the packet is fully received and the packet is ready for queuing.

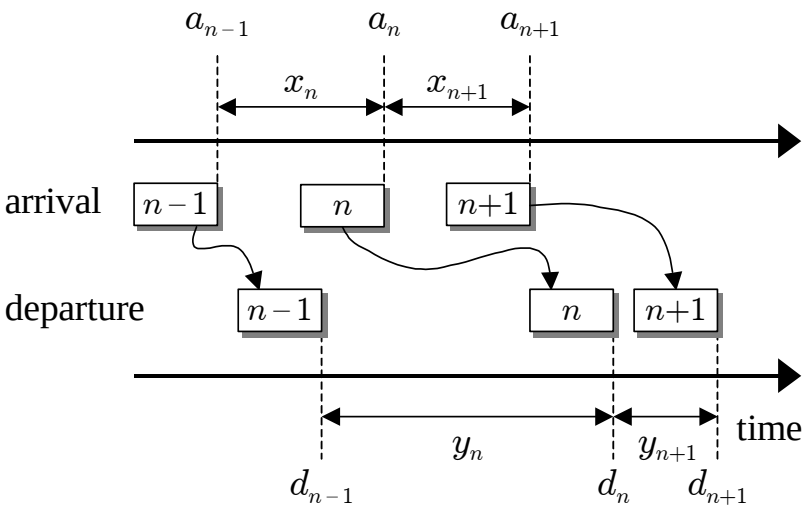

Fig. 27. Departure delays introduced by the node.

a_n). The value of the noise term ω_n is proportional to the number of packets generated by cross-traffic and queued in front of packet n. The final metric of interest is inter-departure delay $y_n = d_n - d_{n-1}$ as the packets leave the router. The various variables and packet arrival/departure are schematically shown in Figure 27.

Even though the model in (98) appears to be simple, it leads to fairly complicated distributions for y_n if we make no prior assumptions about cross-traffic. We next examine several special cases and derive important asymptotic results about process y_n.

C. Renewal Cross-Traffic

1. Packet-Pair Analysis

We start our analysis with a rather common assumption in queuing theory that cross-traffic arrives into the bottleneck link according to some renewal process (i.e., delays between cross-traffic packets are *i.i.d.* random variables). In what follows in the next few subsections, we show that modeling of this direction requires stationarity (more

specifically, ergodicity) of cross-traffic. However, since neither the *i.i.d.* assumption nor stationarity holds for regular Internet traffic, we then apply a different sampling methodology and a different analytical direction to derive a provably robust estimator of capacity C and average cross-traffic rate $\bar{r}$.

The goal of bottleneck bandwidth sampling techniques is to queue probe packets directly behind each other at the bottleneck link and ensure that spacing y_n on the exit from the router is Δ. In practice, however, this is rarely possible when the rate of cross-traffic is non-negligible. This does present certain difficulties to the estimation process; however, assuming a single congested node, the problem is asymptotically tractable given certain mild conditions on cross-traffic. We present these results below.

To generate measurements of the bottleneck capacity, it is commonly derived that the server must send its packets with initial spacing no more than Δ (i.e., no slower than C). This is true for *unloaded* links; however, when cross-traffic is present, the probes may be sent arbitrarily slower as long as each packet i arrives to the router before the departure time of packet $i-1$. This condition translates into $a_n \leq d_{n-1}$ and (98) expands to:

$$d_n = \begin{cases} a_1 + \omega_1 + \Delta & n = 1 \\ d_{n-1} + \omega_n + \Delta & n \geq 2 \end{cases}. \tag{99}$$

From (99), packet inter-departure times y_n after the bottleneck router are given by:

$$y_n = d_n - d_{n-1} = \Delta + \omega_n, \quad n \geq 2. \tag{100}$$

Notice that random process ω_n is defined by the arrival pattern of cross-traffic and also by its packet-size distribution. Since this process is a key factor that determines the distribution of sampled delays y_n, we next focus on analyzing its properties.

Assume that inter-packet delays of cross-traffic are given by independent random variables $\{X_i\}$ and the actual arrivals occur at times $X_1, X_1 + X_2, \ldots$ Thus, the arrival pattern of cross-traffic defines a renewal process $M(t)$, which is the number of packet arrivals in the interval $[0, t]$. Using common convention, further assume that the mean inter-arrival delay $E[X_i]$ is given by $1/\lambda$, where $\lambda = \bar{r}$ is the mean arrival rate of cross-traffic in packets per second.

To allow random packet sizes, assume that $\{S_j\}, j = 1, 2, \ldots$ are independent random variables modeling the size of packets in cross-traffic. We further assume that the bottleneck link is probed by a sequence of packet-pairs, in which the delay between the packets *within each pair* is small (so as to keep their rate higher than C) and the delay *between the pairs* is high (so as not to congest the link). Under these assumptions, the amount of cross-traffic data received by the bottleneck link between probe packets $2m - 1$ and $2m$ (i.e., in the interval $(a_{2m-1}, a_{2m}]$) is given by a cumulative reward process:

$$v_n = \sum_{j=1}^{M(a_n)-M(a_{n-1})} S_j, \quad n = 2m, \tag{101}$$

where n represents the sequence number of the second packet in each pair. For now, we assume a general (not necessarily equilibrium) process $M(t)$ and re-write (100) as:

$$y_n = \Delta + \frac{v_n}{C} = \Delta + \frac{\sum_{j=1}^{M(a_n)-M(a_{n-1})} S_j}{C}, \quad n = 2m. \tag{102}$$

Since classical renewal theory is mostly concerned with limiting distributions, y_n by itself does not lead to any tractable results because the observation period of the process captured by each of y_n is very small.

Define a time-average process W_n to be the average of $\{y_i\}$ up to time n:

$$W_n = \frac{1}{n}\sum_{i=1}^{n} y_i. \tag{103}$$

Then, we have the following result.

Theorem 9. *Assuming ergodic cross-traffic, time-average process W_n converges to:*

$$\lim_{n\to\infty} W_n = \Delta + \frac{\lambda E[x_n]E[S_j]}{C} = \Delta + E[\omega_n], \tag{104}$$

where $E[x_n]$ is the mean inter-probe delay of packet-pairs.

Proof. Process W_n samples a much larger span of $M(t)$ and has a limiting distribution as we demonstrate below. Applying Wald's equation to (102) [102]:

$$E\left[y_n\right] = \Delta + \frac{E[M(a_n) - M(a_{n-1})]E[S_j]}{C}. \tag{105}$$

The last result holds since $M(t)$ and S_j are independent and $M(a_n) - M(a_{n-1})$ is a stopping time for sequence $\{S_j\}$. Equation (105) can be further simplified by noticing that $E[M(t)]$ is the renewal function $m(t)$:

$$E\left[y_n\right] = \Delta + \frac{(m(a_n) - m(a_{n-1}))E[S_j]}{C}. \tag{106}$$

Assuming stationary cross-traffic, (106) expands to [102]:

$$E\left[y_n\right] = \Delta + \frac{\lambda E[x_n]E[S_j]}{C}. \tag{107}$$

Finally, assuming ergodicity of cross-traffic (which implies that of process y_n), we can obtain (107) using a large number of packet pairs as the limit of W_n in (103) as $n \to \infty$. □

Notice that the second term in (104) is strictly positive under the assumptions of this work. This leads to an interesting observation that the filtering problem

we are facing is quite challenging since the sampled process y_n represents signal Δ corrupted by a *non-zero-mean* noise ω_n. This is a drastic departure from the classical filter theory, which mostly deals with zero-mean additive noise. It is also interesting that the only way to make the noise zero-mean is to either send probe traffic with $E[x_n] = 0$ (i.e., infinitely fast) or to have no cross-traffic at the bottleneck link (i.e., $\lambda = \bar{r} = 0$). The former case is impossible since x_n is always positive and the latter case is a simplification that we explicitly want to avoid in this work.

We will present our analysis of packet-train probing shortly, but in the mean time, discuss several simulations to provide an intuitive explanation of the results obtained so far.

2. Simulations

Before we proceed to estimation of C, let us explain several observations made in previous work and put them in the context of our model in (102) and (104). For the simulations in this section, we used the `ns2` network simulator with the topology shown in Fig. 28. In the figure, the source of probe packets `Snd1` sends its data to receiver `Rcv1` across two routers R_1 and R_2. The speed of all access links is 100 mb/s (delay 5 ms), while the bottleneck link $R_1 \rightarrow R_2$ has capacity $C = 1.5$ mb/s and 20 ms delay. Note that there are five cross-traffic sources attached to `Snd2`.

We next discuss simulation results obtained under UDP cross-traffic. In the first case, we initialize all five sources in `Snd2` to be CBR streams, each transmitting at 200 kb/s ($\bar{r} = 1$ mb/s total cross-traffic). Each CBR flow starts with a random initial delay to prevent synchronization with other flows and uses 500-byte packets. The probe flow at `Snd1` sends its data at an average rate of 500 kb/s for the probing duration, which results in 100% utilization of the bottleneck link. In the second case, we lower packet size of cross-traffic to 300 bytes and increase its total rate to 1.3 mb/s

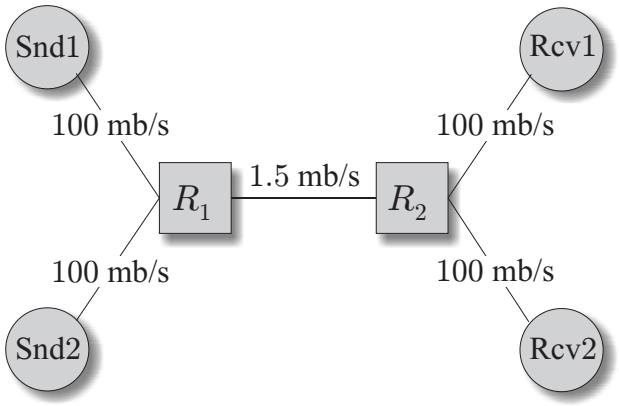

Fig. 28. Single-link simulation topology.

to demonstrate more challenging scenarios when there is packet loss at the bottleneck.

These simulation results are summarized in Fig. 29, which illustrates the distribution of the measured samples y_n based on each pair of packets sent with spacing $x_n \leq \Delta$ (the results exclude packet pairs that experienced loss). Given capacity $C = 1.5$ mb/s and packet size $q = 1,500$ bytes, the value of Δ is 8 ms. Fig. 29 shows that none of the samples are located at the correct value of 8 ms and that the mean of the sampled signal (i.e., W_n) has shifted to 11.7 ms for the first case and 14.5 ms for the second one.

Next, we employ TCP cross-traffic, which is generated by five FTP sources attached to `Snd2`. The TCP flows use different packet sizes of 540, 640, 840, 1,040, and 1,240 bytes, respectively. The histogram of y_n for this case is shown in Fig. 30 for two different average cross-traffic rates $\bar{r} = 750$ kb/s and $\bar{r} = 1$ mb/s. As seen in the figure, even though some of the samples are located at 8 ms, the majority of the mass in the histogram (including the peak modes) are located at the values much higher than 8 ms.

Recall from (104) that W_n of the measured signal tends to $\Delta + E[\omega_n]$. Under CBR cross-traffic, we can estimate the mean of the noise $E[\omega_n]$ to be approximately

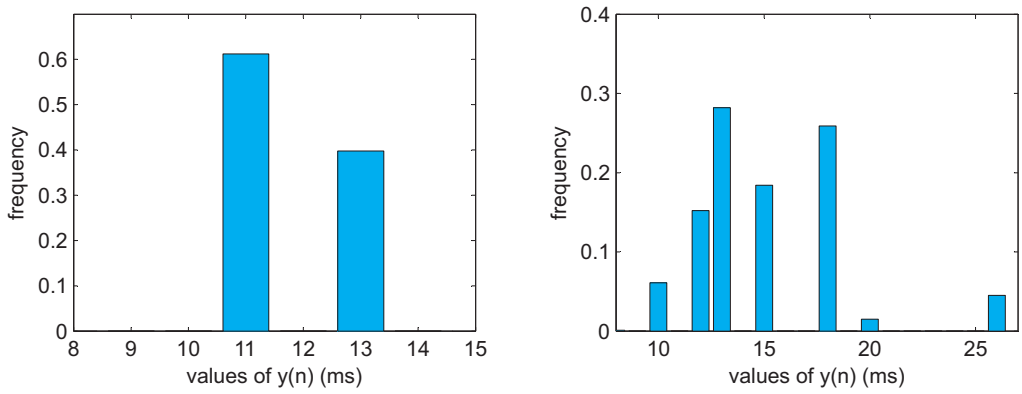

(a) $\bar{r} = 1$ mb/s (b) $\bar{r} = 1.3$ mb/s

Fig. 29. The histogram of measured inter-arrival times y_n under CBR cross-traffic.

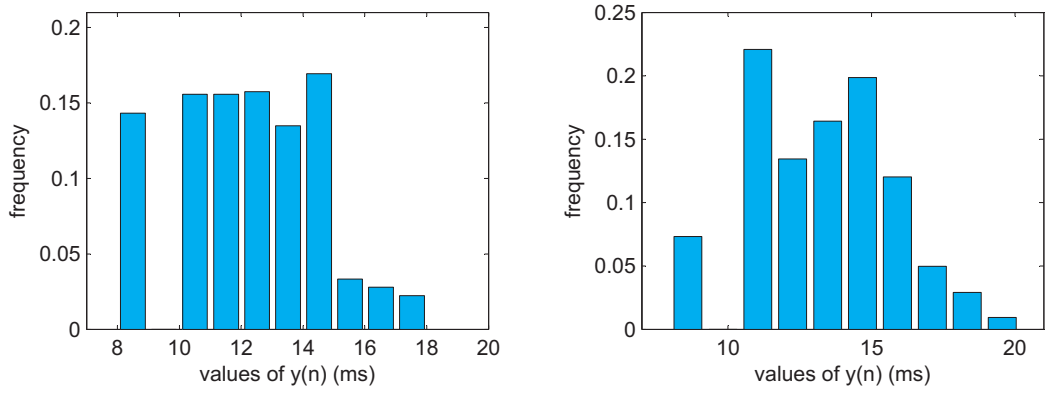

(a) $\bar{r} = 750$ kb/s (b) $\bar{r} = 1$ mb/s

Fig. 30. The histogram of measured inter-arrival times y_n under TCP cross-traffic.

$11.7 - 8 = 3.7$ ms in the first case and $14.5 - 8 = 6.5$ ms in the second one. The two naive estimates of C based on W_n are $\tilde{C} = q/W_n = 1,025$ kb/s and $\tilde{C} = 827$ kb/s, respectively. Likewise, for the TCP case, the measured averages (i.e., 12.2 and 13.3 ms each) of samples y_n lead to incorrect naive estimates $\tilde{C} = 983$ kb/s and $\tilde{C} = 902$ kb/s, respectively.

In order to understand how $\tilde{C}$ and the value of W_n evolve, we run another simulation under 1 mb/s total TCP cross-traffic and plot the evolutions of the absolute error $|\tilde{C} - C|$ and that of W_n in Fig. 31. As Fig. 31(a) shows, the absolute error between C and $\tilde{C}$ converges to a certain value after 5,000 samples y_n, providing a rather poor estimate $\tilde{C} \approx 1,010$ kb/s. Fig. 31(b) illustrates that W_n in fact converges to $\Delta + E[\omega_n]$, where the mean of the noise is $W_n - \Delta \approx 11.9 - 8 = 3.9$ ms.

Previous work [1], [14], [22], [54], [78] focused on identifying the peaks (modes) in the histogram of the collected bandwidth samples and used these peaks to estimate the bandwidth; however, as Figs. 29 and 30 show, this can be misleading when the distribution of the noise is not known a-priori. For example, the tallest peak in Fig. 29(b) is located at 13 ms ($\tilde{C} = 923$ kb/s), which is only a slightly better estimate than 827 kb/s derived from the mean of y_n. Moreover, the tallest peak in Fig. 30(a) is located at 14.5 ms, which leads to a worse estimate $\tilde{C} = 827$ kb/s compared to 983 kb/s computed from the mean of y_n.

To combat these problems, existing studies [1], [14], [22], [54], [78] apply numerous empirical methods to find out which mode is more likely to be correct. This may be the only feasible solution in multi-hop networks; however, one must keep in mind that it is possible that *none* of the modes in the measured histogram corresponds to Δ as evidenced by both graphs in Fig. 29.

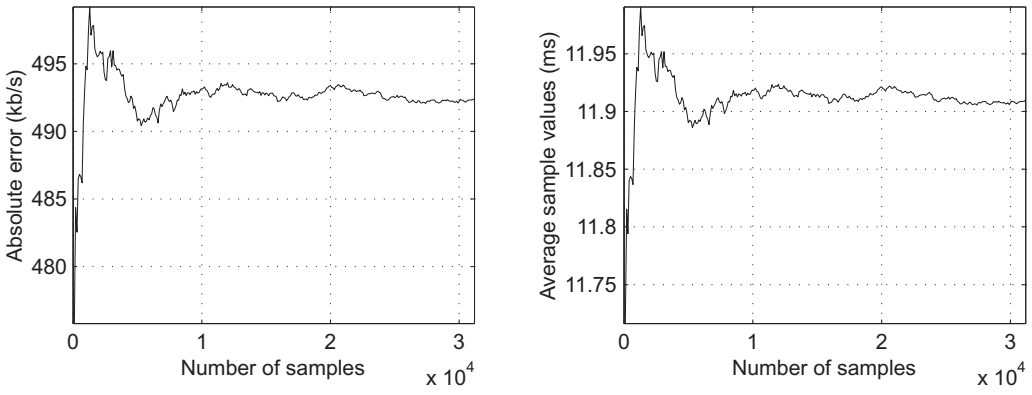

(a) $|\tilde{C} - C|$ (b) W_n

Fig. 31. (a) The absolute error of the packet-pair estimate under TCP cross-traffic of $\bar{r} = 1$ mb/s. (b) Evolution of W_n.

3. Packet-Train Analysis

Another topic of debate in prior work was whether *packet-train* methods offer any benefits over *packet-pair* methods. Some studies suggested that packet-train measurements converge to the *available* bandwidth[3] for sufficiently long bursts of packets [1], [14]; however, no analytical evidence to this effect has been presented so far. Other studies [22] employed packet-train estimates to increase the measurement accuracy of bottleneck bandwidth estimation, but it is not clear how these samples benefit asymptotic convergence of the estimation process.

We consider a hypothetic packet-train method that transmits probe traffic in bursts of k packets and averages the inter-packet arrival delays within each burst to obtain individual samples $\{Z_n^k\}$, where n is the burst number. For example, if $k = 10$, samples $y_2, \ldots, y_{10}$ define Z_1^{10}, samples $y_{12}, \ldots, y_{20}$ define Z_2^{10}, and so on.

[3]Even though this question appears to have been settled in some of the recent papers, we provide additional insight into this issue.

The reason for excluding samples $y_1, y_{n+1}, \ldots, y_{nk+1}$ is because they are based on the leading packets of each burst, which encounter large inter-burst gaps in front of them and do not follow the model developed so far.

In what follows in this section, we derive the distribution of $\{Z_n^k\}$ as $k \to \infty$.

Theorem 10. *For sufficiently large k, constant $x_n = x$, and a regenerative processes $M(t)$, packet-train samples converge to the following Gaussian distribution for large n:*

$$\left\{Z_n^k\right\} \xrightarrow{D} N\Big(\Delta + \frac{\lambda x E[S_j]}{C}, \frac{\lambda x Var\left[S_j - \lambda E[S_j] X_i\right]}{(k-1)C^2}\Big), \tag{108}$$

where $\xrightarrow{D}$ denotes convergence in distribution, $N(\mu, \sigma^2)$ is a Gaussian distribution with mean μ and standard deviation σ, and X_i are inter-packet arrival delays of cross-traffic.

Proof. First, define a k-sample version of the cumulative reward process in (101):

$$V_n^k = \sum_{j=1}^{M(a_{kn}) - M(a_{k(n-1)+1})} S_j, \quad n = 1, 2, \ldots. \tag{109}$$

Process V_n^k is also a counting process, however, its time-scale is measured in bursts instead of packets. Thus, V_n^k determines the amount of cross-traffic data received by the bottleneck link during an entire burst n. Equation (109) shows that Z_n^k can be asymptotically interpreted as the *reward rate* of the reward-renewal process V_n^k:

$$Z_n^k = \Delta + \frac{V_n^k}{(k-1)C}, \tag{110}$$

where $k-1$ is the number of inter-packet gaps in a k-packet train of probe packets. Assuming $M(t)$ is regenerative and for sufficiently large k, we have [102]:

$$Z_n^k = \Delta + \frac{V_1^k}{(k-1)C} + o(1). \tag{111}$$

Applying the regenerative central limit theorem, constraining the rest of the derivations in this section to constant $x_n = x$, and assuming $E[X_i] < \infty$ [102]:

$$\left\{ \frac{V_1^k}{k-1} \right\} \xrightarrow{D} N\Big(\lambda x E[S_j], \frac{\lambda x Var\left[S_j - \lambda E[S_j] X_i\right]}{k-1}\Big). \tag{112}$$

Combining (111) and (112), we get (108). □

First, notice that the mean of this distribution is the same as that of samples $\{y_n\}$ in (107), which, as was intuitively expected, means that both measurement methods have the same expectation. Second, it is also easy to notice that the variance of Z_n^k tends to zero as long as $Var[X_i]$ is finite.

Theorem 11. *If $Var[X_i]$ is finite, the variance of packet-train samples Z_n^k tends to zero for large k.*

Proof. Since λ, x, and $E[S_j]$ are all finite and do not depend on k, using independence of S_j and X_i in (108), we have:

$$Var[Z_n^k] = \frac{\lambda x Var[S_j] + \lambda^3 x E^2[S_j] Var[X_i]}{(k-1)C^2}, \tag{113}$$

which tends to 0 for $k \to \infty$. □

As a result of this phenomenon, longer packet trains will produce narrower distributions centered at $\Delta + E[\omega_n]$. The CBR case already studied in Fig. 29(b) clearly has finite $Var[X_i]$ and therefore samples $\{Z_n^k\}$ must exhibit decaying variance as k increases. One example of this convergence for packet trains with $k = 5$ and $k = 10$ is shown in Fig. 32.

4. Discussion

Now we address several observations of previous work. It is noted in [22] that while packet-pair histograms usually have many different modes, the histogram of packet-

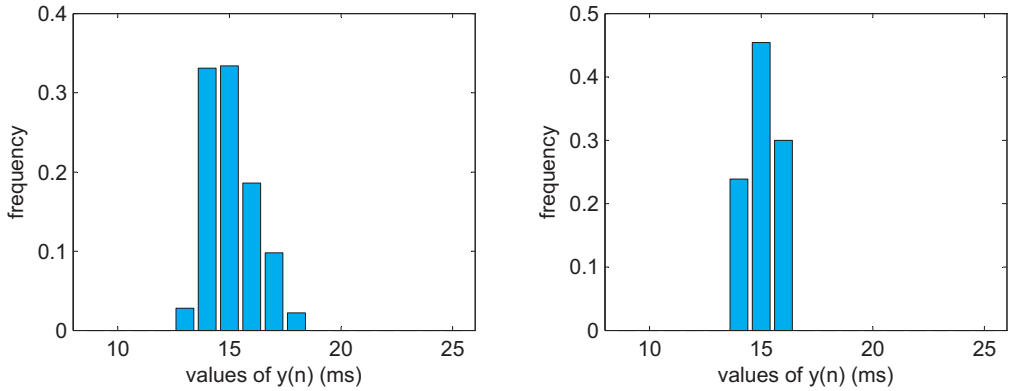

(a) $k = 5$ (b) $k = 10$

Fig. 32. The histogram of measured inter-arrival times Z_n^k based on packet trains and CBR cross-traffic of $\bar{r} = 1.3$ mb/s.

train samples becomes unimodal with increased k. This readily follows from (108) and the Gaussian shape of $\{Z_n^k\}$. Previous papers also noted (e.g., [22]) that as packet-train size k is increased, the distribution of samples $\{Z_n^k\}$ exhibits lower variance. This result follows from the above discussion and (113). Furthermore, [22] found that packet-train histograms for large k tend to a single mode whose location is "independent of burst size k." Our derivations provide an insight into how this process happens and shows the location of this "single mode" to be $\Delta + E[\omega_n]$ in (108).

In summary, packet-train samples $\{Z_n^k\}$ represent a limited reward rate that asymptotically converges to a Gaussian distribution with mean $E[y_n]$. Perhaps it is possible to infer some characteristics of $\{X_i\}$ by observing the variance of $\{Z_n^k\}$ and applying the result in (108); however, since there are several unknown parameters in the formula (such as $Var[X_i]$ and $E[S_j]$), this direction does not lead to any tractable results unless we assume a particular process $M(t)$.

Since $\{Z_n^k\}$ asymptotically tend to a very narrow Gaussian distribution centered

at $\Delta + E[\omega_n]$, we find that there is no evidence that $\{Z_n^k\}$ measure the available bandwidth or offer any additional information about the value of Δ as compared to traditional packet-pair samples $\{y_n\}$.

D. Arbitrary Cross-Traffic

In this section, we relax the stationarity and renewal assumptions about cross-traffic and derive a robust estimator of C and $\bar{r}$. Assume an arbitrary arrival process $r(t)$ for cross-traffic, where $r(t)$ is its instantaneous rate at time t. We impose only one constraint on this process – it must have a finite time average $\bar{r}$ shown in (97). The goal of the sampling process is to determine both C and $\bar{r}$. Since $\bar{r} > C$ imply constant packet loss and zero available bandwidth, we are generally interested in non-trivial cases of $\bar{r} \leq C$. Stochastic process $r(t)$ may be renewal, regenerative, a superposition of ON/OFF sources, self-similar, or otherwise. Furthermore, since packet arrival patterns in the current Internet commonly exhibit non-stationarity (due to day-night cycles, routing changes, link failure, etc.), our assumptions on $r(t)$ allow us to model a wide variety of such non-stationary processes and are much broader than commonly assumed in traffic modeling literature.

Next, notice that if the probing traffic can sample $r(t)$ using a Poisson sequence of probes at times $t_1, t_2, \ldots$, the average of $r(t_i)$ converges to $\bar{r}$ (applying the PASTA principle [102]):

$$\lim_{n\to\infty} \frac{r(t_1) + r(t_2) + ... + r(t_n)}{n} = \lim_{t\to\infty} \frac{1}{t} \int_0^t r(u)du = \bar{r}, \tag{114}$$

as long as delays $\tau_i = t_i - t_{i-1}$ are *i.i.d.* exponential random variables. In order to accomplish this type of sampling, the sender must emit packet-pairs at exponentially distributed intervals. Assuming that the i-th packet-pair arrives to the router at time

t_i, it will sample a small segment of $r(t)$ by allowing g_i amount of data to be queued between the probes:

$$g_i = \int_{t_i}^{t_i+x_i} r(u)du \approx r(t_i)x_i, \tag{115}$$

where x_i is the spacing between the packets in the i-th packet-pair. Again, assuming that y_i is the i-th inter-arrival sample generated by the receiver, we have:

$$y_i = \Delta + \frac{g_i}{C} = \Delta + \frac{r(t_i)x_i}{C}. \tag{116}$$

Finally, fixing the value of $x_i = x$, notice that W_n has a well-defined limit:

$$\lim_{n\to\infty} W_n = \lim_{n\to\infty} \frac{1}{n}\sum_{i=1}^{n}\left(\Delta + \frac{r(t_i)x_i}{C}\right) = \Delta + \frac{x}{C}\lim_{n\to\infty}\sum_{i=1}^{n}\frac{r(t_i)}{n} = \Delta + \frac{x\bar{r}}{C}. \tag{117}$$

In essence, this result[4] is similar to our earlier derivations, except that (117) requires much weaker restrictions on cross-traffic and also shows that a single-node model is completely tractable in the setting of almost arbitrary cross-traffic. We next show how to extract both C and $\bar{r}$ from (117).

1. Capacity

Observe that (117) is a linear function of x, where $\bar{r}$ is the slope and Δ is the intercept[5]. Therefore, by injecting packet-pairs with two different spacings x_a and x_b, one can compute the unknown terms in (117) using two sets of measurements $\{y_i^a\}$ and $\{y_i^b\}$. To accomplish this, define the corresponding average processes to be W_n^a and W_n^b:

$$W_n^a = \frac{1}{n}\sum_{i=1}^{n} y_i^a, \quad W_n^b = \frac{1}{n}\sum_{i=1}^{n} y_i^b. \tag{118}$$

---

[4]A similar formula has been derived in [10], [37], [72] and several other papers under a fluid assumption.

[5]For technical differences between this approach and previous work (such as TOPP [72]), see [60].

The simplest way to obtain both W_n^a and W_n^b using a *single* measurement is to alternate spacing x_a and x_b while preserving the PASTA sampling property. Using a one-bit header field, the receiver can unambiguously sort the inter-arrival delays into two sets $\{y_i^a\}$ and $\{y_i^b\}$, and thus compute their averages in (118).

While samples are being collected, the receiver has two running averages produced by (118). Subtracting W_n^b from W_n^a, we are able to separate $\bar{r}/C$ from Δ:

$$\lim_{n\to\infty}(W_n^a - W_n^b) = \frac{(x_a - x_b)\bar{r}}{C}. \tag{119}$$

Next, denote by $\tilde{\Delta}_n$ the following estimate of Δ at time n:

$$\tilde{\Delta}_n = W_n^a - x_a\frac{W_n^a - W_n^b}{x_a - x_b}. \tag{120}$$

Taking the limit of (120), we have the following result.

Theorem 12. *Assuming a single congested bottleneck for which time-average rate $\bar{r}$ exists, $\tilde{\Delta}_n$ converges to Δ:*

$$\lim_{n\to\infty}\tilde{\Delta}_n = \Delta. \tag{121}$$

Proof. Re-writing (121):

$$\lim_{n\to\infty}\tilde{\Delta}_n = \Delta + \frac{x_a\bar{r}}{C} - x_a\frac{(x_a - x_b)\bar{r}}{C(x_a - x_b)} = \Delta, \tag{122}$$

which is obtained with the help of (117), (119), and (120). □

Our next result shows a more friendly restatement of the previous claim.

Corollary 13. *Assuming a single congested bottleneck for which time-average rate $\bar{r}$ exists, estimate $\tilde{C}_n = q/\tilde{\Delta}_n$ converges to capacity C:*

$$\lim_{n\to\infty}\tilde{C}_n = \lim_{n\to\infty}\frac{q}{W_n^a - x_a\dfrac{W_n^a - W_n^b}{x_a - x_b}} = \lim_{n\to\infty}\frac{q(x_a - x_b)}{x_aW_n^b - x_bW_n^a} = C. \tag{123}$$

2. Available Bandwidth

Notice that knowing an estimate of C in (123) and using $\bar{r}$ in (119), it is easy to estimate the mean rate of cross-traffic:

$$\lim_{n\to\infty} \frac{(W_n^a - W_n^b)\tilde{C}_n}{x_a - x_b} = \bar{r}, \tag{124}$$

which leads to the following result.

Corollary 14. *Assuming a single congested bottleneck for which time-average rate $\bar{r}$ exists, the following converges to the available bandwidth $A = C - \bar{r}$:*

$$\lim_{n\to\infty} q\left(\frac{x_a - x_b - W_n^a + W_n^b}{x_a W_n^b - x_b W_n^a}\right) = C - \bar{r} = A. \tag{125}$$

3. Simulations

We confirm these results and compare our models with several recent methods Spruce [96], IGI [37], and Pathload [44] through `ns2` simulations. Since the main theme of this chapter is bandwidth estimation in heavily-congested routers, we conduct all simulations over a loaded bottleneck link in Fig. 28 with utilization varying between 82% and 92% (the exact value changes depending on C and the interaction of TCP cross-traffic with probe packets). Delays x_a and x_b are set to maintain the desired range of link utilization.

Define $e_A = |\tilde{A} - A|/A$ and $e_C = |\tilde{C} - C|/C$ to be the relative estimation errors of A and C, respectively, where A is the true available bandwidth of a path, $\tilde{A}$ is its estimate using one of the measurement techniques, C is the true bottleneck capacity, and $\tilde{C}$ is its estimate. Table X shows relative estimation errors e_A for Pathload, Spruce, and IGI. For Pathload, we averaged the low and high values of the produced estimates $\tilde{A}$. In the IGI case, we used the estimates available at the end of IGI's internal convergence algorithm. Also note that we fed both Spruce and IGI the

Table X. Available Bandwidth Estimation Error

Bottleneck capacity	Relative error			
C (mb/s)	Model (125)	Pathload	Spruce	IGI
1.5	8.6%	46.5%	27.9%	84.5%
5	8.3%	40.1%	23.4%	90.0%
10	10.1%	40.9%	26.9%	89.0%
15	7.7%	38.5%	24.5%	83.1%

exact bottleneck capacity C, while model (125) and Pathload operated without this information.

As the table shows, Spruce performs better than Pathload in heavily-congested cases, which is expected since it can utilize the known capacity information. Interestingly, however, IGI's estimates are worse than those of Pathload even though IGI utilizes the true capacity C in its estimation algorithm. A similar result is observed in [96] under a relatively small amount of cross-traffic (20% to 40% link utilization).

Next, we examine models (123), (125) with a large number of samples to show their asymptotic convergence and estimation accuracy. We plot the evolution of relative estimation errors e_C and e_A in Fig. 33. As Fig. 33(a) shows, $\tilde{C}$ converges to a value that is very close (within 3%) to the true value of C. In Fig. 33(b), the available bandwidth estimates quickly converge within 10% of A. For the purpose of comparison, we next plot estimation errors e_A produced by Spruce and IGI in Fig. 34. As Fig. 34(a) shows, even with the exact value of C and after 1000 samples, Spruce exhibits an error of 27%. Furthermore, IGI's estimates are much worse than Spruce's as illustrated in Fig. 34(b), which plots the evolution of relative available bandwidth estimation error e_A until IGI's internal algorithm terminates.

Finally, we should note that since both estimates asymptotically converge to their true values, the accuracy of estimation depends on the number of samples y_n

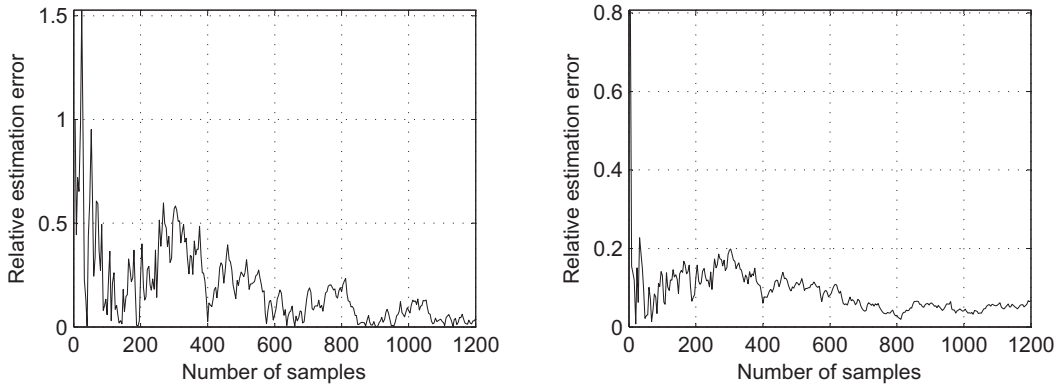

(a) e_C (b) e_A

Fig. 33. Evolution of relative estimation errors e_C and e_A of (123) and (125) over a single congested link with $C = 1.5$ mb/s and 85% link utilization.

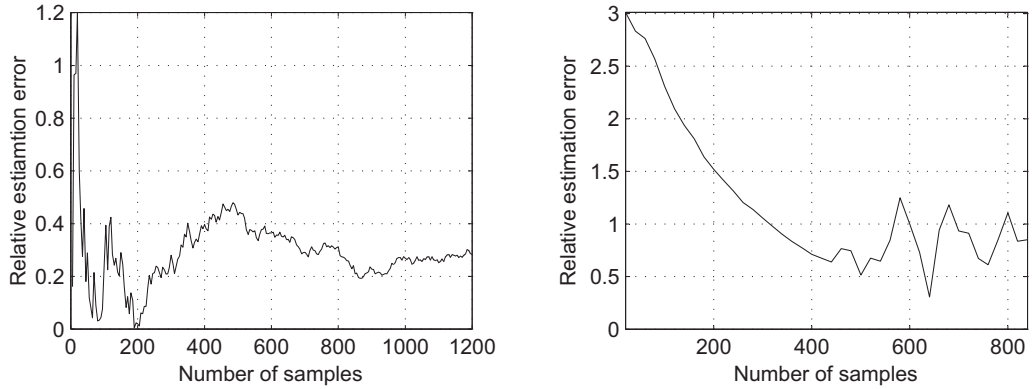

(a) Spruce (b) IGI

Fig. 34. Relative estimation errors e_A produced by Spruce and IGI over a single congested link with $C = 1.5$ mb/s and 85% link utilization.

used. This provides operational flexibility to applications because there exists trade-off between accuracy and time for measurements.

E. Extension to Multiple Links

In this section, we discuss possibility of extension of our single-node model to the case of multiple congested routers and conjecture that such extension may be possible provided that a certain queuing condition of probe packets holds. We start by discussing in the next subsection the case that the probe packets do not queue behind each other at the bottleneck router, which may occur on a path with multiple congested routers.

1. Large Inter-Probe Delays

Consider the original model of a router in (98). This time, assume that *none* of the probe packets queue behind each other at the bottleneck router. This means that packet $n-1$ leaves the router before packet n arrives, which is expected if inter-packet spacing x_n at the source is very large compared to the transmission delay Δ. Under these assumptions, $d_{n-1} < a_n$ and (98) becomes:

$$d_n = a_n + \omega_n + \Delta, \quad n \geq 1. \tag{126}$$

Hence, inter-departure delays y_n are:

$$y_n = a_n - a_{n-1} + \omega_n - \omega_{n-1}, \quad n \geq 2. \tag{127}$$

Notice that the first term $a_n - a_{n-1}$ in (127) is the inter-arrival delay x_n of the probe traffic and the second term $\omega_n - \omega_{n-1}$ can be modeled as some zero-mean random noise. This can be explained intuitively by noticing that under the assumption of large x_n, each router delays probe packets (on average) by the same amount. Then the

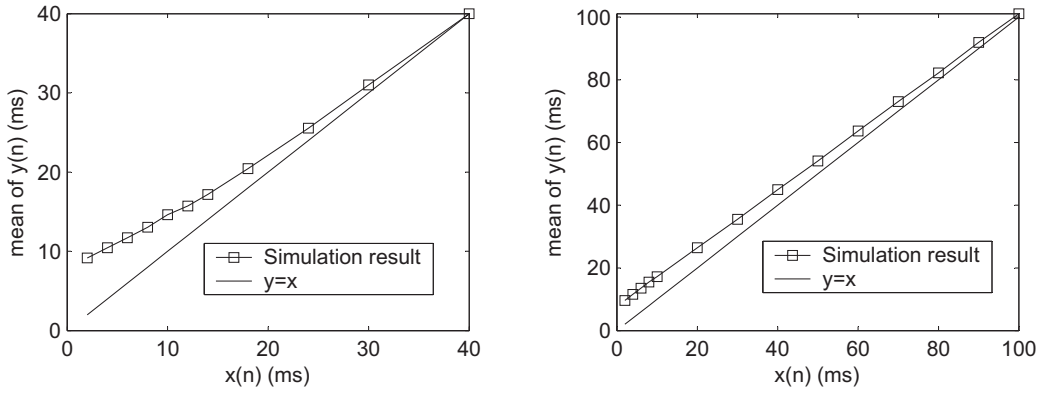

(a) CBR cross-traffic (b) TCP cross-traffic

Fig. 35. Convergence of ω_n to zero-mean additive noise for large x_n under CBR and TCP cross-traffic.

distance between each pair of subsequent packets fluctuates around the mean of x_n. Using an inductive argument, it is also easy to show the following.

Fact 1. *If the initial spacing x_n is larger (in a statistical sense) than queuing delays experienced by packets at each router of an N-hop end-to-end path, the mean of the sampled signal y_n is equal to $E[x_n]$ and the following holds for each router k:*

$$E[\omega_{n,k} - \omega_{n-1,k}] = 0. \tag{128}$$

To confirm that the zero-mean model in (128) holds in practice, we run `ns2` simulations with 85% utilization at the bottleneck link and varying packet sizes of CBR and TCP cross-traffic. The plots of $E[y_n]$ as a function of x_n for different values of $x_n = x$ are shown in Fig. 35. As the two figures show, $E[y_n]$ converges to x_n at 40 and 100 ms, respectively, at which time the noise at the bottleneck router becomes zero-mean-additive. Note that similar results hold for multiple congested routers, different traffic patterns, and different packet sizes. Also note that the point at which $E[y_n]$ converges to x is *not* necessarily the value of the available bandwidth as was

suggested in prior work [37].

2. Recursive Model for Multi-Node Paths

Assuming multiple congested routers along a path, the result in (121) no longer holds. Notice that it is possible to recursively extend the original model in (117) to multiple congested links where the input x_n of each link is the output y_n of the previous link.

Add index k to each process and each random variable to indicate that it is local to router k along the path from the sender to the receiver. Define $x_{i,k}$ to be the inter-packet spacing of two probe packets P_{2i} and P_{2i-1} in a probe-pair i arriving at router R_k and $y_{i,k}$ to be their inter-departure spacing exiting from R_k. Denote by $\omega_{2i,k}$ the random noise introduced to the spacing between P_{2i} and P_{2i-1} by the cross-traffic at R_k. Further denote by $Q_{2i-1,k}$ the queuing delay of the first probe packet P_{2i-1} in the i-th probe-pair inside router R_k and $\phi_{2i,k}$ is some zero-mean noise process of the i-th pair at R_k. Then, we define the following recursive model:

$$y_{i,k} = \begin{cases} \Delta_k + \omega_{2i,k}, & x_{i,k} < Q_{2i-1,k} \\ \Delta_k + \phi_{2i,k}, & x_{i,k} \geq Q_{2i-1,k} \end{cases}, \tag{129}$$

where $\Delta_k = q/C_k$ is the transmission delay of the probe packets over link k (where C_k is the capacity of router R_k).

Notice that inter-arrival spacing $x_{i,k}$ of probe traffic at router R_k simply equals inter-departure delay $y_{i,k-1}$ of the previous router R_{k-1}. Further notice that if inter-arrival spacing $x_{i,k}$ between two packets in a probe-pair i is less than the time that the second probe packet in the pair spends in the buffer, the two packets queue behind each other and follow the model developed earlier in this chapter. When the opposite holds, the packets do not queue behind each other and the router adds *i.i.d.* zero-mean noise $\phi_{2i,k}$ to Δ_k.

F. Measuring Tight-Link Bandwidth over Multi-Hop Paths

Although it appears impossible to completely tract the multi-hop paths due to the stochastic mixture of two types of noise in (129), a recent probing method (called Envelop) aims to measure end-to-end multi-hop paths by achieving the two conditions in (129). This sampling technique sends trains of N probe packets surrounded by two envelope packets along the path in question and allows the probe packets to sample queuing dynamics at the desired router R_k and then "disappear" from the network at router R_{k+1}. If the length of a packet-train is sufficiently large, then the recursive relationship between the average output dispersions $E[y_{i,k}]$ and $E[y_{i,k-1}]$ can be expressed as:

$$E[y_{i,k}] = \begin{cases} E[y_{i,k-1}] & E[y_{i,k-1}] \geq \dfrac{q}{A_k} \\ \dfrac{q + \lambda_k E[y_{i,k-1}]}{C_k} & E[y_{i,k-1}] < \dfrac{q}{A_k} \end{cases}, \tag{130}$$

where C_k and A_k are the respective capacity and available bandwidth of router R_k, q is the size of probing packets, and λ_k is the average arrival rate of cross-traffic entering R_k.

It is easy to see from (130) that a necessary condition for the bandwidth characteristics of link R_k to be measurable is $E[y_{i,k-1}] < q/A_k$. Otherwise, R_k preserves average incoming inter-packet spacings and thus $E[y_{i,k}]$ contains no information about the capacity or available bandwidth of the link. Define R_t to be the tight-link router and A_t to be the tight-link available bandwidth. Then, the above conditions can be summarized as following.

Fact 2. *The tight-link router R_t is always measurable as long as the initial spacing $x < q/A_t$.*

Fact 3. *The mean inter-departure delay $E[y_{i,k}]$ of router R_k is preserved along the*

path suffix from link R_{k+1} up to the receiver, i.e., $E[y_i] = E[y_{i,k}]$, as long as $E[y_{i,k}] > q/A_j$ holds for all $j > k$.

Define $z_{i,k}$ to be the delay between two envelop packets surrounding a probe-train i after the probe-train is dropped at router R_{k+1}. Since we assume that the mean of $z_{i,k}$ is preserved along the path suffix, we have:

$$E[z_{i,k}] = (N+1)E[y_{i,k}]. \tag{131}$$

Define $W_{n,k}$ to be a normalized average of n samples of $z_{i,k}$ (where i is the packet-train sequence number) with respect to a given router R_k:

$$W_{n,k} = \frac{1}{n}\sum_{i=1}^{n}\frac{z_{i,k}}{N+1}. \tag{132}$$

Then, similar to the single-hop case discussed in the first half of this chapter, the capacity and available bandwidth of R_k can be inferred by using two sets of measurements $\{z^a_{i,k}\}$ and $\{z^b_{i,k}\}$ with two different initial inter-packet spacings $x = x_a$ and $x = x_b$ and computing the corresponding metrics $W^a_{n,k}$ and $W^b_{n,k}$ at the receiver:

$$W^a_{n,k} = \frac{1}{n}\sum_{i=1}^{n}\frac{z^a_{i,k}}{N+1}, \quad W^b_{n,k} = \frac{1}{n}\sum_{i=1}^{n}\frac{z^b_{i,k}}{N+1}. \tag{133}$$

Similar to (123) and (125), the receiver (whenever feasible) is able to extract available bandwidth A_k and capacity C_k from $E[z_{i,k}]$:

$$\lim_{n\to\infty}\frac{q(W^a_{n,k-1} - W^b_{n,k-1})}{W^a_{n,k-1}W^b_{n,k} - W^b_{n,k-1}W^a_{n,k}} = C_k \tag{134}$$

$$\lim_{n\to\infty} q\left(\frac{W^a_{n,k-1} - W^b_{n,k-1} - W^a_{n,k} + W^b_{n,k}}{W^a_{n,k-1}W^b_{n,k} - W^b_{n,k-1}W^a_{n,k}}\right) = A_k \tag{135}$$

Now, the remaining question is how to select probing parameters to ensure that spacing $z_{i,k}$ between the surviving envelope packets at router R_k is sufficiently large,

while minimizing probing overhead as much as possible and maximizing the number of links measurable. We address this by developing a measurement tool by adaptively selecting various probing parameters based on different path conditions.

1. Probing Parameters in Envelope

The main idea behind Envelope is to preserve the inter-departure spacing $y_{i,k}$ of probe packets in the path suffix of a congested router R_k using envelope packets. As suggested in Section E, maintaining a large inter-envelope packet spacing $z_{i,k}$ preserves its mean $E[z_{i,k}]$ in the path suffix since cross-traffic noise introduced into $z_{i,k}$ becomes zero-mean. Note that spacing $z_{i,k}$ depends on the capacity of routers R_j $(j \leq k)$, amount of cross-traffic interfering with probe packets at R_j, initial input spacing x, and probe-train length N. Since only x and N can be controlled by the Envelope source, proper selection of N and x is important in producing sufficiently large $z_{i,k}$ (manual selection of such parameters which is done by the previous work cannot determine optimal values of N and x under dynamically changing network conditions).

Hence, in the following subsections, we investigate a method that automatically selects these parameters in practice such that $E[z_{i,k}]$ is preserved through the path suffix after the tight link. We start by discussing two initial input spacings $x = x_a$ and $x = x_b$ and how Envelope chooses them.

a. Initial Input Spacing

Recall from Fact 2 that as long as the two spacings are less than q/A_t and differ from each other, the tight link can be measured. Note that Envelope can also measure many non-tight links if the conditions in Facts 2 and 3 hold. Hence, it makes sense to choose at least one initial spacing that is much smaller than q/A_t. To achieve

this, Envelope utilizes known access link capacity C_0 and sets x_a as small as possible: $x_a = q/C_0$. Then, it probes for the Asymptotic Dispersion Rate (ADR) [21] of the path to determine x_b. Envelope obtains ADR by sending a packet-train with spacing x_a and computes $ADR = q/E[y_i]$ at the receiver, which is similar to Pathrate. Envelope determines the second spacing using $x_b = q/ADR$. It is proved in [21] that $A_t < ADR < C_0$, which confirms that our initial spacing settings satisfy the condition in Fact 2.

b. Probe-Train Length

With x_a and x_b in hands, our next question is how to select N for a particular path under investigation. Recall that to preserve $E[z_{i,k}]$, the rate (i.e., $q/z_{i,k}$) of Envelope packets departing from the router R_{k+1} must be slower than any of the available bandwidth of the links on the path suffix. Re-writing this condition, we have:

$$z_{i,k} \geq \frac{q}{\min_{j>k+1}(A_j)}. \tag{136}$$

Substituting $z_{i,k} = (N+1)y_{i,k}$ in (136) and re-arranging terms, we get a theoretical lower bound for N that satisfies the condition in Fact 3:

$$N \geq \frac{q}{y_{i,k} \min_{j>k+1}(A_j)} - 1. \tag{137}$$

Observe from (137) that it is not possible to directly compute the right-side term in the equation since $y_{i,k}$ and A_j are unknown. This leads us to investigating an empirical method, which iteratively probes for N that satisfies (137).

c. Algorithm

We now introduce a selection algorithm that chooses a probe-train length N using spacings $x_a = q/C_0$ and $x_b = q/ADR$ discussed above as input parameters. Since

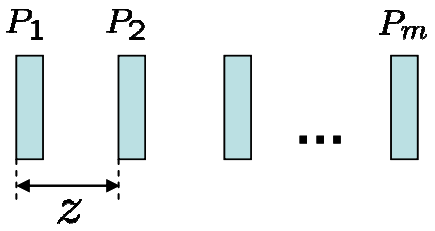

Fig. 36. A probe-train of m packets that is used for parameter tuning.

Envelope requires $x_a \neq x_b$, it chooses two values N_a and N_b for the train length N in order to sample cross-traffic statistics with two different time spans $x_a N_a$ and $x_b N_b$ at routers along the path. Intuitively, cross-traffic arriving over a time interval $x_a N$ or $x_b N$ is more bursty for smaller N. Hence, we can sample cross-traffic statistics more accurately with larger time spans (using large N_a and N_b). However, since measurement overhead also increases with N, it is preferable to keep N as small as possible. Based on the above discussion and the trade-off between accuracy and overhead, we develop an automated algorithm that selects $N = N_a$ and $N = N_b$, each of which is large enough to preserve the mean of inter-envelope packet spacings, while minimizing measurement overhead under various network path conditions.

Define N_l and N_h to be a minimum and maximum train lengths, respectively. Further define σ to be a certain threshold that is adjustable between zero and one. Our parameter tuning procedure (Algorithm 1) includes two subroutines called adjust-spacing (Algorithm 2) and binary-tuning (Algorithm 3), where the former searches for the smallest value of x_a that satisfies the mean preservation condition for the given maximum train length N_h and the latter optimizes the train length N for selected initial input spacings x_a and x_b. Both sub-procedures include an additional subroutine called probe-run (Algorithm 4), which tests if a particular input spacing $z = xN$ is preserved in the path by sending to the receiver a train of m probe packets $P_1, P_2, \ldots, P_m$ (1500 bytes each) with inter-packet spacing z as shown in Fig. 36.

Algorithm 1 Parameter tuning

1: $x_a \leftarrow q/C_0$, $x_b \leftarrow q/ADR$
2: $x_a \leftarrow$ adjust-spacing(x_a, N_h)
3: $N_a \leftarrow$ binary-tuning(N_l, N_h, x_a)
4: $N_b \leftarrow$ binary-tuning(N_l, N_a, x_b)

Algorithm 2 adjust-spacing(x, N)

1: **while** probe-run$(x, N) = true$ **do**
2: $x \leftarrow 2x$
3: **if** $x \geq x_b/\beta$ **then**
4: notify to the user that $N = N_h$ is too small and stop
5: **end if**
6: **end while**
7: **return** x

To assess the preservation of input spacing z, the probe-run procedure computes the following relative error metric e_z:

$$e_z = \frac{|z - \bar{z}|}{z}, \tag{138}$$

where $\bar{z}$ represents an m-sample average of output inter-packet spacings sampled at the receiver. When $e_z > \sigma$, the routine returns true; otherwise, it returns false. Note that if more than the half of probe packets in a probe-train are lost, then the receiver discards that probe train (this implementation details are not shown in the algorithms).

The parameter selection procedure (Algorithm 1) operates as follows. If input spacing $z = qN_h/C_0$ is not preserved in the path, Envelope keeps doubling x_a until the input spacing is preserved or x_a reaches a certain fraction of q/ADR (step 2). When Envelope finds x_a that satisfies the preservation for $N = N_h$, it probes for an optimal value of N_a with current x_a using a binary search (step 3). Thereafter, Envelope repeats the binary search in step 4 to determine an optimal value for N_b. Note that in step 2, the probe-run subroutine is repeatedly used for parameter optimization and

Algorithm 3 binary-tuning($low, high, x$)

1: **while** $high - low \geq 2$ **do**
2: $middle \leftarrow (low + high)/2$
3: **if** probe-run($x, middle$) $= false$ **then**
4: $high \leftarrow middle$
5: **else**
6: $low \leftarrow middle$
7: **end if**
8: **end while**
9: **return** $high$

Algorithm 4 probe-run(x, N)

1: $z \leftarrow xN$
2: Send a packet train of m probe packets with inter-packet spacing z
3: compute $e_z = |z - \bar{z}|/z$
4: **if** $e_z > \sigma$ **then**
5: **return** $true$
6: **else**
7: **return** $false$
8: **end if**

the threshold value σ provides a criterion that represents how well the input spacing is preserved in the path. Hence, large σ requires less iteration of the probe-run, but leads to coarse selection of x_a.

It is worth noting that the automated parameter selection method does not impose much overhead on Envelope's bandwidth estimation. Observe in the algorithm that steps $2-4$ need to iterate the probe-run. Since x_a increases by a factor of 2 when preservation of an input spacing is not satisfied (i.e., $e_z > \sigma$), step 2 is repeated at most $\lfloor \log_2(q/(\beta ADR) - q/C_0) \rfloor$ times. Similarly, it is required to execute the probe-run no more than $\lfloor \log_2(N_h - N_l) \rfloor$ times in optimizing N_a (step 3) and $\lfloor \log_2(N_a - N_l) \rfloor$ times when working on N_b (step 4).

For all simulations in Section F.2, we use $\sigma = 0.05$, $m = 12$, and $\beta = 2$. We also use two configurations for the minimum and maximum train lengths $[N_l, N_h] = [10, 50]$ and $[5, 15]$. With these parameter configurations, the overall delay D of the automated

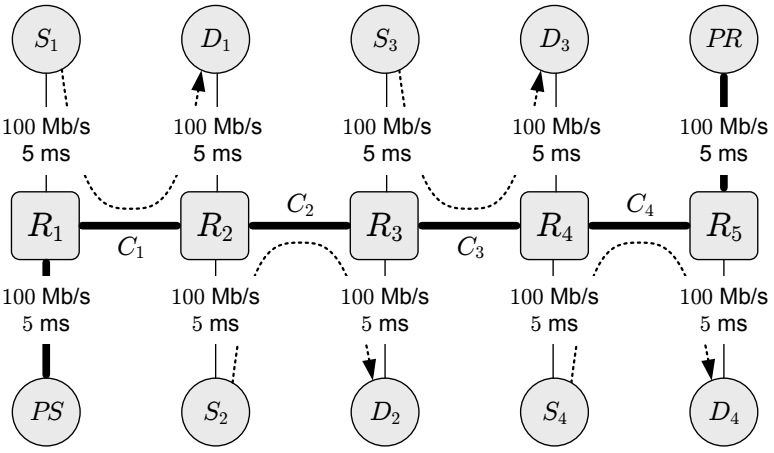

Fig. 37. Simulation topology.

parameter tuning is no more than 5 seconds under various network conditions studied in this chapter (see Tables XI – XIV for details). Note that the parameter selection procedure can accept values for the minimum and maximum train lengths N_l and N_h as an input, which allows users to decide the tradeoff between measurement overhead and estimation accuracy.

2. Performance of Envelope

To evaluate the performance of Envelope, we use simulations to measure estimation accuracy and asymptotic behavior and then compare these results with those in existing methods. We start by describing the simulation setup.

a. Simulation Setup

For simulations, we use the `ns2` network simulator [73] with the topology shown in Fig. 37, in which source PS sends probe data to the destination PR through five router nodes $R_1, \ldots, R_5$. Cross-traffic is injected into each router R_i (where $i = 1, 2, 3, 4$) at an average rate λ_i through nodes S_i ($i = 1, 2, 3, 4$). The speed of all access links is

Table XI. Simulation Setup

	Different link bandwidths (Mb/s)							
	C_1	A_1	C_2	A_2	C_3	A_3	C_4	A_4
Case-I	{[50]	40}	100	50	100	60	70	50
Case-II	[50]	35	100	60	100	70	{60	30}
Case-III	2	0.4	{1.5	0.25}	[0.8]	0.4	1.5	0.35
Case-IV	{[1.5]	0.3}	100	50	100	40	5	1
Case-V	20	4	{15	2.5}	[8]	4	15	3.5
Case-VI	[2]	1	100	50	100	40	{4	0.8}
Case-VII	2	0.4	[0.8]	0.4	{1.5	0.25}	2	0.4

100 Mb/s (delay 5 ms) and the remaining links L_i ($i = 1, 2, 3, 4$) between routers R_i and R_{i+1} have capacities C_i and propagation delay 10 ms.

To examine the estimation accuracy of Envelope, we use seven different network settings shown in Table XI, which lists the capacity and available bandwidth of each link for different simulation scenarios. The values in braces in each row represent the tight-link capacity and available bandwidth of the path for each case. The values in square brackets represent the capacity of narrow link (i.e., bottleneck bandwidth) for each case. Notice from the table that the simulation settings cover all possible relationships between the location of the tight link and narrow link. For instance, in cases I and IV, the narrow link *coincides* with the tight link; in cases III and V, the narrow link *follows* the tight link; while in cases II, VI, and VII, the narrow link *precedes* the tight link.

All simulations are partitioned into two categories: CBR and TCP cross-traffic. For the former scenario, 100 UDP sources are attached to each node S_i to generate CBR flows that are injected into each router R_i. Each CBR flow starts with a random initial delay (between 0 and 15 seconds) and uses 200 or 500-byte packets (half of the

CBR flows uses 200-byte packets, while the other half employs 500-byte packets)[6]. For simulations with TCP cross-traffic, we attach 100 FTP sources to each of S_i and keep the utilization of each router R_i according to the values shown in Table XI. To maintain a fixed average utilization at each link in the TCP scenario, we place an additional router (not shown in the figure) between each node S_i and router R_i to limit the aggregate sending rate of the TCP flows to the capacity of the additional router. The utilization of R_i is controlled by properly setting the capacity of the auxiliary router. TCP cross-traffic consists of a mixture of flows with packet sizes 40, 572, and 1500 bytes, which are selected according to several measurement studies [30], [99] that demonstrate that Internet packet sizes exhibit a trimodal distribution.

In both TCP and UDP scenarios, link utilization along the path of probe packets varies between 20% and 50% for cases I and II (mild-load traffic scenarios) and between 50% and 83% for cases III – VII (heavy-load traffic scenarios).

Under this setup, the probe-traffic source PS starts at 60 seconds and sends trains with 1500-byte packets to measure the path. We use fixed delay between two probe trains instead of using exponentially distributed delay since the benefit of Poisson sampling over fixed-interval sampling is marginal [4]. To avoid congesting the network, Envelope uses low average probing rates for each path depending on measured ADR. Specifically, Envelope sets its probing rate to 50 kb/s for a path with $ADR < 1$ Mb/s, 100 kb/s with $1 < ADR \leq 5$ Mb/s, 250 kb/s for $5 < ADR \leq 10$ Mb/s, and 500 kb/s for $ADR > 10$ Mb/s. Lengths N_a and N_b of alternate packet-trains and inter-packet spacings x_a and x_b are automatically selected as discussed in the previous section.

Note that every simulation has four phases, one for each link in Fig. 37. In each

[6]We remind that the aggregated cross-traffic that actually traverses each router is not CBR, but an aggregation of CBR flows with rather bursty characteristics.

phase ϕ_k $(k = 1, 2, 3, 4)$, the packet-trains enclosed by envelope-packets are dropped at router R_{k+1}, while the two envelope packets are forwarded up to the receiver. In each phase, the receiver PR computes the average spacing $W^a_{n,k}$ and $W^b_{n,k}$ after receiving $n = 50$ packet-trains for each spacing x_a and x_b. The two average spacings are then applied to (134) and (135) to produce estimates of capacity and available bandwidth of the router under investigation.

3. Estimation Accuracy of Envelope

We next investigate estimation accuracy of Envelope, and convergence behavior. We first define the following relative error metrics:

$$e_{C_i} = \frac{|C_i - \tilde{C}_i|}{C_i}, \quad e_{A_i} = \frac{|A_i - \tilde{A}_i|}{A_i}, \tag{139}$$

where C_i is the true capacity of a link L_i, $\tilde{C}_i$ is its estimate, A_i is the true available bandwidth of L_i, and $\tilde{A}_i$ is its estimate. Similarly, define e_C and e_A to be the respective relative estimation errors of capacity and available bandwidth of the tight link L_t of the path:

$$e_C = \frac{|C_t - \tilde{C}_t|}{C_t}, \quad e_A = \frac{|A_t - \tilde{A}_t|}{A_t}, \tag{140}$$

where C_t is the true capacity of the tight link L_t, $\tilde{C}_t$ is its estimate, A_t is the true available bandwidth of L_t, and $\tilde{A}_t$ is its estimate.

Simulation results of Envelope are summarized in Tables XII and XIII, which show relative estimation errors e_{C_i} and e_{A_i} under CBR and TCP cross-traffic, respectively. For these results, we conduct simulations with the minimum and maximum train lengths $N_l = 10$ and $N_h = 50$. In the tables, parameter values selected automatically by Envelope are shown in rows $11 - 14$ and combined delays for parameter tuning are given in rows 15. Empty cells represent links that are not measurable

Table XII. Performance of Envelope under CBR Cross-Traffic ($N_l = 10$, $N_h = 50$)

Metrics	Evaluation scenarios						
	Case-I	Case-II	Case-III	Case-IV	Case-V	Case-VI	Case-VII
e_{C_1}	0.88%	0.09%	0.11%	0.17%	0.006%	0.23%	0.45%
e_{A_1}	0.24%	0.9%	0.67%	1.36%	0.52%	0.11%	0.64%
e_{C_2}	−−	−−	0.2%	−−	0.7%	−−	0.14%
e_{A_2}	−−	−−	0.82%	−−	0.75%	−−	0.26%
e_{C_3}	−−	−−	0.12%	−−	0.2%	−−	0.41%
e_{A_3}	−−	−−	0.54%	−−	0.6%	−−	0.44%
e_{C_4}	−−	1.55%	0.94%	−−	0.9%	0.35%	−−
e_{A_4}	−−	0.08%	0.08%	−−	0.33%	0.28%	−−
N_a	12	12	37	33	30	50	38
N_b	11	11	11	12	12	12	11
x_a (ms)	0.12	0.12	0.96	0.96	0.12	0.48	0.96
x_b (ms)	0.26	0.33	24.5	8.88	2.49	7.81	24.35
D (sec)	1	1	5	4	2	3	5

Table XIII. Performance of Envelope under TCP Cross-Traffic ($N_l = 10$, $N_h = 50$)

Metrics	Evaluation scenarios						
	Case-I	Case-II	Case-III	Case-IV	Case-V	Case-VI	Case-VII
e_{C_1}	1.86%	3.09%	1.22%	0.21%	0.83%	0.19%	0.79%
e_{A_1}	1.33%	3.8%	1.41%	3.22%	0.77%	0.08%	2.05%
e_{C_2}	−−	−−	0.76%	−−	1.24%	−−	0.04%
e_{A_2}	−−	−−	2.29%	−−	0.34%	−−	0.06%
e_{C_3}	−−	−−	1.13%	−−	1.11%	−−	0.74%
e_{A_3}	−−	−−	1.57%	−−	1.45%	−−	0.97%
e_{C_4}	−−	0.11%	1.46%	−−	0.52%	1.15%	−−
e_{A_4}	−−	0.69%	1.31%	−−	1.52%	2.9%	−−
N_a	12	12	35	32	30	25	38
N_b	11	11	11	12	12	11	11
x_a (ms)	0.12	0.12	0.96	0.96	0.12	0.48	0.96
x_b (ms)	0.26	0.34	24.58	8.86	2.47	7.75	24.04
D (sec)	1	1	5	3	2	3	5

Table XIV. Performance of Envelope under TCP Cross-Traffic ($N_l = 5$, $N_h = 15$)

Metrics	Evaluation scenarios						
	Case-I	Case-II	Case-III	Case-IV	Case-V	Case-VI	Case-VII
e_{C_1}	2.45%	1.63%	1.54%	0.66%	0.6%	0.13%	3.28%
e_{A_1}	0.05%	7.46%	5.93%	3.13%	0.64%	0.04%	0.63%
e_{C_2}	−−	−−	0.18%	−−	2.87%	−−	0.27%
e_{A_2}	−−	−−	2.69%	−−	6.34%	−−	0.61%
e_{C_3}	−−	−−	2.25%	−−	0.39%	−−	6.32%
e_{A_3}	−−	−−	3.88%	−−	2.66%	−−	4.74%
e_{C_4}	−−	6.59%	10.9%	−−	1.97%	1.11%	−−
e_{A_4}	−−	1.95%	7.31%	−−	2.07%	0.83%	−−
N_a	7	7	8	8	13	13	10
N_b	6	6	6	6	7	7	7
x_a (ms)	0.12	0.12	3.84	3.84	0.24	0.96	3.84
x_b (ms)	0.26	0.34	24.58	8.86	2.47	7.75	24.04
D (sec)	1	1	3	3	1	2	3

by Envelope. Note that Envelope's parameter tuning overhead is not significant for various network settings shown in table XI and is no more than 5 seconds in the worst case. As Table XII shows, under CBR cross-traffic, Envelope estimates both capacity and available bandwidth of the tight link (shaded in the table) with over 98% accuracy for all cases studied in this chapter. Under TCP cross-traffic, Envelope also produces the tight-link bandwidth estimates $\tilde{C}$ and $\tilde{A}$ with over 96% accuracy as shown in Table XIII.

We also perform simulations with lower values of $N_l = 5$ and $N_h = 15$ under TCP cross-traffic and show its results in Table XIV. As the table shows, Envelope uses considerably smaller values for the probe-train lengths N_a and N_b compared to simulations with higher $N_l = 10$ and $N_h = 50$. For instance, in case VII, Envelope reduces N_a by 78% and N_b by 45%. Note, however, that even with much smaller N_a and N_b Envelope does not significantly sacrifice estimation accuracy and both

capacity and available bandwidth of the tight link are estimated with $93\% - 99\%$ accuracy for all studied cases.

4. Performance Comparison

In this subsection, we compare Envelope with several existing available bandwidth estimators (Pathload [44], Spruce [96], and IGI [37]) and capacity estimation tools (Pathrate [21] and CapProbe [49]) with respect to estimation accuracy using the setup shown in Table XI. For Pathload, IGI, and CapProbe, we use the `ns2` modules that were obtained from the authors, while for Spruce and Pathrate, we converted corresponding UNIX software publicly available into `ns2` code.

a. Available Bandwidth Comparison

We first compare Envelope with Pathload, Spruce, and IGI. For this purpose, we conduct all simulations under both mild-load (cases I and II) and heavy-load (cases III – VII) traffic conditions. Note that with negligible cross-traffic interference at non-tight links, all methods produce very accurate estimates of available bandwidth (we do not show this result in the thesis for brevity). However, when cross-traffic is non-negligible, the estimation accuracy is drastically different depending on the applied methods.

Tables XV and XVI show relative estimation errors e_A for the different cases under CBR and TCP cross-traffic, respectively. For Pathload, we use up to 15600 samples with a very fine-grained bandwidth resolution of 50 kb/s and average the low and high values of the produced estimates[7]. For Spruce, we obtain up to 2000

[7]Recall that Pathload normally exhibits better estimation accuracy with smaller bandwidth resolution, but its internal algorithm requires more samples and time to converge.

Table XV. Available Bandwidth Estimation Methods (CBR Cross-Traffic)

	Relative estimation error e_A			
	Envelope	Pathload	Spruce	IGI
Case-I	0.24%	1%	0.04%	0.44%
Case-II	0.08%	1.66%	15.4%	19.84%
Case-III	0.82%	1.4%	65.07%	62.31%
Case-IV	1.36%	2.52%	1.63%	53.73%
Case-V	0.75%	3.12%	67.51%	68.04%
Case-VI	0.28%	1.12%	22.66%	44.24%
Case-VII	0.44%	1.28%	67.84%	72.07%

Table XVI. Available Bandwidth Estimation Methods (TCP Cross-Traffic)

	Relative estimation error e_A			
	Envelope	Pathload	Spruce	IGI
Case-I	1.33%	1.25%	2.47%	13.7%
Case-II	0.69%	2.56%	14.5%	4.09%
Case-III	2.29%	11.31%	68.07%	61.7%
Case-IV	3.22%	2.53%	27.56%	237%
Case-V	0.34%	6.64%	71.17%	74.28%
Case-VI	2.9%	1.12%	9.9%	47.25%
Case-VII	0.97%	17.98%	82.82%	55.23%

packet-pair samples (over 1200 seconds of simulation time) and then use the last 100 sample average to obtain the main estimate as suggested in [96]. In the IGI case, we use the estimates available at the end of IGI's internal convergence algorithm. Also note that we feed both Spruce and IGI the *exact* bottleneck capacity C, while Envelope and Pathload operate without this information.

As both tables show, when paths are mildly utilized (cases I and II), all methods including Spruce and IGI produce bandwidth estimates within 20% of their true values. Note, however, that in heavy-load scenarios (cases III–VII), Envelope significantly outperforms Spruce and IGI. Further note that Pathload also produces much

Table XVII. Capacity Estimation Methods (CBR Cross-Traffic)

	Relative estimation error e_C		
	Envelope	CapProbe	Pathrate
Case-I	0.88%	11.02%	4.15%
Case-II	0.09%	4%	25.15%
Case-III	0.12%	37.5%	38.82%
Case-IV	0.17%	11.11%	10%
Case-V	0.2%	48.27%	38.84%
Case-VI	0.23%	20%	19.98%
Case-VII	0.14%	40.73%	38%

more accurate bandwidth estimates than Spruce and IGI and its results are comparable to those of Envelope (although Envelope exhibits much better accuracy than Pathload in cases III and VII under TCP cross-traffic).

b. Bottleneck Bandwidth Comparison

Since in all seven path configurations simulated, the narrow link is measurable, we next compare Envelope with recent bottleneck bandwidth estimators CapProbe and Pathrate, both of which provide very accurate capacity estimates in lightly congested paths. For CapProbe [49], we use 100 packet-pair samples for estimation as suggested in the paper. In Pathrate, the internal algorithm executes for over 1800 seconds and uses up to 28440 samples to get estimates of the bottleneck capacity of the end-to-end path.

Tables XVII and XVIII respectively illustrate relative capacity estimation errors e_C of the different methods under CBR and TCP cross-traffic. Even though CapProbe shows very accurate results in cases I and II under TCP cross-traffic, in all other cases Envelope produces significantly better capacity estimates than CapProbe. Envelope also outperforms Pathrate in most simulated cases.

Table XVIII. Capacity Estimation Methods (TCP Cross-Traffic)

	Relative estimation error e_C		
	Envelope	CapProbe	Pathrate
Case-I	1.86%	0%	34.51%
Case-II	3.09%	0%	4.03%
Case-III	1.13%	34.78%	7.46%
Case-IV	0.21%	15.94%	14.86%
Case-V	1.11%	34.78%	7.47%
Case-VI	0.19%	30.43%	32.37%
Case-VII	0.04%	47.36%	13.45%

G. Analysis of Existing Methods

In this section, we examine bandwidth sampling techniques used in several existing methods (Spruce, IGI, and CapProbe) and understand the reasons for their estimation inaccuracy.

1. Spruce and IGI

Note that even with the exact bottleneck capacity information, Spruce and IGI produce estimates with very high relative errors when link utilization is high (see Tables XV and XVI). Recall that Spruce is based on the probe gap model (PGM) [96], which is derived under the assumption of a single bottleneck link that is both the narrow and the tight link along the path. By measuring packet spacing at the receiver, Spruce collects individual samples A_i [96]:

$$A_i = C\left(1 - \frac{y_i - x}{x}\right), \tag{141}$$

where x is the initial inter-packet spacing at the sender and y_i is the i-th measured packet spacing at the receiver. The algorithm averages samples A_i to obtain a running estimate of the available bandwidth $A_n = \sum_{i=1}^{n} A_i/n$.

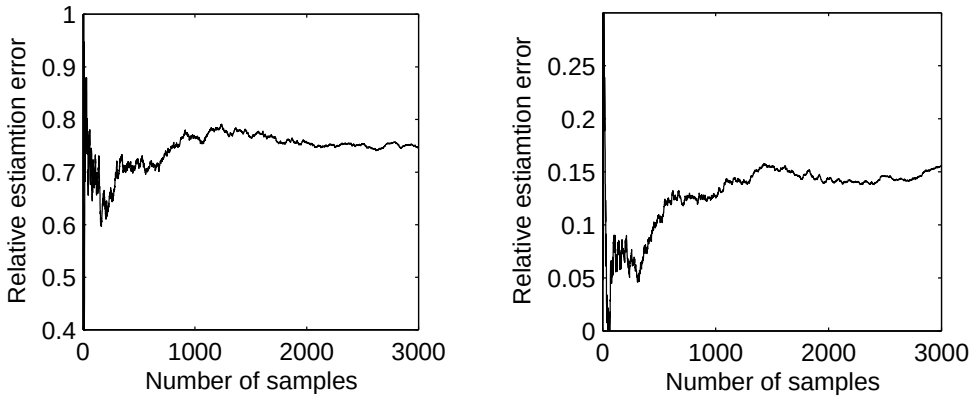

(a) $\rho = 70\%$ (b) $\rho = 30\%$

Fig. 38. Evolution of relative available bandwidth estimation error e_A of Spruce for different values of link utilization ρ in case VII.

Note that this method does not take into account interference of cross-traffic with the probe-gap at the routers other than the bottleneck router over the entire path. Hence, with congested pre- and post-bottleneck links, Spruce's estimation accuracy degrades significantly. For example, in cases III, V, and VII, the estimation error is over $60 - 80\%$ as shown in Tables XV and XVI. To illustrate the estimation accuracy of Spruce for different values of link utilization ρ, we extract the evolution of Spruce's estimate A_n in case VII with TCP cross-traffic. For this demonstration, we set the utilization of all links in the path to ρ and plot the relative estimation errors $e_A = |A - A_n|/A$ for $\rho = 70\%$ and $\rho = 30\%$ in Fig. 38. As the figures show, the convergence error of e_A is reduced from 73% to 16% when ρ is lowered from 70% to 30%. This explains Spruce's high estimation errors in Tables XV – XVI and confirms the method's limitation in heavily-loaded multi-link paths.

IGI [37] is also based on a probing gap model. IGI sends a sequence of packet-trains with increasing inter-packet spacing in each subsequent packet-train until it reaches the *turning point* (where the initial inter-packet spacing x at the sender equals

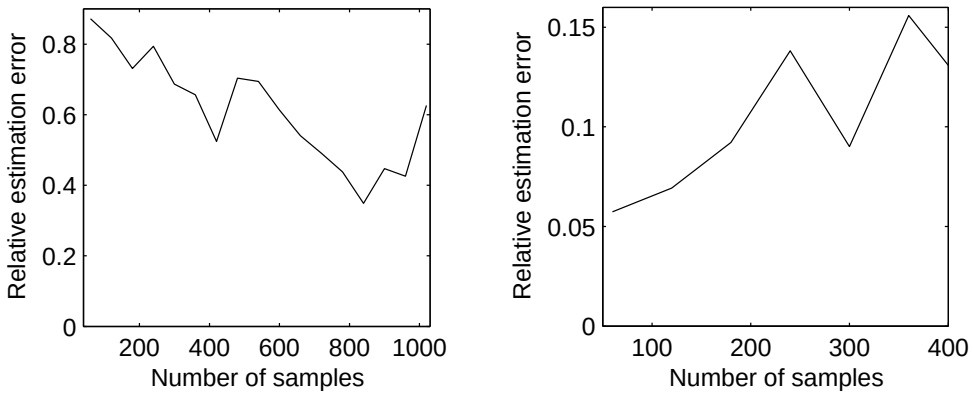

(a) $\rho = 70\%$ (b) $\rho = 30\%$

Fig. 39. Evolution of relative available bandwidth estimation error e_A of IGI for different values of link utilization ρ. In both cases, the IGI algorithm stops at $E[y_i] = 1.1x$.

the average output inter-packet spacing $E[y_i]$ sampled at the receiver). This method assumes that at the turning point, the noise introduced by cross-traffic becomes zero mean and the probing rate is equal to the available bandwidth of the path (which is incidentally not true, see [61] for details). Furthermore, the analysis in [37] with respect to a single congested node does not consider the interference of pre- and post-bottleneck cross-traffic, which randomly changes the probe-gap at the receiver. As a result, IGI's estimate can converge to a value that is significantly different from the true path available bandwidth (see Tables XV – XVI).

To emphasize this fact, we simulate case VII with TCP cross-traffic for two different utilizations $\rho = 70\%$ and $\rho = 30\%$. We plot in Fig. 39 the evolution of relative estimation error e_A until IGI's internal algorithm terminates. For this illustration, we let the IGI algorithm terminate when $E[y_i]$ reaches within 10% (i.e., $E[y_i] = 1.1x$) of the value at the turning point. As the figure shows, IGI produces the available bandwidth estimate with 63% error in the heavily congested case, while the same error is only 12% in the lightly congested case. Note from the figure that IGI's

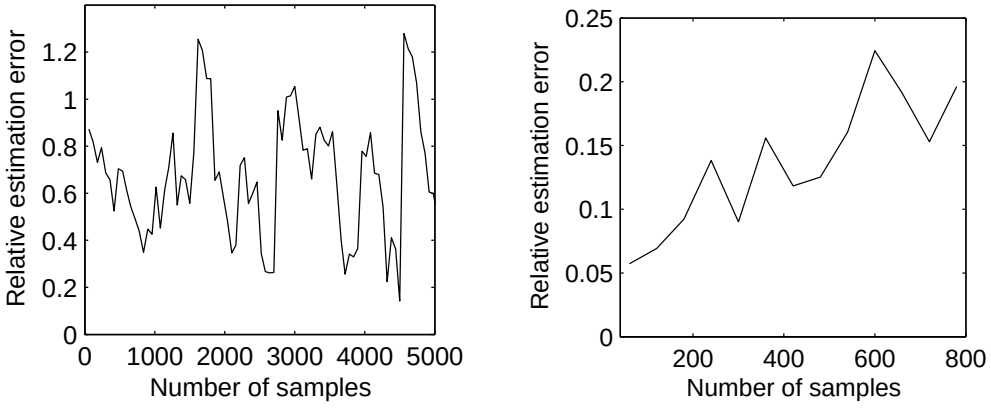

(a) $\rho = 70\%$ (b) $\rho = 30\%$

Fig. 40. Evolution of relative available bandwidth estimation error e_A of IGI for different values of link utilization ρ. In both cases, the IGI algorithm stops at $E[y_i] = 1.001x$.

estimates keep fluctuating until the internal algorithm stops at $E[y_i] = 1.1x$ and the error is not necessarily decreasing over time.

To further investigate IGI's convergence behavior, we run the IGI algorithm until it terminates at $E[y_i] = 1.001x$ (recall that the turning point means $E[y_i] = x$). We plot the evolution of relative estimation errors for those two cases with $\rho = 70\%$ and $\rho = 30\%$ in Fig. 40. Observe from the figure that even though the initial packet spacing x becomes closer and closer to the turning point, IGI's estimation accuracy significantly fluctuates (between 18% and 122% of relative error) in case of $\rho = 70\%$, while for $\rho = 30\%$, it gets worse without showing a sign of convergence. This high variation of IGI's estimates for different values of $x/E[y_i]$ explains extremely high error in certain path configurations (case IV in Table XVI) and makes it difficult to decide when to stop IGI's internal algorithm to produce bandwidth estimates. In the figure, IGI produces the best estimate some time before it reaches the turning point and thereafter the accuracy becomes worse as the initial spacing becomes closer to the

turning point. Hence, unlike Envelope, using more samples in IGI does not necessarily lead to better estimation accuracy (for this reason, we let the IGI algorithm terminate at $E[y_i] = 1.1x$ to produce its available bandwidth estimates discussed in Section F.4).

2. CapProbe

Recall that CapProbe is based on the assumption that if packets in a probe pair have arrived at the receiver with the smallest combined one-way delay, then the packets have not been queued at any intermediate routers in the path and thus the inter-packet delay of the probe pair reflects the transmission delay of the bottleneck link. Based on this assumption, CapProbe uses 100 samples and the minimum delay condition to obtain the packet-pair that contains information about C. However, CapProbe's minimum filtering is sensitive to random queuing delays in front of the first packet of the pair and thus it is possible that the estimated capacity converges to a value that is very different from the true value of C. Furthermore, the convergence is rather random, which makes it difficult, if not impossible, to decide the optimal number of samples to be used in the estimation algorithm.

To illustrate the queuing effects discussed above, we simulate case VII with TCP cross-traffic for varying link utilization ρ between 30% and 70%. Fig. 41(a) shows CapProbe's relative capacity estimation errors e_C for different ρ. Observe that as ρ of the path increases from 30% to 70%, the relative estimation error e_C jumps from 0% to 48%. This indicates that CapProbe performs very well in a lightly utilized path; however, in a heavily-congested path, its capacity estimation accuracy significantly degrades. Furthermore, CapProbe's estimation accuracy fluctuates substantially depending on the number of samples used as illustrated in Fig. 41(b). For example, in a path with $\rho = 80\%$, $e_C = 30\%$ with 100 samples, 47% with 500 samples, 14% with 1000 samples, and 47% with 3000 samples. This indicates that if the measur-

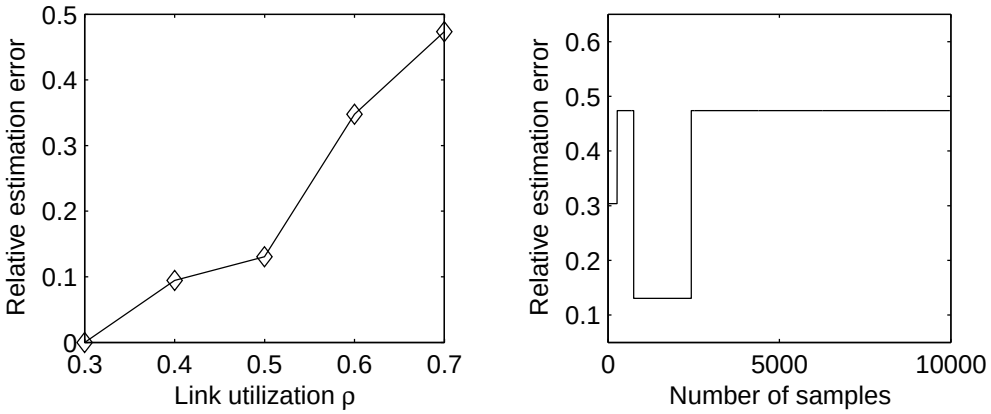

(a) e_C for different ρ (b) Evolution of e_C

Fig. 41. (a) Relative estimation error e_C of CapProbe for different utilization ρ of the links in case VII. (b) Evolution of relative capacity estimation error e_C of CapProbe for $\rho = 80\%$.

ing process stops at a random plateau where CapProbe has seemingly converged, its estimation accuracy will be random as shown in Fig. 41(b).

H. Impact of Probing Parameters in Envelope

Recall that Envelope's bandwidth estimation relies on two sets of measurements, which sample cross-traffic statistics at routers along the path using alternate probe-trains. In Envelope, there are two important and controllable parameters: initial input spacing x and probe-train length N. We discuss their impact on estimation accuracy of Envelope.

1. Initial Spacing

As discussed in Section F.1, Envelope's parameter selection routine sets x_a as small as possible to maximize the number of measurable non-tight links, while keeping $x_b = q/ADR$. Note that Envelope can use smaller x_b as long as it is larger than

x_a, which potentially increases the number of measurable non-tight links. We next answer the question whether reducing x_b (while keeping the same time span $x_b N_b$ by increasing N_b) affects estimation accuracy and if so, what impact it has on it.

Define $\rho_k = \lambda_k / C_k$ to be the utilization of router R_k, where C_k is the capacity of R_k and λ_k is an average cross-traffic rate arriving at R_k. Recall that $W^a_{n,k}$ and $W^b_{n,k}$ are respective n-sample averages of inter-departure spacings $y^a_{i,k}$ and $y^b_{i,k}$ of router R_k sampled at the receiver. Define $W^a_k = \lim_{n\to\infty} W^a_{n,k}$ and $W^b_k = \lim_{n\to\infty} W^b_{n,k}$. Assume that router R_k is measurable. Then, it is easy to obtain ρ_k from (130) and (133):

$$\rho_k = \frac{W^b_k - W^a_k}{W^b_{k-1} - W^a_{k-1}}. \tag{142}$$

With finite n, what we really sample at the receiver includes some measurement noise. Define measurement errors $\varepsilon^a_k = W^a_k - W^a_{n,k}$ and $\varepsilon^b_k = W^b_k - W^b_{n,k}$. Assume that when link k is examined, W^a_{k-1} and W^b_{k-1} for the previous router $k-1$ are known. Then, denoting by $\tilde{\rho}_k$ an estimate of link utilization ρ_k, we have:

$$\tilde{\rho}_k = \rho_k + \frac{\varepsilon^b_k - \varepsilon^a_k}{W^b_{k-1} - W^a_{k-1}}. \tag{143}$$

Note that the second term in (143) represents the measurement noise in estimation of ρ_k. Since sampling noise ε^b_k depends on the time span of a probe train $x_b N_b$, the numerator in (143) will be roughly the same regardless of the value of x_b as long as the time span $x_b N_b$ is maintained the same. Hence, measurement noise in (143) mainly depends on the difference between two output dispersions W^b_{k-1} and W^a_{k-1}. Also, note from (130) that an average inter-packet dispersion $E[y_{i,k}]$ exiting from router R_k is non-decreasing as k increase, which results in that a larger input spacing tends to produce a larger average dispersion from a router than that with a smaller input spacing. Hence, reducing x_b is likely to produce smaller output dispersion W_{k-1}, which in turn leads to higher measurement noise in estimation of link

utilization ρ_k.

To confirm our intuition discussed above, we conduct simulations with $x_a N_a =$ 36.4 ms and $x_b N_b = 268$ ms for two different values of $x_b = 24.4$ ms ($N_b = 11$) and $x_b = 1.92$ ms ($N_b = 140$) using case VII. In measuring the tight link (i.e., router R_3 in this example), the value of metric $\varepsilon_3^b - \varepsilon_3^a$ is 35 μs for larger $x_b = 24.4$ ms and 35.8 μs for smaller $x_b = 1.92$ ms, both of which are almost identical. However, the denominator $W_2^b - W_2^a$ is drastically different for two values of x_b. For instance, the denominator is 9.44 ms for the larger x_b and 0.39 ms for the smaller x_b, which results in only 0.44% error in estimation of ρ for the former case. However the same estimation error increases to 10% when smaller x_b is used.

In summary, the above result on selection of x_b implies that using smaller x_b can potentially degrade estimation accuracy in certain network configurations, while increasing the number of measurable non-tight links in a path. We note that adjusting x_b for each link can improve accuracy; however, it is not applicable to Envelope without significantly increasing measurement overhead since it requires inter-departure spacings at the previous link $k-1$ to measure the current link k.

2. Probe-Train Length

We next study how the probe-train length N affects the estimation accuracy of Envelope. For this example, we disable the automatic parameter selection routine in Envelope and manually set $x_a = q/C_0 = 0.12$ ms and $x_b = 2$ ms. Further set $N_b = N_a/2$ and $n = 5N_a$ so that N_b and n are scaled up as N_a increases. We then conduct simulations using case I under TCP cross-traffic for different probe-train length N_a and plot relative estimation errors e_C and e_A of the tight link in Fig. 42. As the figure shows, the estimation accuracy of Envelope is improved as probe-train length N_a increases. For example, Envelope produces the bottleneck capacity estimate with

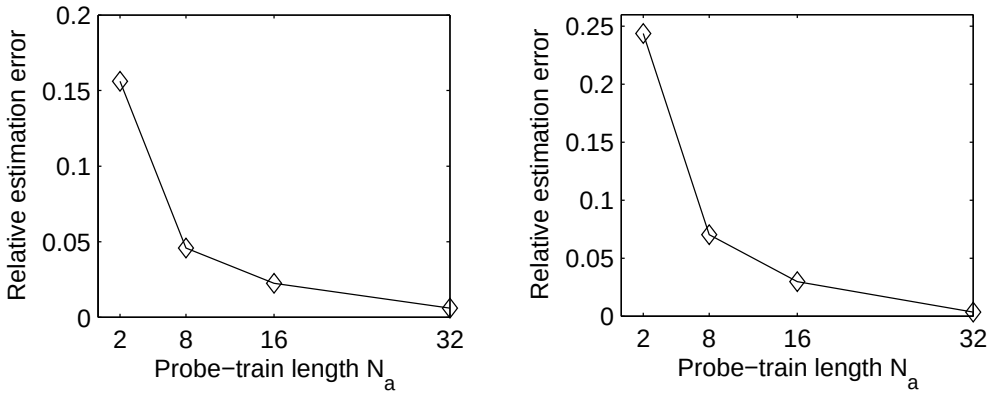

(a) e_C (b) e_A

Fig. 42. Relative estimation errors e_C and e_A of Envelope for varying probe-train length N_a in case I under TCP cross-traffic.

error 15% for $N_a = 2$; however, its error is reduced to 4% for $N_a = 8$ and 2% for $N_a = 16$ (see Fig. 42(a)). Similarly, with small train length $N_a = 2$, the accuracy of available bandwidth estimation is rather low (24% error), but when the train length increases to $N_a = 16$, Envelope estimates the available bandwidth with just 2% error as shown in Fig. 42(b). Note that Envelope's bandwidth estimation errors tend to zero as probe-train lengths N_a and N_b and the number of used trains n become large.

3. Amount of Probe Data

We finish the chapter by discussing the amount of probe data used in bandwidth sampling for different methods. For existing methods, we use the same packet size and number of trains or packet pairs recommended in the original paper. Table XIX shows the number of packets and corresponding data used to obtain bandwidth estimates for cases I and VII, for which Envelope uses the smallest and largest amount of data, respectively, among all studied cases with a parameter configuration $[N_l, N_h] = [10, 50]$. When a tool (e.g., Pathload) uses varying packet sizes, their average value ($\bar{q}$) is shown in the table.

Table XIX. Bandwidth Sampling Overhead for Cases I and VII

Methods		Case-I			Case-VII		
		# packets	$\bar{q}$ (B)	data (MB)	# packets	$\bar{q}$ (B)	data (MB)
Envelope	$[10, 50]$	$4,692$	$1,500$	7.0	$9,376$	$1,500$	14.0
	$[5, 15]$	$2,668$	$1,500$	4.0	$3,540$	$1,500$	5.3
Pathrate		$28,440$	$1,500$	42.7	$15,440$	$1,500$	23.1
CapProbe		200	800	0.2	400	800	0.3
Pathload		$15,600$	513	8.0	$14,400$	207	3.0
Spruce		$4,000$	$1,500$	6.0	$4,000$	$1,500$	6.0
IGI		360	700	0.3	780	700	0.5

As the table shows, IGI and CapProbe do not use many samples, while Pathload, Pathrate, and Envelope requires significantly more probe packets for their measurement. For example, Pathload uses 15600 samples for case I and 14400 samples for case VII, which accounts to $3 - 8$ MB of data. In Pathrate, cases I and VII respectively use 42 MB and 23 MB of samples to produce bottleneck bandwidth estimates. Note that when high values for N_l and N_h, i.e., $[N_l, N_h] = [10, 50]$, are used, Envelope uses 7 MB of probe packets for case I and 14 MB for case VII (see column 3 in the table). However, with smaller values of $[N_l, N_h] = [5, 15]$, the amount of used data is reduced to 4 MB for case I and 5 MB for case VII (see column 4 in the table). Recall that Envelope can also measure some non-tight links in certain network settings. For instance, it is able to measure the first three links in case VII, while it can only measure the tight link in case I. Hence, even with $[N_l, N_h] = [10, 50]$, per-hop measurement overhead in Envelope is 7 MB for case I and 4.6 MB for case VII, which are similar to those in Pathload for both cases (note that Pathload can only measure the tight link).

Also, recall that the number of samples required for Envelope is proportional to the number of hops in the path. Thus, for a 10-hop Internet path and using

$[N_l, N_h] = [10, 50]$, Envelope needs $17-35$ MB of probe data to examine all individual links. With smaller values of parameter configuration $[5, 15]$, it requires $10 - 13$ MB of data for the same 10-hop Internet path.

CHAPTER VI

ROBUST BANDWIDTH MEASUREMENT OF END-TO-END PATHS

In this chapter, we investigate the problem of end-to-end bandwidth estimation under realistic environment. Recall that existing approaches can be classified into *measurement tools* [22], [37], [41], [43], [49], [54], [72], [96], which usually have extensive simulations, but no convergence analysis for general cross-traffic, and *theoretical models* [34], [48], [60], [61], [62], [69], [75], which usually have provable convergence, but no practical implementation. Another issue in related work is the unknown performance of certain proposed algorithms in real networks where delay measurements are not perfect due to various OS and hardware-related timing irregularities [81]. We address the former issue by developing a measurement tool PRC-MT based on the models of [61] that not only achieves asymptotic accuracy in multi-path networks with arbitrary cross-traffic, but also simultaneously measures the capacity and available bandwidth of the tight link. We address the latter issue by performing a comparison study of existing tools in Emulab/PlanetLab and assessing their susceptibility to timing irregularities of end-hosts. Our results show that PRC-MT outperforms all existing tools in terms of accuracy, achieves similar convergence delay, and does not require any manual configuration. We also find that interrupt moderation may cause existing tools (such as Pathload [43], Pathchirp [85], and CapProbe [49]) to become quite inaccurate in certain network configurations and exhibit behavior completely different from that in `ns2` [92].

A. Introduction

Bandwidth of Internet paths is an important metric for many applications. However, without a direct access to network resources, end-to-end bandwidth measurement under general conditions on cross-traffic is a rather complex process [34], [61]. Unfortunately, theoretically justified techniques [61], [69], [75] are commonly not available as practical tools that can be used in real networks and vice versa (i.e., existing implementations are often based on fluid models that exhibit bias in bursty networks [61] and/or rely on heuristics with unknown theoretical performance). In addition, many current techniques produce unreliable results in actual networks where packet dispersions cannot be sampled accurately due to hardware interrupt moderation and various OS-imposed overhead [81].

1. Measuring the Tight Link

Existing techniques usually estimate either the *available bandwidth* [37], [44], [85], [96], or the *bottleneck bandwidth* [22], [49] of the path. The former term refers to the unused bandwidth A_t of the *tight* link (i.e., link with the smallest available bandwidth) and is closely related to the rate at which new applications can send into the path without congesting it. The latter metric is the capacity C_n of the *narrow* link (i.e., link with the lowest speed), which can be viewed as an upper bound on the sending rate that the path can support. Note that A_t can be measured in all network configurations, while this is not necessarily true for C_n.

Even though both A_t and C_n are useful metrics, certain applications require capacity C_t of the tight link instead of C_n, which allows them to compute the utilization of the tight link and possibly achieve better characterization of what causes bottle-

necks in the path.[1] Only a few approaches can measure C_t [47], [48], [72], but they are either based on single-hop models that are inaccurate in multi-path networks, or rely on hop-by-hop probing, which we do not study in this chapter. A recent theoretical development [61] shows that both A_t and C_t can be provably measured in any end-to-end path with infinite buffers by exploiting a certain piece-wise linear relationship between the sending rate r_I of probe packets and the corresponding arrival rate r_O at the receiver. Although this work opens a door for developing a new characterization technique for tight links, it remains to be seen if an automated implementation can achieve good performance in networks with limited buffer space and exhibit overhead comparable to that of existing tools.

Recall that [61] relies on correctly identifying the first two linear segments of the *probing response curve* (PRC), which is a functional relationship between r_I/r_O and r_I. Identifying and separating the linear segments in a stochastic PRC is a non-trivial task since the curve itself may fluctuate and/or deviate from the fluid piece-wise linear limit depending on path-specific characteristics as well as the number of probes per train and their size. In addition, building an entire PRC sometimes requires sending a large amount of traffic into the path and exhaustively probing a wide variety of sending rates (i.e., as done in [63]). Thus, the main challenge in PRC-based estimation is the development of automated algorithms for detecting linear segments in practice and selecting probing rates that result in quick convergence of the method.

In this chapter, we tackle the above problems in an iterative probing technique we call *PRC Measurement Tool* (PRC-MT), which is capable of estimating both A_t and C_t in arbitrary multi-hop paths. PRC-MT autonomously selects probing rates, train and packet size, and termination conditions so as to achieve any desired tradeoff

[1] Also note that certain bandwidth estimation tools [36], [96] require C_t in order to measure A_t.

between accuracy and overhead (i.e., better accuracy requires more probes and vice versa). We implement PRC-MT in Linux and evaluate its performance in a network of software routers of Emulab. We find that PRC-MT, limited to the execution delay of prior methods (i.e., $90-120$ seconds), estimates A_t and C_t with $90-99\%$ accuracy in a wide range of network configurations.

2. Timing Irregularities

Attempting to run existing tools in PlanetLab, we found that some of them frequently produced no estimate at all (e.g., Pathload [43], [44]) while others returned results that did not make much sense (e.g., CapProbe [49]). It became immediately clear that one of the main factors that differentiates bandwidth estimation in real networks from that in `ns2` is *end-host timing irregularities*, which include hardware interrupt moderation [81] and OS scheduling delay jitter (which depends on the CPU utilization of the host). We sampled a number of hosts in PlanetLab and found that many of them used interrupt moderation, which could be enabled at the sender (i.e., packets did not leave the host immediately), at the receiver (i.e., arriving packets were delivered to the OS "bunched up"), or at both. In fact, modern gigabit NICs enable interrupt moderation by default, which means that bandwidth-measurement tools that are not robust to timing irregularities are unlikely to be successful in real networks.

To reduce the effect of interrupt moderation, techniques such as Pathchirp [85] and the current version of Pathload [44], [81] incorporate mechanisms that aim to "weed out" packets affected by interrupt delays. Specifically, Pathchirp requires manual modification to force it to send more probing packets to obtain an accurate estimate. For Emulab experiments in this chapter, we use 6 times more packets per probing train (i.e., chirp) than the default value in order to achieve reasonable accuracy. This modification reduces the effect of interrupt delay, but prolongs the

measurement. On the other hand, Pathload attempts to filter out affected packets without increasing the number of probing packets, which unfortunately has a limited effect when interrupt delays become non-trivial. This makes Pathload's estimation much more susceptible to error, which happens fairly often in practice.

In order to obtain a working version of Pathload that can be used in our comparison with PRC-MT in scenarios with non-negligible interrupt delays, we investigate Pathload's internal algorithm and find that its estimation instability stems from its delay-trend detection mechanism that is not robust under bursty packet arrival introduced by network hardware. To overcome this problem, we introduce two trend-detection algorithms based on signal de-noising techniques and show that they significantly improve Pathload's performance in real networks. We call the new method *Interrupt Moderation Resilient Pathload* (IMRP) and show that it not only outperforms the original Pathload, but also achieves better estimation accuracy than Pathchirp under a wide range of interrupt delay δ, while using approximately half the time and 75% less bandwidth.

We next assess the performance of PRC-MT under interrupt moderation in comparison with IMRP, Pathchirp [85], IGI/PTR [36] using metric A_t and Pathrate [22], CapProbe [49] using metric C_t when the narrow link coincides with the tight link. For available bandwidth A_t, our results show that PRC-MT exhibits no negative side-effects related to interrupt moderation, converges in $90-140$ seconds in all examined topologies, and outperforms the other studied methods in terms of accuracy ($1-5\%$ error). We also find that IMRP's estimates are generally within 7% of the correct value and its convergence delay is $80-100$ seconds. After manually tweaking Pathchirp's train size and running duration, we were able to reduce its error to about 15% and execution time to 200 seconds; however, its default version performs much worse. Even though we supply IGI/PTR with the correct tight-link capacity C_t, both

methods exhibit $40-60\%$ error, but on the bright side converge within just $3-5$ seconds.

For tight-link capacity C_t, PRC-MT's error is below 7% in all studied cases, while that of Pathrate exceeds 15% and that of CapProbe is close to 60%. The measurement delay of prior methods is also significantly higher than that of PRC-MT – almost 2200 seconds in Pathrate and 500 seconds in CapProbe. Our Emulab results suggest that existing methods (in their unmodified form) may experience certain non-negligible performance issues in real networks, while techniques introduced in this work (PRC-MT and IMRP) are much more likely to remain robust in practical settings. In fact, PRC-MT not only provides automatic self-configuration that overcomes interrupt-moderation effects and achieves quick convergence, but also simultaneously estimates (A_t, C_t) and is asymptotically accurate. We finish the chapter by measuring two paths in PlanetLab [80] using all 8 studied tools and discussing their possible inaccuracies.

B. PRC-MT: Bandwidth Estimation Using Probing Response Curve

In this section, we investigate practical issues and difficulties of using PRC in measuring available bandwidth and capacity of the tight link. We then develop empirical algorithms that overcome these problems and lead to a new measurement tool called PRC-MT, which can measure both bandwidth metrics of the tight link over multi-hop paths under arbitrary cross-traffic and routing patterns. We start by describing the basic idea of this approach.

1. Basic Idea

Define r_I to be a sending rate of packets in a probe-packet train at the sender and r_O to be their arrival rate at the receiver. Further define $F = r_I/r_O$ to be the ratio

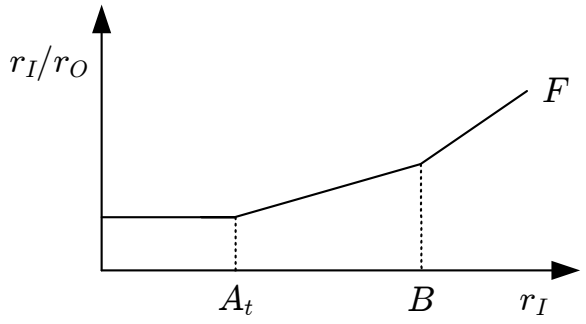

Fig. 43. Relationship between input rate r_I and output rate r_O.

of r_I and r_O under fluid cross-traffic. Then, F can be expressed as [61]:

$$F = \frac{r_I}{r_O} = \begin{cases} 1 & r_I \leq A_t \\ \dfrac{\lambda_t + r_I}{C_t} & A_t \leq r_I \leq B \end{cases}, \tag{144}$$

where λ_t is the amount of cross-traffic that traverses the tight link, A_t and C_t are the respective available bandwidth and capacity of the tight link, and B represents a certain input rate that is greater than A_t (we will discuss this later on). Fig. 43 illustrates a hypothetical fluid response curve F, which shows the relationship between r_I/r_O and r_I.

Observe from the figure that F consists of piece-wise linear segments (at least two in multi-link paths), which breaks at particular input rates A_t and B. The first segment ends when input rate r_I equals the available bandwidth A_t of the tight link, while the second segment breaks down at rate B. Hence, to extract A_t, we only need to identify the first break point where F starts to become larger than one. This can be done by conducting a binary search without fully discovering the line segments (details of this will be described later).

For estimation of the tight-link capacity C_t, it is required to compute slope α of the second line segment since $C_t = 1/\alpha$ from (144). To do this, we need to choose two

points on the second line segment, which may not be easy to identify without knowing the exact rate B of the second break point. Recall from [61] that B is dependent on the routing matrix of cross-traffic traversing the path and thus it is not possible to compute its value without complete knowledge of cross-traffic routing patterns. What we know is that B is no less than the second smallest hop-available bandwidth of the path. Judging from this lack of knowledge on B, extracting C_t appears to be harder than finding A_t and be more susceptible to measurement errors.

Now the question we have is how to find the first break point for estimation of A_t and how to identify the second line segment and compute its slope α for capacity estimation without even knowing the exact value of B in practice. We address these issues in the following subsections.

2. Issues

Define Z to be the real probing response curve of a path over which arbitrarily routed bursty cross-traffic flows traverse. Note that Z is different from the fluid curve F (as long as probe-train length N and probe-packet size q are finite) and this makes the task of identifying the first break point and the second linear segment in Z significantly more challenging than that in the fluid case. Although it is proven in [61] that Z is lower-bounded by fluid response curve F and asymptotically approaches F as $N \to \infty$ or $q \to \infty$, $Z - F > 0$ in real networks, where the size of packets is typically limited by the maximum transfer unit (MTU) of network elements and the packet-train length N cannot be arbitrarily large since router queue sizes are limited.

Before discussing implications of this deviation of Z from F, we explore how the response curve Z behaves with different probe-train length N by conducting experiments in Emulab and `ns2` [73] using a single-hop topology of capacity $C_t = 90$ Mb/s. For this experiment, we keep link utilization at 32% (i.e., $\lambda_t = 29$ Mb/s) and

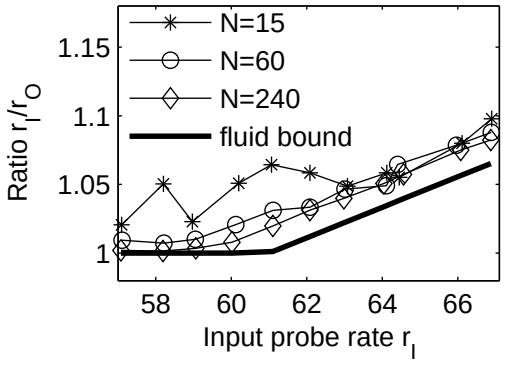

Fig. 44. Probing response curves for different values of probe-train length N in Emulab experiments.

plot the response curve Z for several different values of N in Fig. 44.

Notice in Fig. 44 that when N is small (e.g., 15), Z fluctuates substantially and exhibits large deviation from the fluid lower-bound F. However, as N increases, Z shows prominent two linear lines and its deviation from F becomes smaller. For example, with $N = 240$, r_O is within 1.5% of r_I until r_I reaches around 61 Mb/s, which is the available bandwidth A_t of the path in this setup. Note that the difference between Z and F would be zero as N becomes large (we do not show this since we cannot use arbitrarily large N in Emulab without causing packet loss due to queue size limit).

To better demonstrate behavior of Z for a large probe-train length N, we conduct `ns2` simulations for different N with two different probe-packet sizes $q = 1500$ and 200 bytes. As shown in Fig. 45(a), although Z deviates from F with $N = 15$, it converges to F when $N = 240$, which in general agrees with the Emulab result in Fig. 44. Note that the simulation result in Fig. 45(a) shows less variation in Z and faster convergence of Z to F, which we believe stems from perfect timestamping of sending and arriving packets in `ns2`. With smaller packets (e.g., $q = 200$ bytes), we observe a similar behavior of Z even though it exhibits higher fluctuation and requires larger

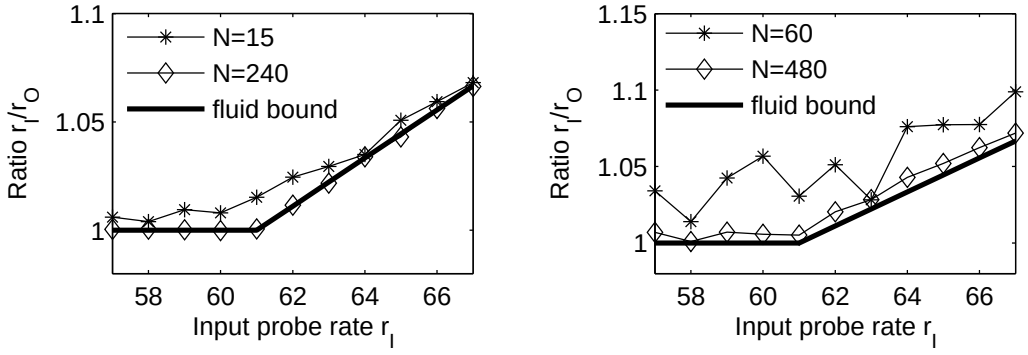

(a) ns2 ($q = 1500$ B) (b) ns2 ($q = 200$ B)

Fig. 45. Probing response curves for different probe-train length N in `ns2` simulation.

N to converge to F (see Fig. 45(b)).

Next, we discuss how the evolution of the real response curve Z on input probe rate r_I affects bandwidth estimation. Recall that to estimate bandwidth A_t and C_t, we need to identify the end of the first line segment (for A_t) and stable second linear line (for C_t) from the response curve Z. For accurate discovery of the first break point in Z, it is required that variation in Z should be small for different r_I. More importantly, it is desired to have a second line segment that is *parallel* to that in F even though they do not match (i.e., deviation $Z - F > 0$). Note that if the second line segments in Z and F are parallel, then we can use any two points on the line in Z to compute its slope α, which reflects the true capacity C_t of the tight link regardless of their locations as long as they are on the second line segment. Further note that under this condition the amount of deviation $Z - F$ has no direct impact on estimation accuracy. However, if the second line segment in Z is not parallel to that of fluid counter part F, then estimation accuracy of C_t depends on which two points we select in computing the slope α, which is a non-trivial task in practice.

To confirm the above discussion and demonstrate the direct impact of the probe-train length N on estimation accuracy, we conduct experiments in Emulab using the

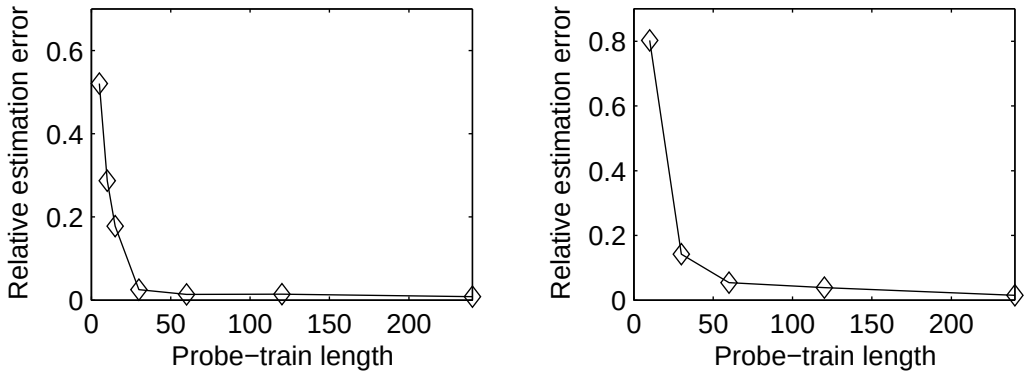

(a) e_A (b) e_C

Fig. 46. Evolution of relative estimation errors e_A and e_C of PRC-MT for different N.

same single-hop setup. We use error metrics e_C and e_A, which are defined in Chapter V to be the respective relative estimation errors of capacity and available bandwidth of the tight link L_t of a path:

$$e_C = \frac{|C_t - \tilde{C}_t|}{C_t}, \quad e_A = \frac{|A_t - \tilde{A}_t|}{A_t}, \tag{145}$$

where $\tilde{C}_t$ and $\tilde{A}_t$ are the respective estimates of the true capacity C_t and available bandwidth A_t of the tight link L_t. We then illustrate evolution of relative estimation errors e_A and e_C for different N in Fig. 46. As Fig. 46(a) shows, e_A quickly drops from 28% (for $N = 10$) to a value that is less than 2% as N becomes 60. Similarly, estimation accuracy of C_t is significantly improved from $e_C = 80\%$ for $N = 10$ to 3% for $N = 120$ (see Fig. 46(b)). These results indicate the importance of having sufficiently large N, which makes line segments in the response curve Z straight line without much fluctuation and allows accurate bandwidth estimation.

Note that even though a large N brings down fluctuation of line segments in Z, using an arbitrarily large value is not desirable since it increases measurement overhead and can also induce too much packet loss within a probe train. On the other hand, use of too small N results in high estimation errors. Hence, it is clear

that there exists a trade-off between accuracy and overhead and thus proper selection of train length N is very important in developing PRC-MT. However, selection of appropriate value of N is non-trivial since fluctuation of line segments in the real response curve Z depends on probe parameters and unknown path characteristics such as amount of cross-traffic.

Now, the problem we need to solve is how to select N in practice for a particular path such that the second line segment in Z becomes parallel to that in F. We investigate this next.

3. Parameter Selection

Recall that for a sufficiently large N, the slope of the second line segment in Z converges to a value that makes it parallel to that of fluid curve F in an input rate range $r_I \in [A_t, B]$. We can interpret this as that the ratio r_I/r_O saturates at a certain value when N becomes large. To confirm this, we examine the quantity of r_I/r_O for different N using the Emulab setup discussed in the previous subsection. For this purpose, we send packets with rate $r_I = 68$ Mb/s (which is higher than the available bandwidth $A_t = 61$ Mb/s of the path in this setup) with varying N and plot r_I/r_O in Fig. 47. As the figure shows, r_I/r_O quickly drops to a value that is slightly larger than the fluid-bound (i.e., $(\lambda_t + r_I)/C_t = 1.07$) as N increases. This leads us to investigating an empirical method, which iteratively probes for N that makes the ratio r_I/r_O saturate for a given input rate r_I.

In what follows below in this section, we discuss a simple selection procedure for N, which adjusts its value based on variation of r_I/r_O for a given sending rate r_I discussed above. Although there is no particular constraints on the input sending rate for this routine, it is preferable to use a rate that is not so smaller than available bandwidth A_t of the path since variation of the ratio r_I/r_O for an input rate that is

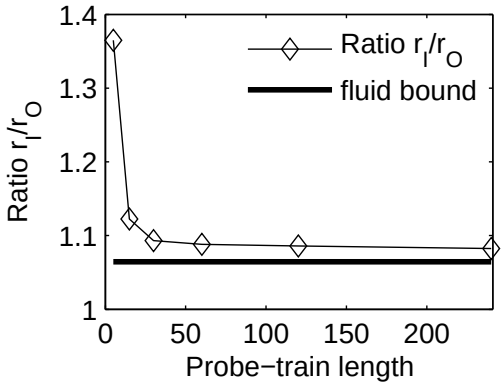

Fig. 47. Evolution of ratio r_I/r_O for different values of N.

smaller than A_t diminishes rather fast with small increase in probe-train length N [61]. Finding a rate that is no less than A_t would be sufficient for this purpose and Asymptotic Dispersion Rate (ADR) [21] of a path is a good candidate for r_I since it is proven in [21] that $A_t < ADR$. Hence, PRC-MT probes for ADR by sending a single packet train and computes $ADR = q/E[y_i]$ at the receiver (where $E[y_i]$ is the average inter-packet dispersion of packets in the probe train i), which is similar to Pathrate [21]. With the input sending rate r_I determined, the rest of the procedure for train-length probing is as follows.

Define γ to be the ratio of input rate and output rate: $\gamma = r_I/r_O$ and γ_{old} to be the previous value of γ. Further define N_{min} and N_{max} to be a respective minimum and maximum train length that can be adjusted by the user and σ to be a certain threshold that can vary between zero and one. The selection routine conducts a binary search between N_{min} and N_{max} to find a value that saturates γ. This procedure tests if γ converges to a certain value for a given length N by sending to the receiver packet trains of length N with rate $r_I = ADR$. To assess saturation of γ, the selection procedure computes the following relative error metric ε:

$$\varepsilon = \frac{|\gamma - \gamma_{old}|}{\gamma}. \tag{146}$$

When $\varepsilon \leq \sigma$, the routine decreases N; otherwise, it increases N.

Note that users can use any packet size $q_{min} \leq q \leq q_{max}$ (where we use $q_{min} = 200$ bytes and $q_{max} = 1500$ bytes), in which case N_{min} and N_{max} are scaled up or down by q_{max}/q. This routine ensures us to select a larger N when a user chooses a smaller packet q, sufficing the condition for stabilizing line segments in Z as discussed in the previous subsection. For experiments in Sections C. and D., we use $N_{min} = 60$, $N_{max} = 3000$, $\sigma = 0.02$, and $q = 200$ bytes.

4. Bandwidth Probing

With probe-train length N in hands, our next question is how to identify the first break point in the response curve Z, at which input sending rate r_I starts to become larger than the arrival rate r_O (see Fig. 43). To efficiently search for this point, PRC-MT uses an iterative probing-based binary search, which is similar to Pathload [44]. Note, however, that the two tools are different in a way that assesses whether an input rate r_I corresponds to A_t. For example, PRC-MT determines if the current rate $r_I > A_t$ by *directly* comparing r_I with r_O, while Pathload *infers* it by examining one-way delays of probe packets.

Similarly to Pathload, PRC-MT sends a group of K packet trains with a given rate r_I. Then, based on how much fraction η of K trains belongs to either $r_I > r_O$ or $r_I < r_O$, it adjusts its sending rate r_I. Specifically, PRC-MT decrease r_I if a fraction η of K probe-trains are asserted to be $r_I > r_O$; increase r_I when the ratio of the number of trains with $r_I < r_O$ to K is more than η. Note that it is possible that neither of the above two cases happens (i.e., none of ηK trains belongs to either $r_I > r_O$ or $r_I < r_O$). If this is the case, we treat it like a "grey region" in Pathload (see [44] for details).

This binary search process continues until the bandwidth range $[W_L, W_H]$ around

A_t becomes smaller than a certain threshold ω, which can be automatically selected ($\omega = 0.02ADR$) based on measured ADR or given by the user. PRC-MT returns $\tilde{A}_t = (W_L + W_H)/2$ as the available bandwidth estimate of the tight link when its internal algorithm terminates. We empirically set $\eta = 60\%$ and $K = 12$ as their respective default value in PRC-MT.

After finding a bandwidth range $[W_L, W_H]$, PRC-MT starts a procedure for estimating the tight-link capacity C_t. The main focus of this routine is to select two points that will be used to extract C_t without the knowledge of the end of the second line segment. Note that to facilitate estimation of C_t, PRC-MT records the sending rate r_I and its corresponding receiving rate r_O during the available bandwidth probing whenever the current r_I reduces the upper bound W_H of the bandwidth range due to r_I being larger than r_O. These recorded points are the possible candidates for computing a capacity estimate $\tilde{C}_t$.

Note that we can select any two among the recorded points to extract C_t in ideal case (i.e., the second segment is a perfect straight line and there is no measurement noise). Unfortunately, however, there is no straightforward method that chooses optimal two points with certain measurement noise and imperfect straight line, which leads us to exploring empirical method (which we explain below).

Assume that there are $m \geq 2$ recorded points $(u_1, v_1), \ldots, (u_m, v_m)$, where u_i and v_i $(i = 1, \ldots, m)$ are the respective sending and receiving rates used during the available bandwidth probing. Then, PRC-MT first chooses (u_i, v_i), where u_i is the smallest among m points that satisfies $u_i \geq W_H$. We have two reasons for not using $r_I = \tilde{A}_t$ as the first point. First, it is not very clear from the response curve Z where the second line segment starts around A_t (see Fig. 44). The other reason is that the estimated value $\tilde{A}_t$ may be on the first line segment due to measurement error ($\tilde{A} < A_t$), which can result in high errors in capacity estimation.

Recall that to produce accurate capacity estimates $\tilde{C}_t$, the second point should be on the second line segment. Since PRC-MT picks the first point (u_i, v_i) whose sending rate u_i is closest to W_H among recorded points, we may consider the point that is close to the first one as the best candidate for the second point since it has higher chance to be on the second line segment. However, if two points are close to each other, then computing linear slope of the two points is more susceptible to measurement noise. Hence, it is better to have the second point as far away as possible from the first one as long as they are on the second line segment. Since there is no way to determine the end of the second line segment, we empirically select farthest two points among the recorded points to extract the tight-link capacity. Based on the above discussion, PRC-MT uses (u_j, v_j) as the second point, where u_j is the largest among the recorded points.

Having two points (u_i, v_i) and (u_j, v_j) selected, PRC-MT computes the tight-link capacity estimate $\tilde{C}_t$:

$$\tilde{C}_t = \frac{v_i v_j (u_i - u_j)}{u_i v_j - u_j v_i}, \tag{147}$$

which is the inverse of a slope of the linear line segment between $(u_i, u_i/v_i)$ and $(u_j, u_j/v_j)$.

Before concluding this section, we should note that if the number of recorded points m is less than 2, PRC-MT requires to send additional packets with rates r_I that is larger than $\tilde{A}_t$ to obtain (r_I, r_O) pairs. Even though this case will rarely happen (only when a very large threshold ω is used to terminate the algorithm), we include this for the sake of completeness.

C. Performance of PRC-MT

To evaluate the performance of PRC-MT, we conduct experiments in Emulab[2] [24]. We examine estimation accuracy of PRC-MT and its convergence behavior and then compare these results with those in existing methods. For experiments in this section, we do not use interrupt moderation (i.e., interrupt delay $\delta = 0$) at the receiver and defer discussion of these tools under interrupt delay to Section D. We start by describing the experimental setup.

1. Experimental Setup

For all experiments, we use a topology shown in Fig. 48, in which source PS sends probe data to the destination PR through five routers $R_1, \ldots, R_5$. Nodes S_i ($i = 1, 2, 3, 4$) send cross-traffic packets to destination nodes D_i ($i = 1, 2, 3, 4$) at an average rate λ_i. The speed of all access links is 100 Mb/s (delay 10 ms) and the remaining links L_i ($i = 1, 2, 3, 4$) between routers R_i and R_{i+1} have capacities C_i and propagation delay 40 ms.

To examine the estimation accuracy of PRC-MT, we use six different network settings shown in Table XX, which lists the capacity and available bandwidth of each link for different experimental scenarios. Note that the table shows a fair amount of cross-traffic at each node, which is needed to ensure that each case represents some non-degenerate scenario. Without cross-traffic, most studied techniques are accurate and their comparison is not very insightful. The values in braces in each row represent the tight-link capacity C_t and available bandwidth A_t of the path for each case. The values in square brackets are the capacities C_n of the narrow link (i.e., bottleneck bandwidth) for each case. Notice from the table that the experimental settings cover

[2]In Emulab, users can change configuration of network interface cards.

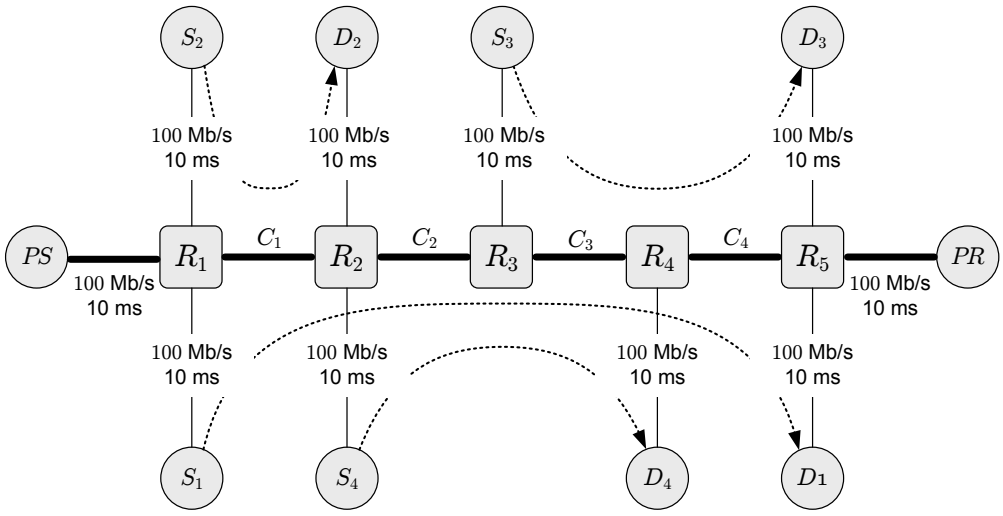

Fig. 48. Evaluation topology in Emulab.

Table XX. Evaluation Setup

	Different link bandwidths (Mb/s)							
	C_1	A_1	C_2	A_2	C_3	A_3	C_4	A_4
Case-I	{75	31.8}	90	51.6	90	42.1	[60]	40.7
Case-II	75	41.3	90	70.7	90	46.7	{[60]	26.4}
Case-III	[60]	35.8	90	70.7	90	23.4	{75	18.1}
Case-IV	{[60]	21.6}	90	65.9	90	42.1	75	36.7
Case-V	[60]	50.2	90	61.1	{90	41.9}	75	50.8
Case-VI	75	28.9	90	37.8	{90	13.8}	[60]	31.2

all possible relationships between the location of the tight link and narrow link. For instance, in cases II and IV, the narrow link *coincides* with the tight link; in cases I and VI, the narrow link *follows* the tight link; while in cases III and V, the narrow link *precedes* the tight link.

In all experiments, we use TCP cross-traffic generated by the Iperf traffic generator [40] to load network paths. Although Iperf traffic does not exactly resemble Internet traffic, it is adequate for our purposes in this chapter. We run 100 threads in each cross-traffic source S_i to generate TCP flows that are injected into routers R_1,

Table XXI. Performance of PRC-MT ($\delta = 0$ μs)

Evaluation scenario	Relative estimation error		
	e_A	e_C	time
Case-I	3.49%	6.04%	89 sec
Case-II	2.35%	2.52%	115 sec
Case-III	0.88%	1.31%	96 sec
Case-IV	5.05%	3.51%	138 sec
Case-V	5.51%	6.38%	102 sec
Case-VI	9.74%	3.51%	125 sec

R_2, and R_3 and keep the utilization of each router R_i according to the values shown in Table XX. To maintain a fixed average utilization at each link in the experiment, we place an additional router (not shown in the figure) between node S_1 and router R_1, S_2 and R_1, S_3 and R_3, and S_4 and R_2 to limit the aggregate sending rate of TCP flows to the capacity of the additional router. The utilization of R_i is controlled by properly setting the capacity of the auxiliary router.

2. Estimation Accuracy of PRC-MT

We next investigate estimation accuracy and convergence behavior of PRC-MT. Experimental results of PRC-MT are summarized in Table XXI, which shows relative estimation errors e_A and e_C and convergence time of PRC-MT's internal algorithm.

As Table XXI shows, PRC-MT estimates available bandwidth of the tight link with over 90% accuracy for all cases studied in this chapter. Its estimation accuracy of the tight-link capacity is as good as that of available bandwidth for all studied cases. In all experiments, PRC-MT's algorithm converges within 140 seconds.

In what follows below, we briefly examine convergence behavior of PRC-MT using cases II and IV and show the evolution of PRC-MT's estimates. For this purpose, we trace bandwidth range $[W_L, W_H]$ of the tight link every time PRC-MT's

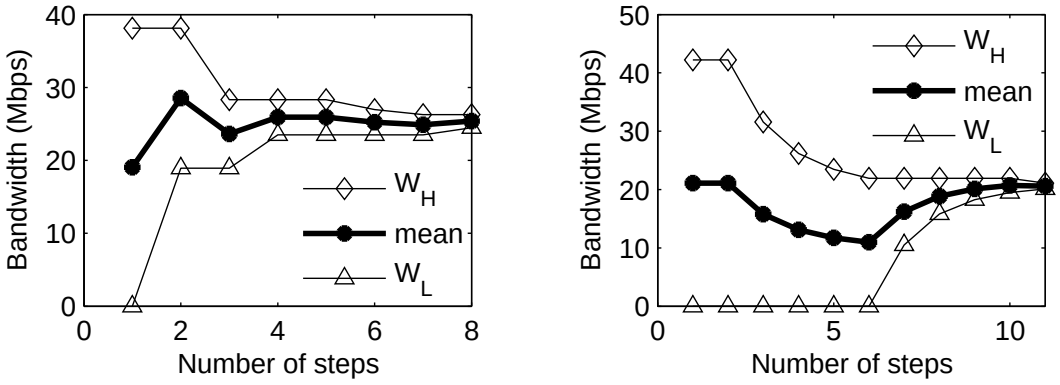

(a) Case-II (b) Case-IV

Fig. 49. Convergence characteristics of PRC-MT for cases II and IV.

internal algorithm updates it and plot the evolution of the range and their average $\tilde{A}_t = (W_L + W_H)/2$. As Fig. 49(a) shows, the available bandwidth estimate $\tilde{A}_t$ in case II converges to a value that is within 3% of its true value ($A = 26.39$ Mb/s) in 8 steps. Similarly, in case IV, $\tilde{A}_t$ approaches its true value $A = 21.6$ Mb/s with error $e_A = 5\%$ in 11 steps. We observe a similar convergence behavior of PRC-MT for other studied cases, but we omit these results for brevity.

3. Performance Comparison

In this subsection, we compare PRC-MT with several existing available bandwidth estimators (Pathload [44], Pathchirp [85], and IGI/PTR [37]) and capacity estimation tools (Pathrate [21] and CapProbe [49]) with respect to estimation accuracy using the setup shown in Table XX. For existing methods, we use user-level implementations (which do not require super-user privilege to run the program) that are publicly available or obtained from the authors.

Table XXII. Available Bandwidth Estimation Methods ($\delta = 0$ μs)

Estimation method	Metrics	Evaluation scenario					
		Case-I	Case-II	Case-III	Case-IV	Case-V	Case-VI
PRC-MT	e_A	3.49%	2.35%	0.88%	5.05%	5.51%	9.74%
	time	89 sec	115 sec	96 sec	138 sec	102 sec	125 sec
Pathload	e_A	9.45%	8%	7.57%	6.48%	16.58%	15.01%
	time	69 sec	69 sec	70 sec	69 sec	108 sec	99 sec
Pathchirp	e_A	10.84%	8.53%	0.39%	1.62%	19.81%	18.04%
	time	200 sec	200 sec	200 sec	200 sec	200 sec	200 sec
IGI	e_A	10.58%	4.21%	72.76%	19.72%	13.38%	98.56%
PTR		16.02%	9.93%	30.28%	24.63%	5.31%	59.24%
	time	3 sec	4 sec	5 sec	6 sec	3 sec	5 sec

a. Available Bandwidth Comparison

We first compare PRC-MT with Pathload, Pathchirp, and IGI/PTR. We also have studied Spruce [96], but do not include its result here since it performs significantly worse than the other tools in all cases studied in this chapter (see [56], [61] for details of Spruce and possible causes of its estimation inaccuracy in multi-hop paths).

Table XXII shows relative estimation errors e_A for different cases. For Pathload, we average the low and high values of the produced estimates after its internal algorithm terminates. For Pathchirp, we use "jumbo" option J that increases accuracy by sending more packets in each probe train (called chirp) than the default. We manually set this option $J = 6$ to send 6 times more packets than the default to produce accurate and reliable available bandwidth estimates. Selection of the value J is purely based on trial and error since Pathchirp does not offer any automatic selection mechanism for it. Different from other tools studied in this subsection, Pathchirp is an open loop system, which does not have an automatic convergence mechanism. It runs for a specified time t and stops when the running time reaches t, without

knowing convergence of its estimate. We use $t = 200$ seconds to obtain results in this chapter even though its default execution time is $t = 600$ seconds since its estimation accuracy has not been improved even we run it more than 200 seconds in our experimental setup. In IGI/PTR case, we use the estimates available at the end of its internal convergence algorithm. Note that we feed IGI/PTR the *exact* tight-link capacity C_t, while all other tools operate without this information.

As the table shows, Pathchirp produces estimates with less than 20% of error for all cases. Note that IGI/PTR produces estimates very quickly (40 times faster than Pathchirp), but its estimation error is significantly higher than Pathchirp. Pathload measures the paths with accuracy that is similar to Pathchirp. Notice in the table that PRC-MT produces bandwidth estimates with accuracy that is comparable to or better than those of Pathload and Pathchirp.

b. Bottleneck Bandwidth Comparison

Note that only in cases II and IV, the narrow link coincides with the tight link of the path. Hence, we compare PRC-MT only in these path configurations with recent bottleneck bandwidth estimators CapProbe and Pathrate. For CapProbe, we use 1800 packet-pairs for estimation since it often does not produce good estimates (on the studied paths) with 100 pairs recommended in the paper [49]. In Pathrate, the internal algorithm executes for over 2000 seconds (around 36 minutes) to get estimates of the bottleneck capacity of the end-to-end path (note that Pathrate has quick termination mode that takes about 100 seconds, but we do not use this since its estimate is not accurate in the cases studied in this chapter).

Table XXIII illustrates relative capacity estimation errors e_C of the different methods. As the table shows, PRC-MT produces capacity estimates $\tilde{C}_t$ of the tight link within 5% of its true values C_t in the studied cases, which is significantly better

Table XXIII. Capacity Estimation Methods ($\delta = 0$ μs)

Methods	Relative estimation error e_C			
	Case-II		Case-IV	
	e_C	time	e_C	time
PRC-MT	2.52%	115 (sec)	3.51%	138 (sec)
Pathrate	28.33%	2191 (sec)	21.67%	2191 (sec)
CapProbe	47.32%	500 (sec)	63.38%	500 (sec)

than Pathrate and CapProbe.

D. Impact of End-Host Interrupt Delays on Bandwidth Measurement

As use of interrupt moderation has become a common practice in modern network settings, host machines in real networks employ interrupt delays that vary widely in order to reduce CPU utilization and to increase network throughput. It is reported in [39] that the range of interrupt delays for Intel Gigabit NIC (GbE) is $83 - 250$ μs for Microsoft Windows-based systems and $125 - 1000$ μs for Linux-based systems. Jin *et al.* [45] also report that a variety of systems equipped with Gigabit NICs require to delay generation of interrupts over 470 μs to achieve good throughput in receiving high-speed TCP streams and to substantially reduce CPU utilization.

To assess robustness of bandwidth estimation tools under various interrupt delays, we investigate how this wide range of interrupt delays affect them by comparing their estimation accuracy using the same Emulab setup in Table XX. Among tools evaluated under no interrupt delay ($\delta = 0$) in Section C, use of interrupt moderation affects Pathload the most, while others exhibit estimation accuracy that is similar to that in the cases without using interrupt moderation. Thus, before conducting comparisons among tools under interrupt delays, we study the impact of interrupt moderation using Pathload as an example and propose a new measurement algorithm

Table XXIV. Measurement Reliability of Pathload

Evaluation scenario	Interrupt delay δ			
	0 μs	100 μs	125 μs	$>$ 125 μs
Case-I	9.45%	1.44%	−−	−−
Case-II	8%	8.52%	−−	−−
Case-III	7.57%	14.9%	15.01%	−−
Case-IV	6.48%	5.74%	−−	−−
Case-V	16.58%	3.6%	−−	−−
Case-VI	15.01%	20.74%	34.65%	−−

that is resilient to various interrupt delays and significantly improves Pathload's estimation reliability under such conditions.

1. Effect of Interrupt Moderation on Pathload

We run Pathload with 4 different values of interrupt delays δ and report estimation results for each case in Table XXIV, which shows relative estimation errors e_A of available bandwidth for each case. As the table shows, with relatively small interrupt delays (e.g., $\delta \leq 100$ μs), Pathload estimates available bandwidth of the tight link with over 80% accuracy for all cases studied in this chapter. Notice, however, from the table that when δ becomes larger than 125 μs, it is unable to produce estimates for any of the cases as shown in the table as empty cells, which suggests that its internal algorithm is susceptible to non-trivial interrupt delays.

To better understand the above problem, we investigate Pathload's internal algorithm in detail and identify what causes its measurement to be unstable under non-negligible values of δ. Recall that Pathload [44] sends back-to-back packets in a train of size $N = 100$ with a fixed rate R and examines one-way delay[3] (OWD) of each

[3]One-way delay of a packet is defined as the difference between its arrival time at the receiver and the corresponding sending time at the sender.

packet in the probe-train in order to detect a trend existing in the time-series delay data. Based on OWD delay trend, Pathload determines whether the current rate R is faster than the available bandwidth of the path under investigation. Hence, proper detection of OWD trend in a probe-train is critical for it to produce an accurate and reliable bandwidth estimate of the path.

Note that Pathload first perform ADR (Asymptotic Dispersion Rate) probing by sending a single packet-train and checks interrupt moderation, which it detects when more than 60% of packets in a probe-train have been received back-to-back (with zero or very small inter-packet delay). If interrupt moderation is detected, Pathload first eliminates such coalesced packets from the received train. Then, it directly performs PCT (Pairwise Comparison Test) and PDT (Pairwise Difference Test) on the remaining data if the number of remaining packets is no less than 5. Recall that the PCT metric represents the fraction of consecutive OWD pairs that are increasing, while the PDT metric quantifies how strong the difference between the first and last OWDs in the data set is. Define X_j to be the one-way delay of a packet j in a set of size k. Then, the PCT and PDT metrics[4] are given by [44]:

$$PCT = \frac{1}{k-1}\sum_{j=2}^{k} I(X_j > X_{j-1}), \quad PDT = (X_k - X_1)/\sum_{j=2}^{k} |X_j - X_{j-1}|, \qquad (148)$$

where $I(Y)$ is one if Y holds, zero otherwise.

On the other hand, when Pathload does not detect interrupt moderation from the initial check, it first eliminates back-to-back packets from the probe-train just like the previous case. If the number of remaining packets is no smaller than 36, then Pathload selects OWDs from remaining packets using median-based sampling (see

[4]Pathload [44] determines OWDs as "increasing" if $PCT > 0.66$, "non-increasing" if $PCT < 0.54$, or "ambiguous" otherwise. Similarly, it identifies OWDs as "increasing" if $PDT > 0.55$, "non-increasing" if $PDT < 0.45$, or "ambiguous" otherwise.

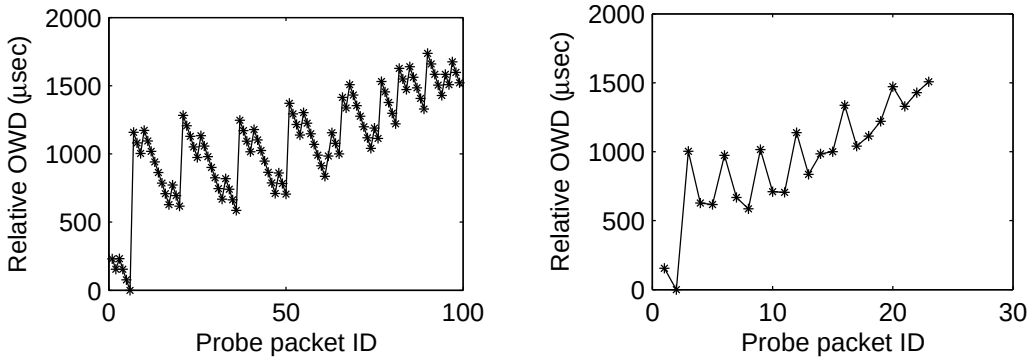

(a) OWD (original) (b) OWD (remaining)

Fig. 50. (a) Relative OWDs obtained using the path configuration in case I. (b) Remaining OWDs after removing coalesced packets.

[44] for details) and applies the PCT and PDT tests to the sampled OWDs.

To assess Pathload's trend detection mechanism, we conduct experiments for Case I with interrupt delay $\delta = 250$ μs. In this example, we collect one-way delay data by running Pathload with a fixed rate $R = 38$ Mb/s (that is substantially higher than the available bandwidth $A = 31$ Mb/s) and examine how its internal algorithm specifies a delay-trend existing in OWDs. Fig. 50(a) illustrates relative OWDs (one-way delays subtracted by their minimum value) obtained by sending packet trains at 38 Mb/s over the path in case I. Note in the figure that OWDs exhibit an increasing trend overall even though they decrease in a small-scale burst (successive OWDs in the same burst decrease if the latency for transferring a packet from NIC to the user space at the receiver is smaller than the inter-packet dispersion departing NIC at the sender [81]. Since the PCT and PDT tests cannot accurately detect a trend present in this kind of coalesced data, Pathload first removes the coalesced packets before applying the PCT and PDT tests. Fig. 50(b) shows remaining OWDs after eliminating the coalesced packets. However, even with the data shown in Fig. 50(b), Pathload is unable to detect the increasing trend present in the data since its trend-

test produces $PCT = 0.5$ and $PDT = 0.11$, which leads to *incorrect* conclusion. This indicates that Pathload's trend-detection mechanism is not robust under the presence of coalesced packets due to interrupt delays.

Note that Pathload often discards entire packet-trains even with strong presence of a trend in the data due to the number of remaining OWDs after removing coalesced packets being too small (less than 36) when interrupt moderation is not detected. This situation happens since Pathload divides a single packet-train into subgroups when one or more packets in a probe-train experience(s) unusually large delay (e.g., over 1000 μs) due to context switching or some unknown reasons in order to remove packets affected by large sending delay in trend detection. In summary, we believe that Pathload's inaccuracy in trend detection is the major problem that makes it unlikely to be successful in real networks such as the Internet.

2. IMRP: Interrupt Moderation Resilient Pathload

Motivated by the difficulty of characterizing delay variations in measured noisy OWD data, we study noise-filtering techniques such as wavelet-based signal processing and window-based averaging and explore their applicability in reliably identifying a trend from the data. In what follows below, we first investigate wavelet-based signal processing techniques that are widely used in removing noise from various data sets obtained empirically [16]. To overcome the effect of interrupt delays on trend detection, we apply a simple multi-level discrete wavelet transform [13] to OWDs before performing PCT- and PDT-based trend-test.

Note that in the multi-level wavelet decomposition, each stage consists of scale and wavelet filters followed by down-sampling by a factor of 2 and separates an input signal into two sets of coefficients: scale and wavelet coefficients. The wavelet coefficients represent a noise component in the input signal and thus are not processed

further. On the other hand, the scale coefficients are applied to the two filters in the next level as an input to further reduce noise that might still exist in the scale coefficients from the previous stage. As a decomposition level increases, the frequency of wavelets used in filters decreases, capturing lower frequency components present in the original signal.

For experiments in this section, we use the family of Daubechies wavelets [18], which are well known standard wavelets. Specifically, we use Daubechies' length-4 wavelets, whose scale filter coefficients are given by $h_0 = \frac{1+\sqrt{3}}{4\sqrt{2}}$, $h_1 = \frac{3+\sqrt{3}}{4\sqrt{2}}$, $h_2 = \frac{3-\sqrt{3}}{4\sqrt{2}}$, and $h_3 = \frac{1-\sqrt{3}}{4\sqrt{2}}$, while its wavelet filter coefficients are $g_0 = h_3$, $g_1 = -h_2$, $g_2 = h_1$, and $g_3 = -h_0$.

Assume that a sequence $s_0, s_1, \ldots, s_{n-1}$ is an input to the j-th stage filters. Define $cA_{j,k}$ and $cD_{j,k}$ (where $k = 0, 1, \ldots, n/2$) to be the scale and wavelet coefficients produced at level j, respectively. Then, $cA_{j,k}$ and $cD_{j,k}$ are given by:

$$cA_{j,k} = h_0 s_{2k} + h_1 s_{2k+1} + h_2 s_{2k+2} + h_3 s_{2k+3} \quad (149)$$

$$cD_{j,k} = g_0 s_{2k} + g_1 s_{2k+1} + g_2 s_{2k+2} + g_3 s_{2k+3}. \quad (150)$$

Note that when $k \geq n/2 - 1$, there are not enough data in the input sequence to compute the coefficients using (149) and (150). This is known as a boundary condition, which requires a special treatment that adds more data points to the input sequence [95] (if this is the case, we pad the last few OWDs as needed).

To demonstrate the effect of wavelet decomposition on trend detection, we decompose OWDs shown in Fig. 50(a) up to level 3 and plot in Fig. 51(a) the scale coefficients that represent the trend component of OWD data. Applying the same PCT and PDT tests to the scale coefficient data, we get $PCT = 0.75$ and $PDT = 0.78$, which means that OWDs exhibit an increasing trend according to the criteria used

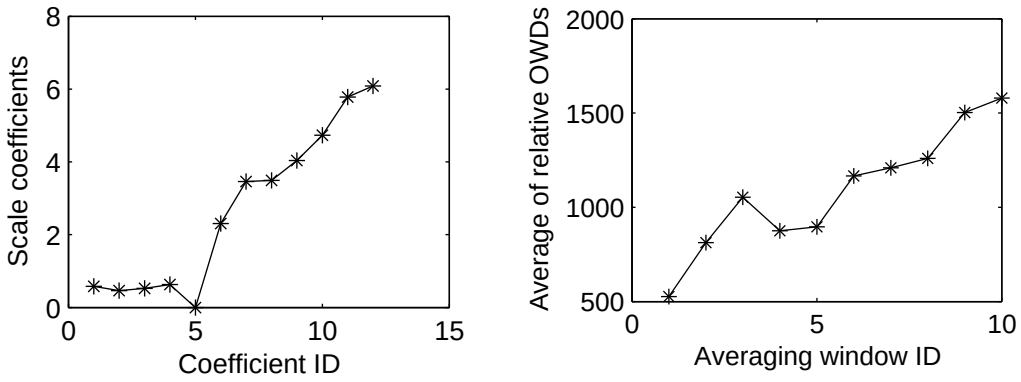

(a) Wavelet (b) Average

Fig. 51. Scale coefficients of wavelet decomposition and window-based averages of one-way delays shown in Fig. 50(a).

in Pathload (recall that Pathload fails to detect this increasing trend as discussed in Section D.1).

Next, we explore how window-based averaging improves trend detection in noisy data. In this approach, we take the average of OWDs in a window of size k (k-packet sliding window). Using a smaller window makes trend-detection susceptible to a larger interrupt delay since it may not sufficiently remove noise from OWDs (we leave optimal selection of window size as future work). For this example, we employ $k = 10$ and plot in Fig. 51(b) k-packet window averages of relative OWDs shown in Fig. 50(a), which clearly shows an increasing trend. With these averaged OWDs, we get $PCT = 0.8$ and $PDT = 0.74$, which leads us to conclude that an increasing trend exists in the measured data.

We incorporate the above trend-detection mechanisms into Pathload and call it *Interrupt Moderation Resilient Pathload* (IMRP). We then discuss its performance under a variety of end-host interrupt delays.

Table XXV. Performance of IMRP

Estimation method	Interrupt delay δ	Evaluation scenario					
		Case-I	Case-II	Case-III	Case-IV	Case-V	Case-VI
IMRP (wavelet)	0 μs	2.46%	1.23%	3.47%	2.69%	3.71%	6.52%
	100 μs	6.47%	4.5%	3.02%	4.42%	5.98%	12.17%
	125 μs	7.21%	2.64%	3.88%	1.32%	6.1%	10.77%
	500 μs	5.12%	2.17%	6.78%	3.24%	7.23%	5.56%
IMRP (average)	0 μs	2.07%	2.24%	2.1%	2.18%	9.67%	5.05%
	100 μs	0.19%	0.71%	11.69%	1.32%	4.19%	6.82%
	125 μs	1.44%	1.82%	12.58%	1.59%	2.64%	7.89%
	500 μs	4.43%	4.59%	9.27%	2.55%	8.95%	6.48%

3. Performance of IMRP

We investigate estimation accuracy of IMRP under substantially different interrupt delays δ and report its relative estimation errors e_A in Table XXV. As the table shows, IMRP produces available bandwidth estimates for all studied cases with $88 - 99\%$ accuracy under a wide range ($0 \leq \delta \leq 500$) of interrupt delays (it is reported in [45] that 500 μs interrupt delay is large enough to substantially reduce CPU overhead and achieve good throughput, which is why we show interest in it). Notice in the table that IMRP's estimation accuracy is indifferent for various values of δ, which indicates its robustness to variety of NIC configurations at the end-hosts. For example, even with a very large delay $\delta = 500$ μs, IMRP measures the paths within $e_A = 10\%$ error in all studied cases. This is substantial improvement over that of Pathload, which can only measure paths with small interrupt delays (i.e., $\delta < 125$ μs) as discussed in Section D.1.

Note that IMRP is as fast as Pathload and its measurement duration in producing estimates is virtually same as that of Pathload since numerical computation time for wavelet decomposition of small number ($N = 100$) of delay samples or for their

Table XXVI. Available Bandwidth Estimation Methods ($\delta = 500$ μs)

Estimation method	Metrics	Evaluation scenario					
		Case-I	Case-II	Case-III	Case-IV	Case-V	Case-VI
PRC-MT	e_A	3.71%	3.83%	1.55%	0.19%	5.81%	5.56%
	time	90 sec	89 sec	133 sec	89 sec	92 sec	96 sec
IMRP	e_A	5.12%	2.17%	6.78%	3.24%	7.23%	5.56%
	time	88 sec	89 sec	95 sec	99 sec	79 sec	80 sec
Pathload	e_A	−−	−−	−−	−−	−−	−−
	time	−−	−−	−−	−−	−−	−−
Pathchirp	e_A	10.84%	8.53%	0.39%	1.62%	19.81%	18.04%
	time	200 sec	200 sec	200 sec	200 sec	200 sec	200 sec
IGI	e_A	10.58%	4.21%	72.76%	19.72%	13.38%	98.56%
PTR		16.02%	9.93%	30.28%	24.63%	5.31%	59.24%
	time	3 sec	4 sec	5 sec	6 sec	3 sec	5 sec

average is negligible compared to the time needed to collect the probes.

4. Performance Comparison under Interrupt Moderation

We compare PRC-MT with IMRP as well as the same existing available bandwidth estimators and capacity estimation tools studied in Section C with a large interrupt delay $\delta = 500$ μs to understand their robustness to end-host interrupt moderation. For this purpose, we use the same path configurations discussed in Section C.

a. Available Bandwidth Estimation

Table XXVI illustrates relative estimation errors e_A of all available bandwidth estimators studied in this chapter for different cases under an interrupt delay $\delta = 500$ μs. For IMRP, we evaluate both wavelet- and averaging-based algorithms, but report only wavelet-based estimates since the other produces similar results. Notice in the table that PRC-MT produces very accurate bandwidth estimates (less than 10% of

Table XXVII. Capacity Estimation Methods ($\delta = 500$ μs)

Methods	Relative estimation error e_C			
	Case-II		Case-IV	
	e_C	time	e_C	time
PRC-MT	1.72%	89 (sec)	7.65%	86 (sec)
Pathrate	17.5%	2191 (sec)	18.33%	2191 (sec)
CapProbe	57.65%	500 (sec)	81.77%	500 (sec)

error) and outperforms all other existing methods studied. Even with IMRP that uses our improved trend detection mechanisms, estimation accuracy is not as good as PRC-MT. Observe that Pathchirp exhibits estimation accuracy that is slightly worse than PRC-MT and IMRP in some cases (e.g., cases II, V, and VI), but comparable to them in other cases. Note that Pathchirp's estimation accuracy is similar to that observed without using interrupt moderation ($\delta = 0$) (see Table XXII), which implies that its "jumbo" option (if selected properly) that sends substantially more packets makes it resilient to interrupt delays. Estimation accuracy of IGI/PTR is not much different from those cases with no interrupt delay shown in Table XXII, but is a lot worse than that of PRC-MT and IMRP as well as Pathchirp.

b. Capacity Estimation

We compare PRC-MT with CapProbe and Pathrate in cases II and IV, in which tight link and narrow link coincide. We show relative estimation errors e_C of the above methods in Table XXVII. As the table shows, PRC-MT produces capacity estimates with over 90% accuracy, which significantly outperforms Pathrate and CapProbe in the studied cases.

Table XXVIII. Bandwidth Sampling Overhead ($\delta = 100$ μs)

Methods	Case-II			Case-IV		
	Samples	$\bar{q}$ (bytes)	Data (MB)	Samples	$\bar{q}$ (bytes)	Data (MB)
PRC-MT	32,162	262	8.4	14,086	292	4.1
IMRP	8,400	239	2	12,000	225	2.7
Pathload	10,800	260	2.8	12,000	267	3.2
Pathchirp	7,560	1,000	7.5	7,560	1,000	7.5
IGI/PTR	600	1,000	0.6	800	1,000	0.8
Pathrate	26,000	1,454	37.8	26,000	1,454	37.8
CapProbe	1,800	1,000	1.8	1,800	1,000	1.8

5. Measurement Overhead

We next discuss the amount of probe data used in bandwidth sampling for different methods. For this experiment, we use a small interrupt delay $\delta = 100$ μs to allow Pathload's algorithm to terminate normally and produce bandwidth estimates of all the path shown in Table XX. For the existing methods, we use the same packet size and number of trains or packet pairs recommended in the original paper.

Table XXVIII shows the number of packet samples and corresponding data used to get bandwidth estimates for cases II and IV. When tools use varying packet size during probing, we show their average ($\bar{q}$ in the table). As the table shows, IGI/PTR and CapProbe do not use many samples while PRC-MT, IMRP, Pathload, Pachchirp, and Pathrate require significantly more probe packets for their measurement. Note that PRC-MT requires even more samples in case I than Pathrate to examine the path. However, since it uses smaller packet size on average, the amount of data used is significantly less than that of Pathrate. For instance, Pathrate sends 26000 samples in both cases, which amounts to 37 MB of data, while PRC-MT uses $4 - 8$ MB of probe packets. Also note that both IMRP and Pathload incur almost 4 times less

overhead than Pathchirp.

Recall that in all experiments studied in this chapter, we use "jumbo" option to increase Pathchirp's estimation accuracy since without using that option, its accuracy is significantly worse than Pathload. This result is somewhat different from that reported in [92], which conducted simulations using `ns2` with low link utilization (at most 53%). In our experimental setup used in this work where link utilization reaches up to 80%, Pathchirp cannot produce accurate estimates due to timestamping inaccuracy and interrupt moderation. Higher measurement overhead of Pathchirp in this work (different from that in [92]) accounts for the use of the jumbo option.

E. Internet Experiments

In this section, we report experimental results obtained by measuring two Internet paths between universities in U.S. The first path is from the University of Utah (Utah) to Texas A&M University (TAMU) and the other is from Utah to the University of Texas at Austin (UTexas). Note that we choose these paths simply for the convenience of accessibility. Also note that the purpose of this experiment is not to compare estimation accuracy of bandwidth estimators since we do not know exact characteristics of these paths. Instead, we use this example as a sort of sanity test for how these tools work in the Internet.

Table XXIX shows bandwidth estimates of all 8 tools investigated in this chapter. In the first path, Three tools (PRC-MT, IMRP, and Pathload) produce similar bandwidth estimates that are in a range of $86-93$ Mb/s, while the others (Pathchirp and IGI/PTR) estimate the same path as 68 Mb/s and 69 Mb/s, respectively. For the second path (Utah-UTexas), all methods produce available bandwidth estimates $\tilde{A}_t$ that are in a range $[79-101]$ Mb/s. Recall that unlike other estimators, PRC-MT

Table XXIX. Internet Experiments

Method	Utah → TAMU	Utah → UTexas
PRC-MT	$\tilde{A}_t = 86$ Mb/s	$\tilde{A}_t = 98$ Mb/s
	$\tilde{C}_t = 94$ Mb/s	$\tilde{C}_t = 97$ Mb/s
IMRP	$\tilde{A}_t = 91$ Mb/s	$\tilde{A}_t = 101$ Mb/s
Pathload	$\tilde{A}_t = 93$ Mb/s	$\tilde{A}_t = 96$ Mb/s
Pathchirp	$\tilde{A}_t = 68$ Mb/s	$\tilde{A}_t = 79$ Mb/s
IGI/PTR	$\tilde{A}_t = 69/69$ Mb/s	$\tilde{A}_t = 101/88$ Mb/s
Pathrate	$\tilde{C}_n = 96$ Mb/s	$\tilde{C}_t = 94$ Mb/s
CapProbe	$\tilde{C}_t = 13$ Mb/s	$\tilde{C}_t = 10$ Mb/s

can also measure the tight-link capacity C_t. PRC-MT produces $\tilde{C}_t = 94$ Mb/s for the Utah-TAMU path and $\tilde{C}_t = 97$ Mb/s for the Utah-UTexas paths. We also run two bottleneck (narrow link) capacity estimators, Pathrate and CapProbe, and show estimation results in the table as well. Notice in the table that Pathrate measures the narrow link capacity of the two paths as 96 Mb/s in Utah-TAMU path and 94 Mb/s in the Utah-UTexas path, while CapProbe produces significantly lower estimates of 10 Mb/s and 13 Mb/s for the same two paths. Observe that Capprobe's capacity estimates for both paths are even less than available bandwidth estimates produced by other tools by a factor of $7 - 8$, which strongly implies that estimates produced by Capprobe are substantially different from their true values.

CHAPTER VII

CONCLUSION AND FUTURE WORK

In this chapter, we summarize the major results of this thesis and discuss some future directions for extension of this work.

A. Conclusion

In Chapter III, we studied characteristics of video streaming in best-effort networks and proposed a preferential streaming framework called Partitioned Enhancement Layer Streaming (PELS) that can provide a high level of end-user QoS. We further studied modified Kelly controls in conjunction with PELS and found that they presented a good foundation for future video streaming in AQM environments. Since the PELS framework is independent of congestion control methods employed, it can be further used with a variety of existing and future game-theoretic or optimization-based controllers.

In Chapter IV, we investigated the effect of random packet loss on scalable video traffic in best-effort networks and proposed an adaptive FEC overhead control mechanism that can provide high quality of video to end-users. We also investigated the characteristics of packet loss in an FEC block and derived practical models for the distribution of the number of lost packets in a block of fixed size under Markov packet loss. Furthermore, we examined several stochastic loss models for streaming video and conclusively established that proper control of FEC overhead can significantly improve the utility of received video over lossy channels.

In Chapter V, we examined the problem of estimating the capacity and available

bandwidth of a single congested link and showed a simple stochastic analysis of the problem. Unlike previous approaches, our estimation did not rely on empirically-driven methods, but instead used a queuing model of the bottleneck router that specifically assumed non-negligible, non-fluid cross-traffic. It is also the first model to provide simultaneous asymptotically-accurate estimation of both C and A in the presence of arbitrary cross-traffic.

After successfully characterizing a single-congested path, we focused on measuring the tight-link of a multi-hop path and developed an automated measurement tool (called Envelope) that is based on a recursive extension of the single-hop estimator. Through simulations, we showed that Envelope is asymptotically accurate (to the extent possible to observe using finite-sampling) in estimating both types of bandwidth. We also presented extensive simulation results of existing methods Pathload, Spruce, IGI, Pathrate, and CapProbe and their comparison to Envelope. These results suggested that in multi-link paths with significant cross-traffic interference at non-tight links, most existing methods cannot converge to the correct values of the bottleneck capacity C or available bandwidth A, even if the sampling process is sufficiently long. We further demonstrated that in many network settings, Envelope can also estimate bandwidth for some non-tight links in the path.

In Chapter VI, we implemented a new bandwidth measurement tool called PRC-MT that can extract both bandwidth metrics of the tight link over multi-hop paths under arbitrary cross-traffic and routing patterns. We evaluated PRC-MT in Emulab and PlanetLab and showed that PRC-MT produces available bandwidth and capacity estimates with very high accuracy. We also evaluated existing bandwidth estimation tools under various network settings and found that certain proposed algorithms (such as Pathload) becomes susceptible to timing irregularities caused by network hardware interrupt moderation. We identified its estimation instability under non-

negligible interrupt delays and found that Pathload's instability stems from that its delay-trend detection mechanism is unreliable when probing packets are coalesced at the receiver. We overcame this problem using robust trend detection algorithms (called IMRP) based on signal de-noising and showed that IMRP greatly improves measurement stability of Pathload under various network settings.

B. Future Work

It is likely that multimedia content will be pervasive in the future Internet and the demand for high-quality streaming services will remain very high. In order to solve the problems related to large-scale delivery of multimedia content over the Internet, we would like to expand this work to cover overlay networks (such as content distribution networks and peer-to-peer systems) that are increasingly used as a vehicle to deploy new services over the current Internet without support from the underlying infrastructure. This involves addressing issues associated with efficient overlay self-reconfiguration and maintenance, load balancing among servers in the network, and optimal selection of servers or paths for streaming services. We also have interest in studying performance issues of real-time streaming in wireless environments as increasing number of users rely on various wireless networks to gain access to the Internet.

In addition, we have further interest in bandwidth characterization techniques, which can directly benefit real-time streaming services over the Internet. As the speed of network connections increases, measuring bandwidth of Internet paths can become very susceptible to operating system (OS) and hardware-related timing irregularities because they introduce artificial delays that are unrelated to network events such as queuing. Even though our work succeeded at designing accurate bandwidth

measurement techniques under the influence of timing irregularities related to network hardware interrupt moderation at the receiving host, its performance in the presence of severe OS scheduling delay jitter that depends on the CPU utilization of the sending and/or receiving hosts requires future work. We also have interest in further reducing measurement duration and overhead without sacrificing estimation accuracy.

REFERENCES

[1] B. Ahlgren, M. Björkman, and B. Melander, "Network Probing Using Packet Trains," Swedish Institute, Tech. Rep., Mar. 1999.

[2] M. Allman and V. Paxson, "On Estimating End-to-End Network Path Properties," in *Proc. ACM SIGCOMM*, Aug. 1999, pp. 263–274.

[3] E. Altman, C. Barakat, and V. M. Ramos, "Queueing Analysis of Simple FEC Schemes for IP Telephony," in *Proc. IEEE INFOCOM*, Apr. 2001, pp. 796–804.

[4] F. Baccelli, S. Machiraju, D. Veitch, and J. Bolot, "The Role of PASTA in Network Measurement," in *Proc. ACM SIGCOMM*, Sep. 2006, pp. 231–242.

[5] S. Bajaj, L. Brelau, and S. Shenker, "Uniform versus Priority Dropping for Layered Video," in *Proc. ACM SIGCOMM*, Sep. 1998, pp. 131–143.

[6] D. Bansal and H. Balakrishnan, "Binomial Congestion Control Algorithms," in *Proc. IEEE INFOCOM*, Apr. 2001, pp. 631–640.

[7] E. Biersack, "Performance Evaluation of Forward Error Correction in ATM Networks," in *Proc. ACM SIGCOMM*, Oct. 1992, pp. 248–257.

[8] P. Billingsley, *Probability and Measure*, 3rd ed. John Wiley & Sons, Inc., 1995.

[9] S. Blake, D. Black, M. Carlson, E. Davies, Z. Wang, and W. Weiss, "An Architecture for Differentiated Services," *IETF RFC 2475*, Dec. 1998.

[10] J. Bolot, "End-to-End Packet Delay and Loss Behavior in the Internet," in *Proc. ACM SIGCOMM*, Sep. 1993, pp. 289–298.

[11] J. Bolot, S. Fosse-Parisis, and D. Towsley, "Adaptive FEC-Based Error Control for Internet Telephony," in *Proc. IEEE INFOCOM*, Mar. 1999, pp. 1453–1460.

[12] R. Braden, D. Clark, and S. Shenker, "Integrated Services in the Internet Architecture: An Overview," *IETF RFC 1633*, Jun. 1994.

[13] C. Burrus, R. Gopinath, and H. Guo, *Introduction to Wavelets and Wavelet Transforms: A Primer*. Prentice-Hall, 1998.

[14] R. L. Carter and M. E. Crovella, "Measuring Bottleneck Link Speed in Packet Switched Networks," *Performance Evaluation*, vol. 27–28, pp. 297–318, Oct. 1996.

[15] D. Clark and W. Fang, "Explicit Allocation of Best Effort Packet Delivery Service," *IEEE/ACM Trans. Netw.*, vol. 6, no. 4, pp. 362–373, Aug. 1998.

[16] P. Craigmile, P. Guttorp, and D. Percival, "Trend Assessment in a Long Memory Dependence Model Using the Discrete Wavelet Transform," *Environmetrics*, vol. 15, no. 4, pp. 313–335, May 2004.

[17] M. Dai and D. Loguinov, "Analysis of Rate-Distortion Functions and Congestion Control in Scalable Internet Video Streaming," in *Proc. ACM NOSSDAV*, Jun. 2003, pp. 60–69.

[18] I. Daubechies, "Orthonormal Bases of Compactly Supported Wavelets," *Communications on Pure and Applied Mathematics*, vol. 41, no. 7, pp. 909–996, Oct. 1988.

[19] A. Demers, S. Keshav, and S. Shenker, "Analysis and Simulation of a Fair Queuing Algorithm," in *Proc. ACM SIGCOMM*, Sep. 1989, pp. 1–12.

[20] A. Dhamdhere, H. Jiang, and C. Dovrolis, "Buffer Sizing for Congested Internet Links," in *Proc. IEEE INFOCOM*, Mar. 2005, pp. 1072–1083.

[21] C. Dovrolis, P. Ramanathan, and D. Moore, "Packet-Dispersion Techniques and a Capacity-Estimation Methodology," *IEEE/ACM Trans. Netw.*, vol. 12, no. 6, pp. 963–977, Dec. 2004.

[22] C. Dovrolis, P. Ramanathan, and D. Moore, "What Do Packet Dispersion Techniques Measure?" in *Proc. IEEE INFOCOM*, Apr. 2001, pp. 905–914.

[23] A. B. Downey, "Using PATHCHAR to Estimate Internet Link Characteristics," in *Proc. ACM SIGCOMM*, Aug. 1999, pp. 241–250.

[24] Emulab. [Online]. Available: http://www.emulab.net/. Accessed: Apr. 2008.

[25] V. Firoiu and M. Borden, "A Study of Active Queue Management for Congestion Control," in *Proc. IEEE INFOCOM*, Mar. 2000, pp. 1435–1444.

[26] V. Firoiu, X. Zhang, and Y. Guo, "Best Effort Differentiated Services: Trade-off Service Differentiation for Elastic Applications," in *Proc. IEEE ICT*, Jun. 2001.

[27] S. Floyd, "TCP and Explicit Congestion Notification," *ACM Comput. Commun. Rev.*, vol. 24, no. 5, pp. 10–23, Oct. 1994.

[28] S. Floyd, M. Handley, J. Padhye, and J. Widmer, "Equation-Based Congestion Control for Unicast Applications," in *Proc. ACM SIGCOMM*, Aug. 2000, pp. 43–56.

[29] S. Floyd and V. Jacobson, "Random Early Detection Gateways for Congestion Avoidance," *IEEE/ACM Trans. Netw.*, vol. 1, no. 4, pp. 397–413, Aug. 1993.

[30] C. Fraleigh, S. Moon, B. Lyles, C. Cotton, M. Khan, D. Moll, R. Rockell, T. Seely, and C. Diot, "Packet-Level Traffic Measurements from the Sprint IP Backbone," *IEEE Network*, vol. 17, no. 6, pp. 6–16, Nov./Dec. 2003.

[31] P. Frossard and O. Verscheure, "Joint Source/FEC Rate Selection for Qualtiy-Optimal MPEG-2 Video Delivery," *IEEE Trans. Image Processing*, vol. 10, no. 12, pp. 1815–1825, Dec. 2001.

[32] E. N. Gilbert, "Capacity of a Burst-Noise Channel," *Bell Systems Technical Journal*, vol. 39, pp. 1253–1265, Sep. 1960.

[33] E. Gurses, G. B. Akar, and N. Akar, "Impact of Scalability in Video Transmission in Promotion-Capable Differentiated Service Networks," in *Proc. IEEE ICIP*, Sep. 2002, pp. 753–756.

[34] P. Haga, K. Diriczi, G. Vattay, and I. Csabai, "Granular Model of Packet Pair Separation in Poissonian Traffic," *Computer Networks*, vol. 51, no. 3, pp. 683–698, Feb. 2007.

[35] K. Harfoush, A. Bestavros, and J. Byers, "Measuring Bottleneck Bandwidth of Targeted Path Segments," in *Proc. IEEE INFOCOM*, Apr. 2003, pp. 2079–2089.

[36] N. Hu, L. Li, Z. Mao, and P. Steenkiste, "Locating Internet Bottlenecks: Algorithms, Measurements, and Implications," in *Proc. ACM SIGCOMM*, Aug. 2004, pp. 41–54.

[37] N. Hu and P. Steenkiste, "Evaluation and Characterization of Available Bandwidth Probing Techniques," *IEEE J. Sel. Areas Commun.*, vol. 21, no. 6, pp. 879–974, Aug. 2003.

[38] P. Hurley, M. Kara, J. Y. L. Boudec, and P. Thiran, "ABE: Providing a Low-Delay Service within Best Effort," *IEEE Network Magazine*, vol. 15, no. 3, pp. 60–69, May 2001.

[39] Interrupt Moderation Using Intel GbE Controllers. [Online]. Available: http://download.intel.com/design/network/applnots/ap450.pdf. Accessed: Apr. 2008.

[40] Iperf – The TCP/UDP Bandwidth Measurement Tool. [Online]. Available: http://dast.nlanr.net/Projects/Iperf/. Accessed: Apr. 2008.

[41] V. Jacobson, "Pathchar – A Tool to Infer Characteristics of Internet Paths." [Online]. Available: ftp://ftp.ee.lbl.gov/pathchar/. Accessed: Apr. 2008.

[42] V. Jacobson, "Congestion Avoidance and Control," in *Proc. ACM SIGCOMM*, Aug. 1988, pp. 314–329.

[43] M. Jain and C. Dovrolis, "End-to-End Available Bandwidth: Measurement Methodology, Dynamics, and Relation with TCP Throughput," in *Proc. ACM SIGCOMM*, Aug. 2002, pp. 295–308.

[44] M. Jain and C. Dovrolis, "Pathload: A Measurement Tool for End-to-End Available Bandwidth," in *Proc. Passive and Active Measurement Workshop*, Mar. 2002.

[45] G. Jin and B. L. Tierney, "System Capability Effects on Algorithms for Network Bandwidth Measurement," in *Proc. ACM IMC*, Oct. 2003, pp. 27–38.

[46] R. Johari and D. K. H. Tan, "End-to-End Congestion Control for the Internet: Delays and Stability," *IEEE/ACM Trans. Netw.*, vol. 9, no. 6, pp. 818–832, Dec. 2001.

[47] S. Kang, X. Liu, A. Bhati, and D. Loguinov, "On Estimating Tight-Link Bandwidth Characteristics over Multi-Hop Paths," in *Proc. IEEE ICDCS*, Jul. 2006.

[48] S. Kang, X. Liu, M. Dai, and D. Loguinov, "Packet-Pair Bandwidth Estimation: Stochastic Analysis of a Single Congested Node," in *Proc. IEEE ICNP*, Oct. 2004, pp. 316–325.

[49] R. Kapoor, L. Chen, L. Lao, M. Gerla, and M. Sanadidi, "CapProbe: A Simple and Accurate Capacity Estimation Technique," in *Proc. ACM SIGCOMM*, Aug. 2004, pp. 67–78.

[50] D. Katabi, M. Handley, and C. Rohrs, "Congestion Control for High Bandwidth Delay Product Networks," in *Proc. ACM SIGCOMM*, Aug. 2002, pp. 89–102.

[51] F. P. Kelly, A. K. Maulloo, and D. K. H. Tan, "Rate Control for Communication Networks: Shadow Prices, Proportional Fairness and Stability," *J. of Oper. Res. Soc.*, vol. 49, no. 3, pp. 237–252, Mar. 1998.

[52] S. Keshav, "A Control-Theoretical Approach to Flow Control," in *Proc. ACM SIGCOMM*, Sep. 1991, pp. 3–15.

[53] S. Kunniyur and R. Srikant, "Analysis and Design of an Adaptive Virtual Queue (AVQ) Algorithm for Active Queue Management," in *Proc. ACM SIGCOMM*, Aug. 2001, pp. 123–134.

[54] K. Lai and M. Baker, "Measuring Bandwidth," in *Proc. IEEE INFOCOM*, Mar. 1999, pp. 235–245.

[55] K. Lai and M. Baker, "Measuring Link Bandwidths Using a Deterministic Model of Packet Delay," in *Proc. ACM SIGCOMM*, Aug. 2000, pp. 283–294.

[56] L. Lao, C. Dovrolis, and M. Y. Sanadidi, "The Probe Gap Model can Underestimate the Available Bandwidth of Multihop Paths," *ACM SIGCOMM Comput. Commun. Review*, vol. 36, no. 5, pp. 29–34, Oct. 2006.

[57] D. Lapsley and S. Low, "Random Early Marking: An Optimization Approach to Internet Congestion Control," in *Proc. IEEE ICON*, Oct. 1999, pp. 67–74.

[58] D. Li and D. R. Cheriton, "Evaluating the Utility of FEC with Reliable Multicast," in *Proc. IEEE ICNP*, Oct. 1999, pp. 97–105.

[59] J.-R. Li, S. Ha, and V. Bharghavan, "HPF: A Transport Protocol for Supporting Heterogeneous Packet Flows in the Internet," in *Proc. IEEE INFOCOM*, Mar. 1999, pp. 543–550.

[60] X. Liu, K. Ravindran, B. Liu, and D. Loguinov, "Single-Hop Probing Asymptotics in Available Bandwidth Estimation: Sample-Path Analysis," in *Proc. ACM IMC*, Oct. 2004, pp. 300–313.

[61] X. Liu, K. Ravindran, and D. Loguinov, "Multi-Hop Probing Asymptotics in Available Bandwidth Estimation: Stochastic Analysis," in *Proc. ACM IMC*, Oct. 2005, pp. 173–186.

[62] X. Liu, K. Ravindran, and D. Loguinov, "What Signals Do Packet-Pair Dispersions Carry?" in *Proc. IEEE INFOCOM*, Mar. 2005.

[63] X. Liu, K. Ravindran, and D. Loguinov, "Measuring Probing Response Curves over the RON Testbed," in *Proc. Passive and Active Measurement Workshop*, Mar. 2006.

[64] D. Loguinov and H. Radha, "End-to-End Internet Video Traffic Dynamics: Statistical Study and Analysis," in *Proc. IEEE INFOCOM*, Jun. 2002, pp.

723–732.

[65] S. Low, "Equilibrium Bandwidth and Buffer Allocations for Elastic Traffics," *IEEE/ACM Trans. Netw.*, vol. 8, no. 3, pp. 373–383, Jun. 2000.

[66] S. Low, L. Peterson, and L. Wang, "Understanding TCP Vegas: A Duality Model," in *Proc. ACM SIGMETRICS*, Jun. 2001, pp. 226–235.

[67] S. H. Low and D. E. Lapsley, "Optimization Flow Control I: Basic Algorithm and Convergence," *IEEE/ACM Trans. Netw.*, vol. 7, no. 6, pp. 861–874, Dec. 1999.

[68] S. H. Low, F. Paganini, J. Wang, S. Adlakha, and J. Doyle, "Dynamics of TCP/RED and a Scalable Control," in *Proc. IEEE INFOCOM*, Jun. 2002, pp. 239–248.

[69] S. Machiraju, D. Veitch, F. Baccelli, and J. Bolot, "Adding Definition to Active Probing," *ACM SIGCOMM Comp. Comm. Rev.*, vol. 37, no. 2, pp. 17–28, Apr. 2007.

[70] B. Mah, "Pchar: A Tool for Measuring Internet Path Characteristics." [Online]. Available: http://www.kitchenlab.org/www/bmah/Software/pchar/. Accessed: Apr. 2008.

[71] L. Massoulié, "Stability of Distributed Congestion Control with Heterogeneous Feedback Delays," *IEEE Trans. Automat. Contr.*, vol. 47, no. 6, pp. 895–902, Jun. 2002.

[72] B. Melander, M. Björkman, and P. Gunningberg, "A New End-to-End Probing and Analysis Method for Estimating Bandwidth Bottlenecks," in *Proc. IEEE GLOBECOM*, Nov. 2000, pp. 415–420.

[73] Network Simulator. [Online]. Available: http://www.isi.edu/nsnam/ns/. Accessed: Apr. 2008.

[74] A. Papoulis, *Probability, Random Variables, and Stochastic Processes*, 2nd ed. McGraw-Hill, 1984.

[75] K.-J. Park, H. Lim, and C.-H. Choi, "Stochastic Analysis of Packet-Pair Probing for Network Bandwidth Estimation," *Computer Networks*, vol. 50, no. 12, pp. 1901–1915, Aug. 2006.

[76] A. Pásztor and D. Veitch, "Active Probing Using Packet Quartets," in *Proc. ACM IMW*, Nov. 2002, pp. 293–305.

[77] A. Pásztor and D. Veitch, "The Packet Size Dependence of Packet Pair Like Methods," in *Proc. IEEE/IFIP IWQoS*, May 2002, pp. 204–213.

[78] V. Paxson, "Measurements and Analysis of End-to-End Internet Dynamics," *Ph.D. Dissertation, Computer Science Department, University of California at Berkeley*, 1997.

[79] C. Perkins, O. Hodson, and V. Hardman, "A Survey of Packet Loss Recovery Techniques for Streaming Audio," *IEEE Network*, vol. 12, pp. 40–48, Sep. 1998.

[80] PlanetLab. [Online]. Available: http://planet-lab.org/. Accessed: Apr. 2008.

[81] R. Prasad, M. Jain, and C. Dovrolis, "Effects of Interrupt Coalescence on Network Measurements," in *Proc. Passive and Active Measurement Workshop*, Apr. 2004.

[82] QBone Scavenger Service. [Online]. Available: http://qbone.internet2.edu/qbss. Accessed: Apr. 2008.

[83] H. Radha, M. Schaar, and Y. Chen, "The MPEG-4 Fine-Grained Scalable Video Coding Method for Multimedia Streaming Over IP," *IEEE Trans. Multimedia*, vol. 3, no. 1, pp. 53–68, Mar. 2001.

[84] S. Ratnasamy and S. McCanne, "Inference of Multicast Routing Trees and Bottleneck Bandwidths Using End-to-End Measurements," in *Proc. IEEE INFOCOM*, Mar. 1999, pp. 353–360.

[85] V. Ribeiro, R. Riedi, R. Baraniuk, J. Navratil, and L. Cottrell, "pathChirp: Efficient Available Bandwidth Estimation for Network Paths," in *Proc. Passive and Active Measurement Workshop*, Apr. 2003.

[86] P. I. Richards, *Manual of Mathematical Physics*. Pergamon, 1959.

[87] O. Rose, "Statistical Properties of MPEG Video Traffic and Their Impact on Traffic Modeling in ATM Systems," in *Proc. 20th Annual Conference on Local Computer Networks*, Oct. 1995.

[88] S. Shenker and L. Breslau, "Two Issues in Reservation Establishment," in *Proc. ACM SIGCOMM*, Aug. 1995, pp. 14–26.

[89] J. Shin, J. G. Kim, J. W. Kim, and C. C. Kuo, "Dynamic QoS Mapping Control for Streaming Video in Relative Service Differentiated Networks," *European Trans. on Telecommunications*, vol. 12, no. 3, pp. 217–229, May 2001.

[90] J. Shin, J. W. Kim, and C. C. Kuo, "Quality-of-Service Mapping Mechanism for Packet Video in Differentiated Services Network," *IEEE Trans. Multimedia*, vol. 3, no. 2, pp. 219–231, Jun. 2001.

[91] M. Shreedhar and G. Varghese, "Efficient Fair Queuing Using Deficit Round-Robin," *IEEE/ACM Trans. Netw.*, vol. 4, no. 3, pp. 375–385, Jun. 1996.

[92] A. Shriram and J. Kaur, "Empirical Evaluation of Techniques for Measuring Available Bandwidth," in *Proc. IEEE INFOCOM*, May 2007.

[93] D. Sisalem and H. Schulzrinne, "The Loss-Delay Based Adjustment Algorithm: A TCP-friendly Adaptation Scheme," in *Proc. ACM NOSSDAV*, Jul. 1998.

[94] C. Stein, "A Bound for the Error in the Normal Approximation to the Distribution of a Sum of Dependent Random Variables," *6th Berkeley Symp. Math. Statist. Probab.*, vol. 2, pp. 583–602, 1972.

[95] G. Strang and T. Nguyen, *Wavelets and Filter Banks*. Wellesley-Cambridge Press, 1996.

[96] J. Strauss, D. Katabi, and F. Kaashoek, "A Measurement Study of Available Bandwidth Estimation Tools," in *Proc. ACM IMC*, Oct. 2003, pp. 39–44.

[97] Suyono and J. Weide, "A Method for Computing Total Downtime Distributions in Repairable Systems," *Journal of Applied Probability*, vol. 40, no. 3, pp. 643–653, 2003.

[98] J. Tang, G. Morabito, I. Akyildiz, and M. Johnson, "RCS: A Rate Control Scheme for Real-time Traffic in Networks with High Bandwidh Delay Products and High Bit Error Rates," in *Proc. IEEE INFOCOM*, Apr. 2001, pp. 114–122.

[99] K. Thompson, G. Miller, and R. Wilder, "Wide-Area Internet Traffic Patterns and Characteristics," *IEEE Network*, vol. 11, no. 6, pp. 10–23, Nov./Dec. 1997.

[100] M. van der Schaar and H. Radha, "Network and Device Driven Motion-Compensated Scalable Video for Wireless Systems," in *Proc. Packet Video*, Apr. 2002.

[101] R. Wade, M. Kara, and P. Dew, "Study of a Transport Protocol Employing Bottleneck Probing and Token Bucket Flow Control," *5th IEEE Symposium on Computers and Communications*, 2000.

[102] R. W. Wolff, *Stochastic Modeling and the Theory of Queues.* Prentice Hall, 1989.

[103] H. Wu, M. Claypool, and R. Kinicki, "A Model for MPEG with Forward Error Correction and TCP-Friendly Bandwidth," in *Proc. ACM NOSSDAV*, Jun. 2003, pp. 122–130.

[104] M. Yajnik, S. Moon, J. Kurose, and D. Towsley, "Measurement and Modelling of the Temporal Dependence in Packet Loss," in *Proc. IEEE INFOCOM*, Mar. 1999, pp. 345–352.

[105] H. Yousefizadeh and H. Jafarkhani, "Statistical Guarantee of QoS in Communication Networks with Temporally Correlated Loss," in *Proc. IEEE GLOBECOM*, Dec. 2003, pp. 4039–4043.

[106] L. Zhang, S. Deering, D. Estrin, S. Shenker, and D. Zappala, "RSVP: A New Resource Reservation Protocol," *IEEE Network*, vol. 7, no. 5, pp. 8–18, Sep. 1993.

[107] Y. Zhang, S.-R. Kang, and D. Loguinov, "Delayed Stability and Performance of Distributed Congestion Control," in *Proc. ACM SIGCOMM*, Aug. 2004, pp. 307–318.

[108] L. Zhao, J. W. Kim, and C. C. Kuo, "MPEG-4 FGS Video Streaming with Constant-Quality Rate Control and Differentiated Forwarding," in *Proc. SPIE VCIP*, Jan. 2002, pp. 230–241.

VITA

Seong-Ryong Kang received his B.S. degree in Electrical Engineering from Kyungpook National University, Korea, in 1993 and M.S. degree in Electrical Engineering from Texas A&M University, College Station, TX, in 2000. He graduated with the Ph.D. in Computer Science at Texas A&M University May 2008.

During 1993-1998, he worked as a patent engineer/consultant for First Intellectual Property Services of Korea. His research interests include Internet video streaming, network QoS and rate control, bandwidth estimation, and performance modeling and analysis. He may be contacted at:

Seong-Ryong Kang

2500 Central Park Lane #502

College Station, Texas 77840

U.S.A.